Nanocarbon-containing High Power Cathode for Rechargeable Hybrid Aqueous Battery

by

Xiao Zhu

A thesis
presented to the University of Waterloo
in fulfillment of the
thesis requirement for the degree of
Doctor of Philosophy
in
Chemical Engineering (Nanotechnology)

Waterloo, Ontario, Canada, 2017

Examining Committee Membership

The following served on the Examining Committee for this thesis. The decision of the Examining Committee is by majority vote.

External Examiner	NAME: Xueliang Sun Title: Professor
Supervisor(s)	NAME: Pu Chen Title: Professor
Internal Member	NAME: Eric Croiset Title: Professor
Internal Member	NAME: Leonardo Simon Title: Professor
Internal-external Member	NAME: Xianguo Li (MME) Title: Professor

AUTHOR'S DECLARATION

I hereby declare that I am the sole author of this thesis. This is a true copy of the thesis, including any required final revisions, as accepted by my examiners.

I understand that my thesis may be made electronically available to the public.

Abstract

Aqueous batteries have been considered to be one of the most suitable large-scale energy storage systems that require excellent safety, low cost and high power. A new secondary aqueous $Zn/LiMn_2O_4$ battery system, called Rechargeable Hybrid Aqueous Battery (ReHAB), has been developed by our group recently. Compared to lead-acid batteries that have been widely used as large-scale energy storage systems, this system is more environmentally friendly and shows higher Coulombic efficiency as well as longer cycle life. However, the rate capability of the $LiMn_2O_4$ cathode is intrinsically low, which leads to the low capacity at a high current density operation.

One strategy to increase the rate capability of the $LiMn_2O_4$ cathode is adding conductive additives (*e.g.*, acetylene black (AB), carbon nanotubes (CNTs) and graphene) to the $LiMn_2O_4$ cathode to improve its electrical conductivity. However, traditional conductive additives, like AB, give limited conductivity improvement and can provide neither long-range conductivity nor multiple Li ion pathways. Besides, AB and $LiMn_2O_4$ nanoparticles are easily aggregated during charge/discharge processes. CNTs with a large aspect ratio can provide long-range conductivity, better interfacial contact between $LiMn_2O_4$ nanoparticles and conducting pathways. At the same time, they can create more stable network structures for dispersing $LiMn_2O_4$ nanoparticles. Hence, CNTs are an ideal material to improve the electrical conductivity of the $LiMn_2O_4$ cathode. In addition to CNTs, graphene with superior electrical conductivity and high surface area can provide a highly conductive matrix and offer a high contact area between electrolyte and electrode, facilitating the transportation of Li ions and electrons in the electrode. Graphene is

also an ideal template to construct a hybrid material with good dispersion of $LiMn_2O_4$ nanoparticles and improved electrical conductivity.

This thesis is focused on preparation of new carbon materials (CNTs and graphene) as conductive additives to improve the rate performance of the $LiMn_2O_4$ cathode and includes two parts. The first part is focused on the preparation of CNTs by a chemical vapor deposition (CVD) method and its use as a new conductive additive to increase the rate performance of the $LiMn_2O_4$ cathode. Firstly, a three-dimensional hierarchically structured CNT/AB network was fabricated to increase the conductive contacts among $LiMn_2O_4$ nanoparticles and provide conductive pathways for fast electron transfer. The 3.3wt%CNT/AB/$LiMn_2O_4$ electrode exhibited excellent rate capability (specific discharge capacity of 105 and 73 mAh g^{-1} at 10 C and 20 C, respectively) and cyclability (Coulombic efficiency of almost 100% over 300 charge/discharge cycles at 4 C), in comparison with the cathodes prepared previously. Additionally, the initial specific discharge capacity researched 139 mAh g^{-1}, which has never been reported in the literature. When the content of CNTs reduced to 2 wt%, the 2wt%CNT/AB/$LiMn_2O_4$ electrode still exhibited at least 23% higher rate capability than that of the traditional 10wt%AB/$LiMn_2O_4$ electrode.

Then, highly robust, binder-free flexible $LiMn_2O_4$/CNT electrodes were synthesized and used in the aqueous battery for the first time. The excellent electrical conductivity of the electrodes facilitates electron transport, resulting in a high rate capability. Besides, it can be bent and twisted under mechanical stress, which makes it possible to be used in flexible devices.

The second part of the thesis is focused on the preparation of graphene and its use as new conductive additives to increase the rate performance of the $LiMn_2O_4$ cathode. Firstly, three different kinds of graphene were prepared and used as conductive additives of the $LiMn_2O_4$ cathode of the ReHAB, which are exfoliated graphene (EG), reduced graphene oxide (RGO) and porous graphene (PG). PG prepared from the CVD method exhibited excellent conductivity and porous structure, resulting in significantly better rate capability and cyclability of the ReHAB than those using EG and RGO.

In order to further improve the rate capability of the ReHAB, PG/AB conductive networks were prepared by simple mechanical mixing. The rate performance of the $LiMn_2O_4$ cathode was obviously improved when PG and AB coexisted as conductive additives. The PG/AB conductive network can provide: (1) conductive contacts between $LiMn_2O_4$ and AB nanoparticles; (2) conductive contacts between $LiMn_2O_4$ nanoparticles and PG nanosheets; (3) physical contacts between AB nanoparticles and PG nanosheets. The PG/AB conducting network facilitated the transfer of electron, resulting in an excellent rate performance of the ReHAB. When the content of the PG reduced to 1 wt%, the 1wt%PG/AB/$LiMn_2O_4$ electrode still exhibited at least 19% higher rate capability than the traditional 10wt%AB/$LiMn_2O_4$ electrode.

It is worth mentioning that the CNT/AB/$LiMn_2O_4$ and PG/AB/$LiMn_2O_4$ electrodes were prepared by a simple mechanical mixing method, which is effective and inexpensive in comparison with other complicated preparation approaches, paving the way for easy scale-up of the process.

Acknowledgments

Firstly, I would show my deepest gratitude to Prof. Pu Chen, my supervisor, for his constant encouragement and guidance through my research work. Special thanks are extended to Positec and the China Scholarship Council for the financial support. Besides, I would thank to University of Waterloo for offering me abundant resources and professional research platform.

Secondly, I would like to thank my committee members, Prof. Xueliang Sun, Prof. Xianguo Li, Prof. Eric Croiset, and Prof. Leonardo Simon for their time and valuable comments and advices on my thesis.

Thirdly, I would like to express my heartfelt thanks to all of the members of the aqueous battery research group, past and present: The Nam Long Doan, Tuan K. A. Hoang, Ye Tian, Yan Yu, Zhixu Han, Kyung Eun Kate Sun, Aishuak Konarov, Sameh Saad, Xianwen Wu, Hongbin Zhao, and Jian Zhi. I am so grateful that they gave me a lot of help during my Ph.D study. Expecially thanks are given to Dr. Nam Long Doan and Dr. Tuan K. A. Hoang, who dedicated on my paper and thesis revision; as well as Dr. Ye Tian and Dr. Xianwen Wu, who taught me most valuable experimental skills.

Last but not the least, I would thank my beloved family for their loving considerations and great confidence in me all through these years. Without them, none of my achievements would be possible. The thesis is dedicated to all of them.

Dedication

Dedicated to My Beloved Family Members

Table of Contents

List of Figures

List of Tables

List of Abbreviations

ReHAB: Rechargeable Hybrid Aqueous Battery

ARLB: Aqueous Rechargeable Lithium ion Battery

AB: Acetylene Black

CNT: Carbon Nanotube

SWNT: Single-walled Carbon Nanotube

MWNT: Multi-walled Carbon Nanotube

PG: Porous Graphene

EG: Exfoliated Graphene

RGO: Reduced Graphene Oxide

0-D: zero-dimensional

1-D: one-dimensional

2-D: two-dimensional

3-D: three-dimensional

CNT/AB/$LiMn_2O_4$ electrodes: mechanical mixing 83 wt% $LiMn_2O_4$ with 10 wt% carbon conductor consisting of CNTs and AB with different weight ratios (CNTs : AB = 1 : 9, 1 : 4, 1 : 2, 1 : 0, and 0 : 1), and 7 wt% PVdF. The electrodes prepared are indicated as the 1wt%CNT/AB/$LiMn_2O_4$, 2wt%CNT/AB/$LiMn_2O_4$, 3.3wt%CNT/AB/$LiMn_2O_4$, 10wt%CNT/$LiMn_2O_4$, and 10wt%AB/$LiMn_2O_4$ electrodes, corresponding to electrodes with different weight ratios of CNTs to AB as 1 : 9, 1 : 4, 1 : 2, 1 : 0, and 0 : 1.

Flexible $LiMn_2O_4$/CNT electrodes: The electrodes contained 10 wt% CNT and 90 wt% $LiMn_2O_4$ were prepared by vacuum filtration method.

7wt%CNT/$LiMn_2O_4$ electrode: mechanical mixing 86 wt% $LiMn_2O_4$ with 7 wt% CNTs and 7 wt% PVdF.

7wt%AB/$LiMn_2O_4$ electrode: mechanical mixing 86 wt% $LiMn_2O_4$ with 7 wt% AB and 7 wt% PVdF.

PG/AB/$LiMn_2O_4$ electrodes: mechanical mixing 83 wt% $LiMn_2O_4$ with 10 wt% carbon conductor consisting of PG and AB with different weight ratios (PG : AB = 0.5 : 9.5, 1 : 9, 1 : 2, 1 : 0, and 0 : 1), and 7 wt% PVdF. The electrodes prepared are indicated as the 0.5wt%PG/AB/$LiMn_2O_4$, 1wt%PG/AB/$LiMn_2O_4$, 3.3wt%PG/AB/$LiMn_2O_4$, 10wt%PG/$LiMn_2O_4$, and 10wt%AB/$LiMn_2O_4$ electrodes, corresponding to electrodes with different weight ratios of PG to AB as 0.5 : 9.5, 1 : 9, 1 : 2, 1 : 0, and 0 : 1.

PVdF: Polyvinylidene Fluoride

NMP: 1-methyl-2-pyrrolidinone

AGM: Absorbed Glass Mat

SSA: Specific Surface Area

EV: Electric Vehicle

CVD: Chemical Vapor Deposition

DFT: Density Functional Theory

SEM: Scanning Electron Microscopy

TEM: Transmission Electron Microscopy

HRTEM: High Resolution Transmission Electron Microscopy

EDS: Energy Dispersive Spectroscopy

XRD: X-ray Diffraction

BET: Brunauer-Emmet-Teller

EIS: Electrochemical Impedance Spectroscopy

CV: Cyclic Voltammetry

SHE: Standard Hydrogen Electrode

SCE: Standard Calomel Electrode

Chapter 1

Introduction and Motivation

1.1 Overview

The excessive depletion of resources (*e.g.*, oil and coal) prompts people to explore new sustainable energies. Renewable energy sources (*e.g.*, solar and wind) have aroused widespread interests among scientists. However, the solar and wind energy change with time and season, so large-scale energy storage systems (*e.g.*, batteries and capacitors) with high power and safety, as well as low cost are urgently needed to store these energies and connect them to the power grid **[1]**. Lithium ion batteries have been widely used in electronic devices and have been chosen as one of the most promising power sources for electric vehicles (EVs) due to the high energy density achieved from the high operation voltage of the organic electrolytes. However, these organic electrolytes have high flammability and toxicity, as well as low ionic conductivity (about two orders of magnitude lower than that of aqueous electrolytes); besides, the fabrication cost of lithium ion batteries is high, which makes them not suitable to be used as large-scale energy storage systems. Alternatively, aqueous electrolytes show higher safety (non-flammable, low toxic) and ionic conductivity, as well as lower cost than organic electrolytes. Although aqueous electrolytes can only operate at a lower voltage than organic electrolytes, they are more suitable to be used as large-scale energy storage systems that require high safety at low cost, and high power density, while energy density is not as critical as EVs **[2-16]**.

So far, various types of aqueous batteries, including alkaline Zn-MnO_2, lead-acid, nickel-metal hydride (Ni-MH), nickel metal (*e.g.*, cadmium, iron, zinc, and cobalt) and several metal-ion (*e.g.*, Li^+, Na^+, K^+, and Zn^{2+}) aqueous batteries on the basis of metal-ion intercalation chemistry, are

commercially available or under extensive research **[6, 17-32]**. However, they have been encountering different kinds of challenges. Specifically, alkaline Zn/MnO_2 is a primary battery, and its disposal cause plenty of pollution to the environment; the poisoning metal of cadmium utilized in Ni-Cd battery may cause damage to the environment; Ni-MH (M= La, Ce, Nd, Gd *etc.*) batteries utilize rare earth elements, which makes them expensive; Ni-Co (Fe, Zn) batteries and metal-ion aqueous batteries have narrow voltage range. Among all the aqueous batteries, lead-acid batteries have been widely used as large-scale energy storage systems; however, the utilization of poisoning metal of lead may also cause environmental problems.

Therefore, new battery chemistry and architecture are required for aqueous rechargeable batteries with high power as well as safety and eco-friendliness. A new secondary aqueous $Zn/LiMn_2O_4$ battery system, called Rechargeable Hybrid Aqueous Battery (ReHAB), has been developed by our group **[34]**. The mechanism of this battery system differs from that of the "rocking-chair" type batteries. At the anode, zinc is the active material, dissolved rapidly in a mild aqueous solution containing zinc ions during discharge and deposited reversibly during charge. At the cathode, Li ions can be reversibly intercalated into and de-intercalated from the tunnels of $LiMn_2O_4$ in the same electrolyte system. The electrolyte in this battery is more than an ionic conductive medium; it is also the source of the anode, being consumed and regenerated during battery cycling.

Thanks to its low cost, abundance, environmental friendliness, and stability, $LiMn_2O_4$ has been considered as one of the most promising cathode materials in aqueous batteries for large-scale energy storage **[2, 12, 13, 19, 33, 34]**. However, the rate capability of the $LiMn_2O_4$ cathode is intrinsically low, which leads to the low power density of the ReHAB. In particular, the

sluggish Li ion and electron diffusion in the cathode materials leads to insufficient Li ion intercalation/de-intercalation under high charge/discharge rates, which cannot satisfy the requirements for energy storage system that can transfer (store or release) energy at high rates **[35-37]**. To solve such problems, rapid ion diffusion and electron transport are necessary for the application of $LiMn_2O_4$ materials. Generally, two methods are employed to increase the rate capability of $LiMn_2O_4$ cathodes.

One method is to reduce the particle size of $LiMn_2O_4$ from micrometer to nanometer to reduce the Li ion diffusion distance, resulting in faster Li ion diffusion. These nanostructures include one-dimensional (1-D) nanotubes, nanorods, and nanochains; two-dimensional (2-D) nanosheets as well as nanoporous structures. They have displayed better rate capability than traditional micrometer-sized materials **[11, 12, 34, 38].** However, the nanostructure engineering of electrochemically active materials may increase the cost and the preparation process is complicated.

The other method is to add conductive additives to $LiMn_2O_4$ cathodes to improve the electrical conductivity **[39]**. Traditionally, the electron-transport pathways are constructed by mixing active electrode materials with conductive additives (mainly carbon materials) and polymeric binders **[40]**. However, the conductivity of conventional carbon additives, such as acetylene black (AB), is relatively lower than that of higher crystalline forms of carbon; and AB cannot provide long-range conductivity. Besides, nano-sized AB and $LiMn_2O_4$ both easily aggregate to bulk structure during charge/discharge cycles. As a new kind of highly crystalline forms of carbon materials, carbon nanotubes (CNTs) have been widely used as conductive additives in Li ion battery systems **[41]**. They are composed of sp^2-bonded carbon atoms assembled into a

cylindrical tube with length ranging from less than 100 nm to several centimeters, and diameter ranging from ~0.4 nm to nearly 100 nm, depending on the synthesis conditions. The large aspect ratio of CNTs contributes to long-range conductivity, better interfacial contacts between active materials and conducting pathways **[42]**. In addition, they can create more stable network structures for dispersing active materials, which can effectively decrease aggregation of nano-sized $LiMn_2O_4$. Hence, CNTs are an ideal material to improve the electrical conductivity of battery electrodes. Recently, there have been some reports about the excellent performance of $LiMn_2O_4$/CNT composites in aqueous rechargeable lithium ion batteries **[39, 43]**. Except for CNTs, graphene, a monolayer of sp^2-bonded carbon atoms arranged in hexagonal lattice, shows superior electrical conductivity, high surface area and good mechanical flexibility **[44]**. These characteristics can provide a highly conductive matrix and offer a high contact area between electrolyte and electrode, facilitating the transportation of Li ions and electrons into the electrode. Thus, graphene is also attractive as an ideal template to construct a hybrid material with good dispersion of nano-sized $LiMn_2O_4$ and improved electrical conductivity **[45-47]**. So far, $LiMn_2O_4$/graphene composites have been prepared and studied as the cathode of aqueous rechargeable batteries. The electrochemical performance, especially the rate capability of $LiMn_2O_4$ was improved by graphene modified **[48-51]**.

In this research, in order to improve the rate capability of the $LiMn_2O_4$ cathode of the ReHAB, CNTs and graphene were prepared and evaluated as conductive additives in the $LiMn_2O_4$ cathode.

1.2 Research Objectives

The overall goal of this research was to improve the rate capability of the $LiMn_2O_4$ cathode of the ReHAB, achieving a high power ReHAB system. To achieve this goal, CNTs and graphene were synthesized and tested as conductive additives in the $LiMn_2O_4$ cathode of the ReHAB. The specific objectives are listed as follows:

(1) Achieve power/energy densities of 20% higher than the traditional electrodes (mechanical mixed $LiMn_2O_4$, AB, and polymeric binder), using new conductive additives (CNTs and graphene).

(2) Explore facile and low cost methods to synthesize CNTs and graphene and control the content of CNTs or graphene in the electrodes as low as possible. Thus, the cost of these electrodes is comparable to the traditional electrodes.

(3) Optimize the electrode structures to be more favorable for Li ion diffusion and electron transport. Investigate the interaction between $LiMn_2O_4$ and conductive nanocarbon materials, based on Li ion diffusion and electron transport, through cyclic voltammetry (CV) measurement and electrochemical impedance spectroscopy (EIS).

1.3 Outline of the Thesis

The thesis consists of chapters as follows:

Chapter 1 gives an overview of the thesis and the main objectives of the research.

Chapter 2 reviews the basic development of battery, introduces the new aqueous battery system, ReHAB, its structure and mechanism. Besides, this chapter gives a detailed summary of the active material of $LiMn_2O_4$ and conductive additives of CNTs and graphene.

In Chapter 3, a three-dimensional hierarchically CNT/AB network is fabricated to increase the rate capability of the $LiMn_2O_4$ cathode for the ReHAB, using a simple mechanical mixing method. The structure and the electrochemical performances of CNT/AB/$LiMn_2O_4$ electrodes are investigated.

In Chapter 4, highly flexible $LiMn_2O_4$/CNT electrodes are developed and used as a high power cathode for the ReHAB. The physical properties and the electrochemical performances of the flexible electrodes are measured.

In Chapter 5, three different kinds of graphene, including porous graphene (PG), reduced graphene oxide (RGO), and mechanically exfoliated graphene (EG), are prepared and evaluated as conductive additives of the $LiMn_2O_4$ cathode for the ReHAB. The morphologies and properties, as well as the electrochemical performances of these three kinds of graphene are measured and compared.

In Chapter 6, PG/AB conductive networks are constructed to further improve the rate capability of the $LiMn_2O_4$ cathode for the ReHAB. The structure and the electrochemical performances of PG/AB/$LiMn_2O_4$ electrodes are investigated.

Chapter 7 gives the conclusions of the thesis and provides an outlook of the future of the ReHAB in large-scale energy storage systems.

Chapter 2

Background and Literature

2.1 General Introduction of Aqueous Rechargeable Battery

Batteries are good energy storage systems, which can store electricity in the form of chemical energy. Lithium ion batteries can operate at high voltages due to the wide electrochemical stability range of the organic electrolytes (3-5 V vs. standard hydrogen electrode, SHE), resulting in high energy densities. Therefore, lithium ion batteries have been widely used in electronic devices and they have been considered as one of the most promising power sources for Electric Vehicles (EVs). Unfortunately, these organic electrolytes show high flammability and low ionic conductivity (about two orders of magnitude lower than that of aqueous electrolytes); besides, the fabrication cost of lithium ion batteries is high, which makes them not suitable to be used as large-scale energy storage systems. Alternatively, aqueous electrolytes are electrochemically stable in narrower voltage (1.23 V vs. SHE) than organic electrolytes; however, they are much safer (non-flammable and low toxic) and the fabrication cost of aqueous batteries is much lower than lithium ion batteries, so aqueous batteries are more suitable for large-scale energy storage **[1-3]**. Various types of aqueous batteries, including alkaline Zn-MnO_2, lead-acid, nickel-metal hydride (Ni-MH) and nickel metal (*e.g.*, cadmium, iron, zinc, and cobalt) are commercially available or under extensive research **[1, 4-8]**. However, they have been encountering different kinds of challenges. Specifically, alkaline Zn/MnO_2 is a primary battery, and its disposal cause plenty of pollution to the environment; the poisoning metal of cadmium utilized in Ni-Cd battery may cause damage to the environment; Ni-MH (M= La, Ce, Nd, Gd *etc.*) batteries utilize rare

earth elements, which makes them expensive; Ni-Co (Fe, Zn) batteries have narrow voltage range.

Recently, a series of aqueous "rocking-chair" batteries based on the ion (*e.g.*, Li^+, Na^+, K^+, and Zn^{2+}) interaction/de-intercalation processes have been developed **[9-20]**. In 1994, Dahn *et al.* first developed the aqueous lithium ion battery **[9]**, using VO_2 as anode and $LiMn_2O_4$ as cathode, 5 mol L^{-1} $LiNO_3$ solution as electrolyte. Then, a variety of aqueous ''rocking-chair'' lithium ion batteries (*e.g.*, $LiFePO_4/LiTi_2(PO_4)_3$, $LiMn_2O_4/LiTi_2(PO_4)_3$, and $LiMn_2O_4/LiV_3O_8$) have been reported; however, they showed poor cycling stability **[9-12]**. An aqueous potassium ion battery was developed by Cui *et al.*, in which carbon/polypyrrole hybrid and copper hexacyanoferrate were used as anode and cathode, respectively, exhibited an excellent rate capability **[14]**. In contrast to aqueous lithium (potassium) ion batteries, aqueous sodium ion batteries are more promising to be used as large-scale energy storage systems due to the abundance of sodium in nature. Whitacre's and Chiang's groups both reported aqueous $Na_{0.44}MnO_2/NaTi_2(PO_4)_3$ batteries **[18, 19]**. However, sodium-intercalated compounds for aqueous systems are limited, unique Li/Na mixed ion batteries, $Na_{0.44}MnO_2/TiP_2O_7$ and $LiMn_2O_4/Na_{0.22}MnO_2$, were developed by Xia's group, which mainly depend on the intercalation/de-intercalation of Na ions and Li ions, respectively. The specific energy of these two batteries was 25 and 17 Wh kg^{-1} based on the total weight of the active materials, respectively. It is worth mentioning that Li ions and Na ions are separated in aqueous $LiMn_2O_4/Na_{0.22}MnO_2$ battery due to the special operating mechanism of this system **[21]**. Besides, Cui *et al.* found that materials with the Prussian Blue crystal structure (nickel hexacyanoferrate and copper) possess large interstitial sites, which allows for the

intercalation/de-intercalation of sodium (potassium) ions **[20, 22]**. Their capacities are in the range of 50-60 mAh g^{-1}.

2.2 Introduction of Rechargeable Hybrid Aqueous Battery

New battery chemistry and architecture are required for aqueous rechargeable batteries with high power as well as safety and eco-friendliness. Herein, rechargeable Zn/MnO_2 batteries have been widely studied, however, the poor reversibility of the redox reaction on the cathode hinders its commercial applications. In neutral or alkaline electrolytes, $Zn(OH)_2$, ZnO_2^{2-}, and $[Zn(OH)_4]^{2-}$ are formed depending on potential and pH value; while in acidic solutions, $Zn - 2e^- \rightleftharpoons Zn^{2+}$ **[23]**. Minakshi *et al.* found that replacing MnO_2 by $LiMn_2O_4$ and changing the electrolyte to aqueous LiOH/$ZnSO_4$ solution could improve the reversibility; however, due to the high pH value of the electrolyte, only a few amount of cathode material can be used during charge/discharge processes **[23]**. Recently, Kang *et al.* developed a mild zinc ion battery, using **α**-MnO_2 as cathode and Zn as anode **[15]**, which showed high capacities and a high rate capability. Additionally, a new secondary aqueous Zn/$LiMn_2O_4$ battery system, called Rechargeable Hybrid Aqueous Battery (ReHAB) has also been reported by our group (**Fig. 2.1**) **[24]**. The mechanism of this battery system differs from that of the "rocking-chair" type batteries. At the anode, zinc is the active material, dissolved rapidly in a mild aqueous solution containing zinc ions during discharge and deposited reversibly during charge. At the cathode, Li ions can be reversibly intercalated into and de-intercalated from the tunnels of $LiMn_2O_4$ in the same electrolyte system. The electrolyte in this battery is more than an ionic conductive medium. It is also the source of the anode, being consumed and regenerated during battery cycling.

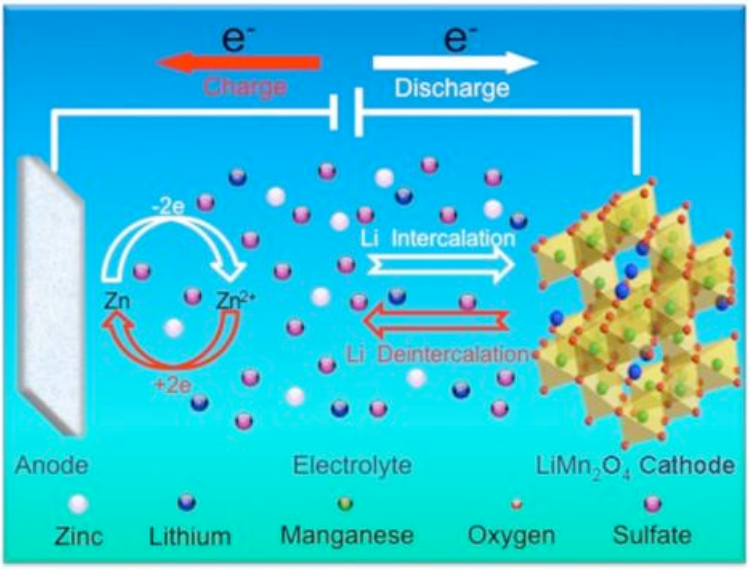

Fig. 2.1 Schematic representation of the proposed mechanism for ReHAB operation. (Modified from **Ref. [24]**)

2.2.1 Anode and Cathode of the ReHAB

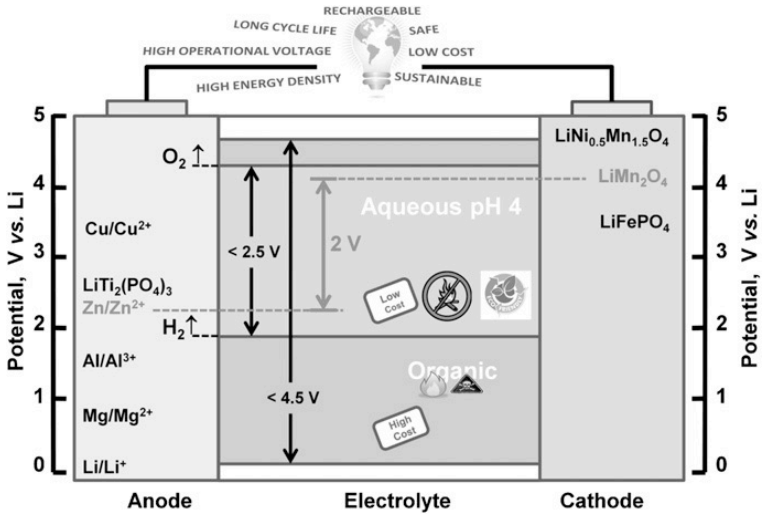

Fig. 2.2 Comparison of aqueous and organic electrolyte; the operation voltage range of the Zn/$LiMn_2O_4$ (ReHAB) is also shown. (Reprinted from **Ref. [24]**)

As we mentioned previously, aqueous batteries are more suitable than lithium ion batteries for large-scale energy storage due to the safety and low cost. Theoretically, the electrodes with an intercalation potential between 3 and 4 V (vs. Li^+/Li) before the oxygen evolution (*e.g.*, $LiMn_2O_4$ and $LiFePO_4$) can be used as cathode materials for aqueous lithium ion batteries. Compared to $LiFePO_4$, $LiMn_2O_4$ can provide a higher energy density due to the higher redox potential. Besides, the volume change of $LiMn_2O_4$ during charge/discharge processes is only about 7%, which is much lower than that in the PbO_2 electrodes (about 90%) of lead acid batteries **[25, 26]**. Therefore, $LiMn_2O_4$ is chosen as the cathode material of the ReHAB. In terms of anode materials, electrodes with an intercalation potential between 2 and 3 V (vs. Li^+/Li) before the hydrogen evolution (*e.g.*, carbon, LiV_3O_8, TiP_2O_7, and $LiTi_2(PO_4)_3$) can be chosen as the anode materials for aqueous lithium ion batteries. However, the large volume changes of these anode materials during charge/discharge processes result in a low reversibility, inhibiting their utilization in aqueous lithium ion batteries **[12]**. Alternatively, the deposition/dissolution processes of metal electrodes (*e.g.*, Li, Mg, Al, Zn, and Cu) are highly reversible in aqueous electrolytes. Based on the reduction potential of the metal, the over-potential for hydrogen evolution on the metal, and the solution pH, zinc is chosen as the most suitable anode material for the ReHAB **[27]**.

2.2.2 Electrolyte Formulation of the ReHAB

The electrolyte of the ReHAB consists of Li_2SO_4 (2 mol L^{-1}) and $ZnSO_4$ (1 mol L^{-1}), and pH equals 4. The solubility of Zn^{2+} is limited due to the low solubility product, K_{sp} (25 ^oC), which can be expressed as $[Zn^{2+}]\ [OH^-]^2 = K_{sp} = 3 \cdot 10^{-17}$. Furthermore, the relationship between the saturation concentration of Zn^{2+} and the pH of the solution can be expressed as $[Zn^{2+}]_{saturated} = 3 \cdot 10^{11-2pH}$, so the pH should be lower than 5.5 to provide plenty amount of zinc ions for the

ReHAB operation. Conversely, $LiMn_2O_4$ and zinc may react with proton as follows in an extremely acid solution:

$$2LiMn_2O_{4(s)} + 4H^+_{(aq)} \rightarrow 3MnO_{2(s)} + Mn^{2+}_{(aq)} + 2Li^+_{(aq)} + 2H_2O_{(aq)} \quad (2.1)$$

$$Zn + 2H^+ \rightarrow Zn^{2+} + H_{2(g)} \quad (2.2)$$

Therefore, the pH must be high enough to prevent these side reactions. Considering the stability of $LiMn_2O_4$ and zinc in acid aqueous solutions, the pH of the electrolyte is adjusted to 4 **[24]**.

2.2.3 Cell Operating Voltage of the ReHAB

At the anode, according to the Nernst equation:

$$E_{Zn^{2+}/Zn} = E°_{Zn^{2+}/Zn} + (RT/nF) \ln[Zn^{2+}] \quad (2.3)$$

where $E°_{Zn^{2+}/Zn}$ equals -0.76 V (vs. SHE), R refers to the universal gas constant (8.314 J $(mol \cdot K)^{-1}$), T refers to the Kelvin temperature (298.15 K), F refers to the Faraday constant (96000 C mol^{-1}), and n refers to the number of moles of electrons transferred in the redox reaction, which can be expressed as $Zn^{2+} + 2e^- \rightleftharpoons Zn°$ (n = 2). Therefore, the reduction potential can be calculated as $E_{Zn^{2+}/Zn}$ = -0.76 V (vs. SHE) with the concentration $[Zn^{2+}]$ = 1 mol L^{-1} at 25 ^oC.

At the cathode, Li ions intercalate and de-intercalate into/from the tunnels of $LiMn_2O_4$ by two steps, which can be expressed as follows **[28, 29]**:

$$LiMn_2O_4 \rightleftharpoons Li_{0.5}Mn_2O_4 + 0.5Li^+ + 0.5e^- \quad (2.4)$$

$$Li_{0.5}Mn_2O_4 \rightleftharpoons Mn_2O_4 + 0.5Li^+ + 0.5e^- \quad (2.5)$$

The reduction potential of this process can be expressed as:

$E_{interc} = E°_{interc} + (RT/nF)\ln[Li^+]$ (2.6)

where $E°_{interc}$ shows a potential range (about 0.85-1.1 V, *vs*. SHE) due to the two-step intercalated processes. Therefore, the E_{interc} shows a range of about 0.89-1.14 V (*vs.* SHE) with the concentration of $[Li^+]$ =2 mol L^{-1} at 25 ^oC.

Therefore, the operating voltage of the ReHAB is about 1.8 V, combining the zinc anode and $LiMn_2O_4$ cathode **[24]**.

2.2.4 Energy Density Calculations of the ReHAB

The mass energy density of a battery is expressed as follows:

$$\text{Energy Density} = \frac{\text{Cell Capacity} \times \text{Operating Voltage}}{\text{Total Mass of Cell Components}}$$

The cell capacity of a battery is dependent on the specific capacity of the active materials. Hence, for a Zn/$LiMn_2O_4$ battery (ReHAB) with the capacity of 1Ah, the energy density can be calculated based on the specific capacities of $LiMn_2O_4$ and Zn, while the electrochemically inactive components such as separator, electrolyte and cell shells can be neglected. The mass of active material is calculated with Faraday's law expressed as follows:

$$\text{Specific Capacity} = \frac{\text{Number of electrons} \times \text{Faraday's constant}}{3600 \times \text{Formula Weight}} = \frac{\text{Current} \times \text{Time}}{\text{Mass}_{\text{Active Material}}}$$

$$\text{Mass of Active Material} = \frac{3600 \times \text{Formula Weight} \times \text{Current} \times \text{Time}}{\text{Number of electrons} \times \text{Faraday's constant}}$$

$$= \frac{\text{Current} \times \text{Time}}{\text{Specific Capacity}}$$

Mass of Active Cathode Material

The practical specific capacity of $LiMn_2O_4$ is about 120 mAh g^{-1}; so the mass of $LiMn_2O_4$ needed for a 1Ah battery is calculated as follows:

$$m_{LiMn_2O_4} = \frac{1Ah}{120mAh \cdot g^{-1}} = 8.3g$$

Mass of Active Anode Material

Since the cathode material is the limiting reagent and the electrolyte is the only source of anode material, a more direct approach is to determine the amount of zinc formed upon charging the battery. This is equivalent to the mass of $ZnSO_4$ reduced upon charge. Using Faraday's law we get:

$$m_{ZnSO_4 reduced} = \frac{Current \times Time \times 3600 \times Formula\ Weight}{Number\ of\ electrons \times Faraday's\ constant} = \frac{1 \times 3600 \times 161.47}{2 \times 96000} = 3.0\ g$$

Assuming 70% of $ZnSO_4$ is utilized, the amount of $ZnSO_4$ needed should be 4.3 g. The total mass of electrolyte is (the density of the electrolyte solution is 1.18 g mL^{-1},):

$$M_{Electrolyte\ Solution} = \frac{Mass_{ZnSO_4} \times Density_{solution}}{Formular\ Weight_{ZnSO_4} \times Molarity_{solution}} = \frac{4.3 \times 1.18 \times 1000}{161.47 \times 1} = 31.4\ g$$

Energy Density

Considering only the mass of active materials, the energy density of the ReHAB is:

$$Energy\ Density' = \frac{1Ah \times 1.8V}{(8.3 + 4.3)} = 143\ Wh \cdot kg^{-1}$$

Including the total mass of electrolyte, the energy density is:

$$\text{Energy Density}'' = \frac{1\text{Ah} \times 1.8\text{V}}{(8.3 + 31.4)} = 45\ \text{Wh} \cdot \text{kg}^{-1}$$

If we assume the weight of active materials accounts half of the total weight of commercial batteries. The practical energy density of the ReHAB can be estimated as 22-72 Wh.kg^{-1}.

2.3 Introduction of $LiMn_2O_4$

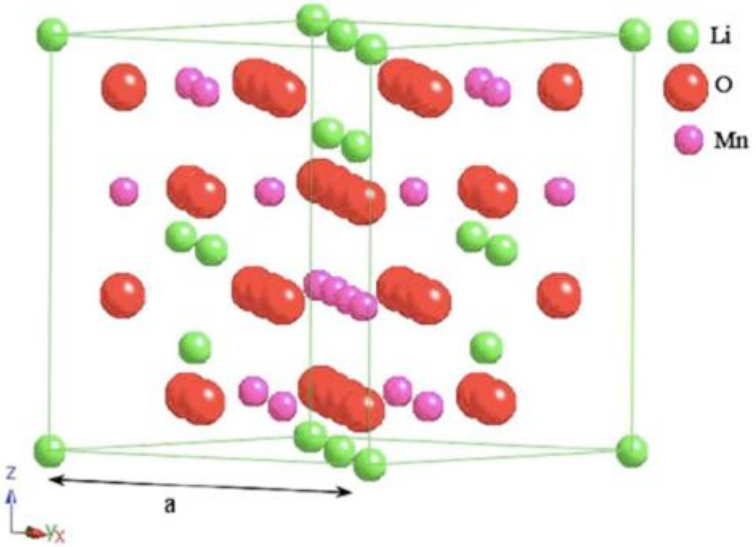

Fig. 2.3 The crystal structure of spinel $LiMn_2O_4$.

Compared with other cathode materials (*e.g.*, $LiCoO_2$ **[30-32]**, $LiNiO_2$ **[33]**, $LiFePO_4$ **[34]**, $NaMnO_2$ **[35],** and $KMnO_2$ **[36]**) in aqueous rechargeable batteries, spinel $LiMn_2O_4$ is the most promising cathode material for aqueous rechargeable batteries due to its safety, eco-friendliness, low cost, and excellent structural stability **[37]**. The crystal structure of spinel $LiMn_2O_4$ is illustrated in **Fig. 2.3**, one eighth of tetrahedral sites are occupied by Li ions and half of the octahedral interstitial sites are occupied by manganese cations; Li ions transfer in the three-dimensional (3-D) interstitial space provided by the Mn_2O_4 framework **[28, 29]**.

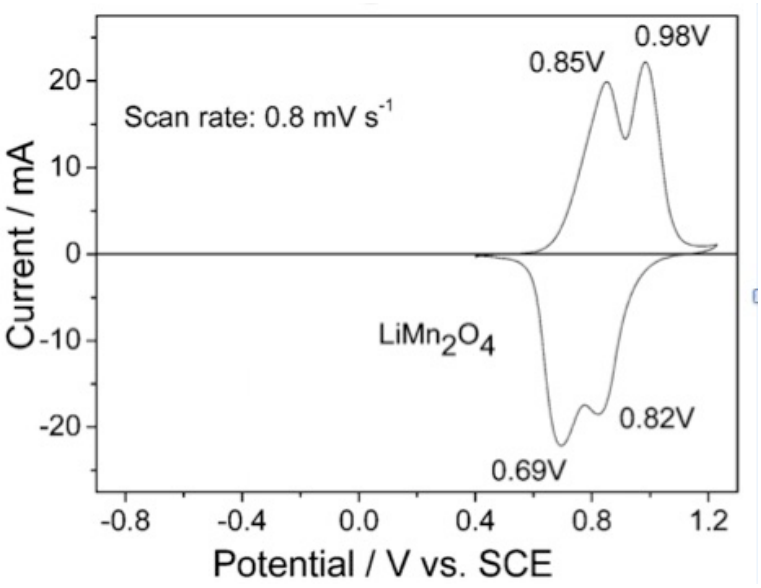

Fig. 2.4 CV curve of the micrometer $LiMn_2O_4$ in the saturated Li_2SO_4 solution. (Reprinted from **Ref. [38]**)

In 1994, it was reported that Li ion could de-intercalate/intercalate from/into $LiMn_2O_4$ in aqueous electrolyte for the first time **[9]**. In the CV curve of the $LiMn_2O_4$ in the saturated Li_2SO_4 solution (**Fig. 2.4**), two pairs of redox peaks at 0.85/0.69 V and 0.98/0.82 V (V vs. standard calomel electrode, SCE), respectively, represent the de-intercalation/intercalation of Li ions from/into the tunnels of $LiMn_2O_4$. Besides, the oxidation potentials are much lower than the oxygen evolution potential (~1.5 V vs. SCE), revealing the excellent stability of $LiMn_2O_4$ as the cathode for aqueous rechargeable batteries **[38]**.

However, the rate capability of the $LiMn_2O_4$ cathode is intrinsically low, which leads to the low power density of batteries. Specifically, the diffusion of Li ions and electrons in $LiMn_2O_4$ is slow, leading to the insufficient Li ion intercalation/de-intercalation under high current density,

which cannot satisfy the requirements for energy storage system that can transfer (store or release) energy at high rates **[39-41]**.

Generally, two methods are employed to increase the rate capability of $LiMn_2O_4$ cathode. One method is reducing the particle size of $LiMn_2O_4$ from micrometer to nanometer to reduce the Li ion diffusion paths, resulting in fast Li ion diffusion **[42]**. Another method is adding conductive additive (*e.g.*, acetylene black) to $LiMn_2O_4$ cathode to improve the transportation of electrons, thus the electrical conductivity **[43]**.

2.3.1 Preparation of Nanostructured $LiMn_2O_4$ to Increase the Li Ion Diffusion in $LiMn_2O_4$ Cathode

Traditionally, $LiMn_2O_4$ is prepared by the solid-state reaction, using lithium and manganese salts. Unfortunately, $LiMn_2O_4$ prepared by these processes shows large particle size and irregular morphology; besides, the stoichiometry is hard to control and the calcination time is long. To improve the structural stability of $LiMn_2O_4$ from solid-state synthesis, heteroatoms such as Ni, Cr, and Al could be doped into $LiMn_2O_4$, this strategy has been proved effectively in non-aqueous batteries **[44-46]**. However, the doped $LiMn_2O_4$ materials show lower capacities, because the concentration of Mn is compromised (via replacement by heteroatom). Recently, a series of chemical methods such as precipitation, spray pyrolysis, combustion, sol-gel, and hydrothermal process have been developed to prepare $LiMn_2O_4$ **[47-55]**. Among them, 1-D nanostructures including nanowires **[56]**, nanotubes **[57]**, nanorods **[58]**and nanochains **[59]** are more favorable due to the large aspect ratio (length-to-diameter ratio) that can facilitate the contact between electrolyte and $LiMn_2O_4$ and can also provide long-range conductive pathways

for the transportation of electrons **[60]**. For example, $LiMn_2O_4$ nanotube (TEM images in **Fig. 2.5a**) with a preferred orientation of (400) planes was prepared through using multi-walled carbon nanotubes as the self-template by Tang *et al.* **[57]**. Except for 1-D nanostructures, 2-D nanostructures, such as nanosheets, can also facilitate Li ion diffusion. It has been found by Sun *et al.* that single-crystalline porous $LiMn_2O_4$ nanosheets exhibited excellent electrochemical performance as cathode of lithium ion battery **[61]**. In consideration of the merits of 2-D nanosheets, such as well-defined geometry and perfect crystallization, spinel $LiMn_2O_4$ with single-crystalline nano-lamellar structure will be a wonderful cathode material for aqueous rechargeable batteries. The easily prepared MnO_2 nanosheets can be used as sacrificial templates for preparing $LiMn_2O_4$ nanosheets **[62].** Specifically, single-crystalline porous $LiMn_2O_4$ nanosheets (SEM images in **Fig. 2.5b**) with exposed (111) facets were reported by Sun *et al.* **[61].** Besides, porous $LiMn_2O_4$ consisting of nanograins was also prepared by using polystyrene particles as templates, whose morphology is shown in **Fig. 2.5c [37]**.

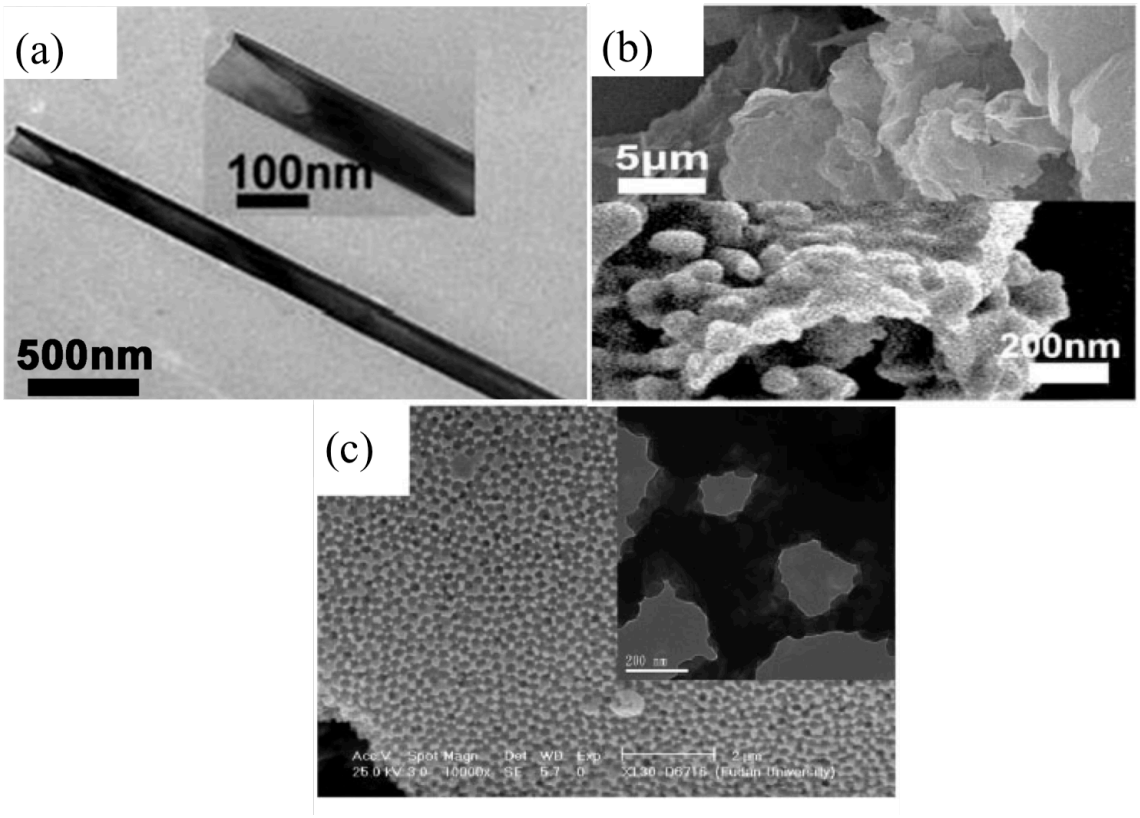

Fig. 2.5 (a) TEM images of the $LiMn_2O_4$ nanotube; SEM images of (b) the $LiMn_2O_4$ nanosheets and (c) the porous $LiMn_2O_4$. (Modified from **Ref. [37, 57, 61]**)

Compared to micrometer-sized materials, porous or nanostructured materials have exhibited superior electrochemical performances as electrode materials for energy storage systems, including higher capacities, better cycling stability and rate capability **[37, 58, 59, 63]**. The size effects within the framework of $LiMn_2O_4$ can explain this superior electrochemical performance (especially the rate capability) held by nanomaterials over micrometer-sized materials **[64]**. The particle size affects the time (t) for Li ion diffusion within a particle based on the relationship $t = L^2/D_{Li}$, where L refers to the length of Li ion diffusion, D_{Li} refers to the velocity of Li ion diffusion. Reducing the particle size from micrometer to nanometer can obviously decrease the time (t). This enhances the Li ion diffusion, which results in high rate capability of cathode

material.

When aqueous rechargeable lithium ion battery (ARLB) uses micrometer $LiMn_2O_4$ as cathode and active carbon (AC) as anode in a 1 mol L^{-1} Li_2SO_4 solution, the energy density is about 38 Wh kg^{-1} at a power density of 100 W kg^{-1}, and keeps 23 Wh kg^{-1} at a power density of 760 W kg^{-1} based on the total weight of the active materials of both electrodes **[65]**. As for the nanostructured $LiMn_2O_4$, when they are assembled into ARLBs, the power density is greatly improved. For example, the ARLB of AC//$LiMn_2O_4$ nanorod presents a very high power density in 0.5 mol L^{-1} Li_2SO_4, up to 14.5 kW kg^{-1} **[56, 58].** Specific charge/discharge capacities of AC//porous $LiMn_2O_4$ battery in 0.5 mol L^{-1} Li_2SO_4 aqueous solution are 89.7 and 112 mAh g^{-1}, respectively, at a current density of 10 A g^{-1} (about 90 C). The power density is up to 10 kW kg^{-1} **[37]**. The nanograins in the porous $LiMn_2O_4$ can inhibit the dissolution of Mn^{3+} in electrolyte by keeping them on the surface, and they can also buffer the strain caused by Jahn-Teller distortion during the charge/discharge processes, contributing to the structural stability **[37]**.

2.3.2 Using CNTs as Conductive Additive to Increase the Electrical Conductivity of $LiMn_2O_4$ Cathode

2.3.2.1 Structure and Properties of CNTs

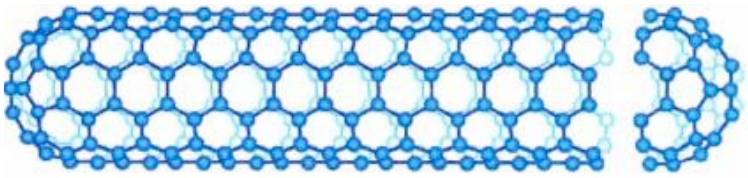

Fig. 2.6 The structural model of CNT.

Since being discovered by Sumio Iijima in 1991 **[66]**, carbon nanotubes (CNTs) have aroused great interest of researchers. CNTs can be envisaged as cylinders rolled by graphene sheets around a central hollow core, and ends with a structure of a hemisphere of fullerene (**Fig. 2.6**). The length of CNTs ranges from less than 100 nm to several centimeters, while the diameter of the hollow cores ranges from ~0.4 nm to nearly 100 nm, resulting in a high length-to-diameter ratio, or aspect ratio. Based on the number of graphene layers, CNTs can be classified into single-walled CNTs (SWNTs) and multi-walled CNTs (MWNTs). SWNTs consist of a single graphene layer, while MWNTs consist of two or more graphene layers **[67]**.

CNTs possess unusual physicochemical properties, including exceptionally high mechanical strength and high electrical conductivity. The chemical bonding of CNTs is composed mostly of sp^2 carbon bonds, which are stronger than the sp^3 carbon bonds found in diamond, resulting in amazing mechanical strength of CNTs. The free electrons formed π-electron system determines the electronic property; and the one-dimensional (1-D) tube structure facilities the transport of electrons, which contributes to the high electrical conductivity of CNTs. These unique properties make CNTs can be used in a wide range of applications, such as nanotechnology, energy storage, electronics, gas storage, water filtration, sensors, and so forth **[67, 68]**.

2.3.2.2 Growth Mechanism of CNTs

Based on the wide application of CNTs, mass production of CNTs with controlled structure becomes urgent. The techniques usually used to synthesize CNTs include arc-discharge **[66, 69]**, laser ablation **[70]**, gas-phase pyrolysis **[71]**, and chemical vapor deposition (CVD) **[72]**. Among these methods, CVD has become dominant for production of large quantities of CNTs at a low

cost. Wei *et al.* reported that more than thousands of tons of CNTs per year worldwide could be produced by a fluidized bed reactor-based CVD method, with the price of MWNTs below US \$100 kg^{-1} and that of SWNTs below US \$2000 kg^{-1} **[73]**.

The growth mechanism of CNTs based on CVD method has been widely studied all through these years **[74-76]**. According to different stages in the growth process, the growth mechanism can be classified into two different categories: atomic nucleation mechanism and tip- (base-) growth mechanism of CNTs on the molecular scale.

The nucleation process consists three stages: dissolution of carbon atoms, supersaturation of carbon atoms, and precipitation of carbon atoms to form CNTs **[77]**. The formation of the cap structure during the nucleation process of CNTs is a key step **[77, 78]**. In order to ensure the continuous growth of CNTs, carbon sources must be introduced continuously **[79]**.

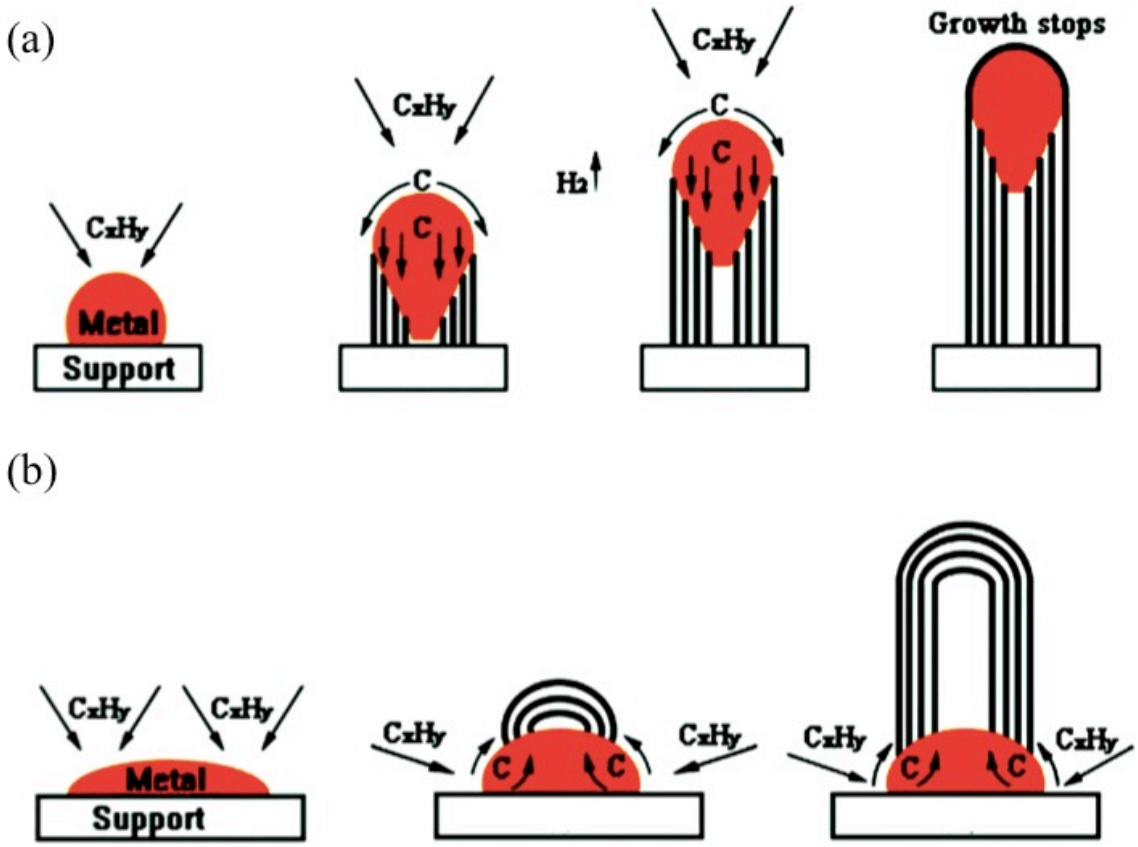

Fig. 2.7 Growth mechanisms for CNTs: (a) tip-growth mechanism and (b) base-growth mechanism. (Modified from **Ref. [80]**)

In a typical CVD run, transition metal (*e.g.*, nickel, molybdenum, and iron) is used as catalyst to catalyze the cracking reactions of hydrocarbon precursors (*e.g.*, C_2H_4 and CH_4) into carbon atoms and hydrogen. During the CVD process, if the interactions between catalyst and substrate are weak, the catalyst nanoparticles can keep floating in the gas flow, which refers to the tip-growth mode (**Fig. 2.7a**). On the other hand, , the catalyst will remain on their base due to the strong interactions between catalyst species and substrate, which refers to the base-growth mode (**Fig. 2.7b**) **[81]**. In the tip-growth mode, a thermal buoyancy is generated by the temperature difference between the gas flow and the substrate, which can help CNTs lift off from the

substrate surface and float in the gas flow **[82]**. The catalyst nanoparticles sit on top of the floating CNTs and continuously catalyze the growth of CNTs, which is favorable for the growth of ultra-long CNTs (**Fig. 2.8a**). As shown in **Fig. 2.8b**, the CNTs with length up to 550 mm were synthesized with furnace moving method **[83]**. It has been reported that the formation of SWNTs or MWNTs is depended on the size of the catalysts. Catalysts with small size (few nanometers) contribute to the formation of SWNTs, while MWNTs are more favorable to form on catalysts with the size larger than 10 nm **[81]**.

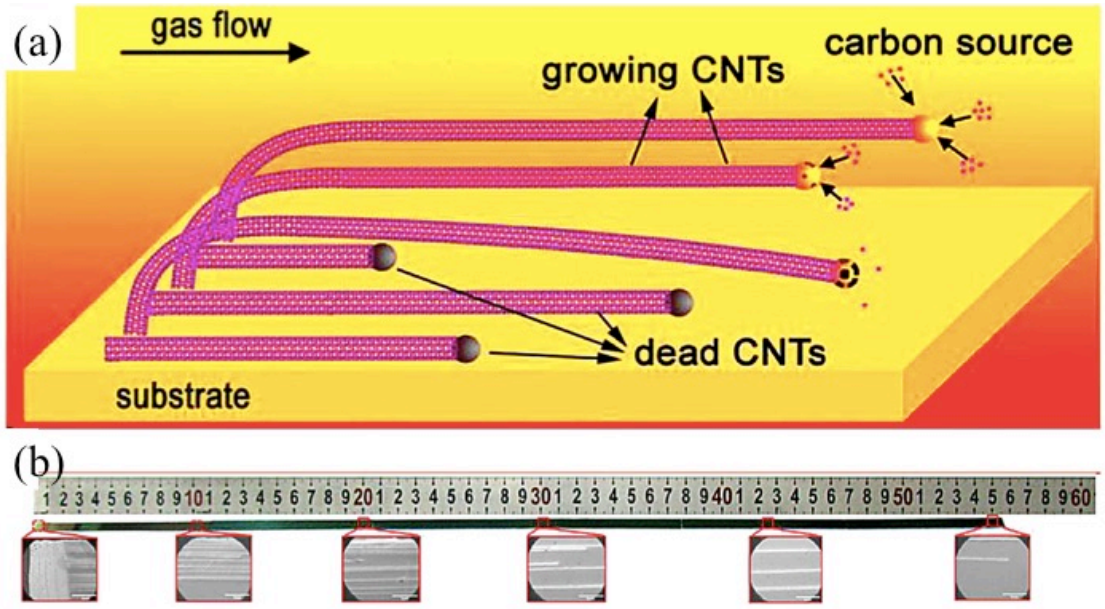

Fig. 2.8 (a) Illustration of tip-growth of ultra-long CNTs; (b) Mosaic scanning electron microscopy (SEM) images of 550 mm long CNTs. (Modified from **Ref. [83]**)

2.3.2.3 CNT Dispersion

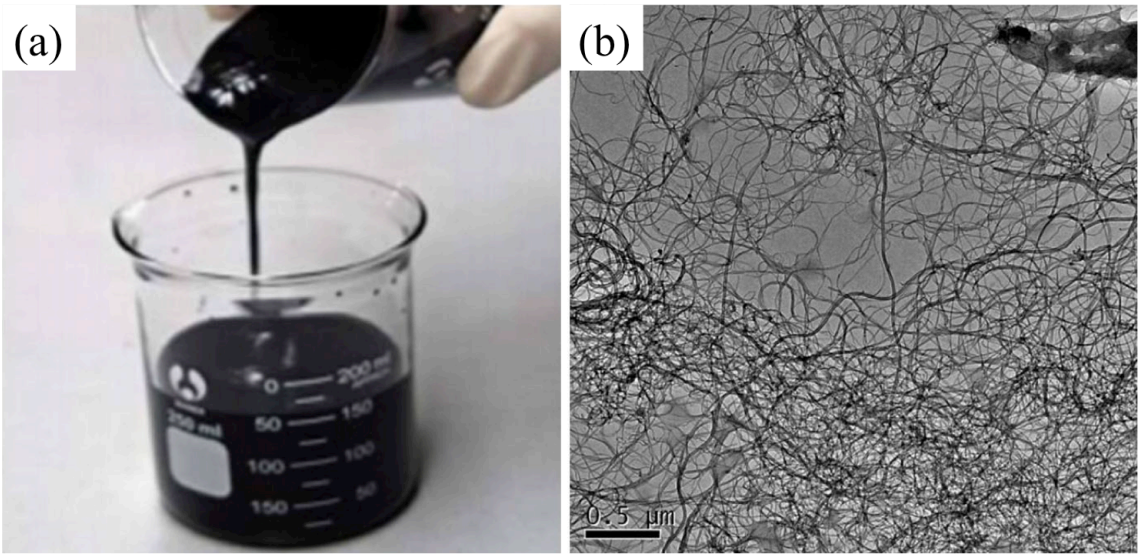

Fig. 2.9 (a) MWNTs dispersed in N-methyl-2-pyrrolidone (concentration of 1.0 mg mL^{-1}) by high-speed fluid shearing, displaying excellent dispersion; (b) Network structure of dispersed CNTs under TEM observation. (Reprinted from **Ref. [67]**)

Due to the large specific surface area, high length-to-diameter ratio, and strong p-p interactions between CNTs, CNTs are generally entangled together to form aggregates. It is a key issue to disperse CNTs uniformly before the utilization. Three conditions are required to obtain uniform dispersion of CNTs **[84]**: (1) destroy the entangled state of CNTs; (2) overcome Van der Waals forces among CNT aggregates; (3) obtain stable CNT dispersion.

Generally, CNTs are dispersed by mechanical methods **[84]**. The mechanical mixing method can only make the CNT aggregates macroscopically mix with the matrix powder, the CNT aggregates themselves cannot be dispersed; the ball milling and ultrasonic agitation methods both cut the CNTs into short length, which inevitably compromise the long-range conductivity of

CNTs. Besides, a high-speed fluid shearing process was used to disperse CNTs **[85]**. **Fig. 2.9a** shows that MWNTs are uniformly dispersed into N-methyl-2-pyrrolidone by a high-speed fluid shearing process, which is owe to the continuously network structures formed by CNTs (**Fig. 2.9b**) **[67]**. However, the organic solvent used in this process is toxic, which may cause damage to the environment in manufacturing.

Alternatively, chemical modifications are used to disperse CNTs. Among which, surface modification of CNTs by acid (alkali) is a highly efficient method **[86]**. The functional groups (*e.g.*, carboxyl and hydroxyl) introduced by the surface modification make CNTs disperse in solvents more easily **[87]**. However, the introduced defects in the structure of CNTs during chemical modification may compromise the electrical conductivity.

2.3.2.4 $LiMn_2O_4$/CNT Nanocomposites

Recently, $LiMn_2O_4$/CNT composites have been prepared by the following methods: mechanical alloying CNTs and $LiMn_2O_4$ powder in stainless steel mixing jars containing steel milling balls **[88]**, self-assembly process combined with solid-state lithiation **[89]**, in-situ hydrothermal method by using MnO_2/CNT and LiOH as reaction **[64, 90, 91]**, microwave-assisted hydrothermal reactions **[92, 93]**, spray-deposition method **[94]**, and in-situ hydrothermal growth of binder-free flexible $LiMn_2O_4$/CNT composite **[95]**. These composites have been used as cathode materials for lithium ion batteries, where better utilization of $LiMn_2O_4$ was attained.

Additionally, $LiMn_2O_4$/CNT composites have been used in aqueous rechargeable batteries to improve the electrochemical performance of the batteries. Zhang *et al.* prepared $LiMn_2O_4$/MWNTs composite by a mechanical activation reaction with a heat treatment **[96]**. The

$LiMn_2O_4$/MWNTs cathode was investigated in 1 mol L^{-1} Li_2SO_4 for aqueous rechargeable batteries, exhibiting a higher discharge capacity (117 mAh g^{-1}) than $LiMn_2O_4$ (84.6 mAh g^{-1}) cathode. What's more, the results from electrochemical impedance spectroscopy (EIS) revealed that the intercalation/de-intercalation of Li ions in the $LiMn_2O_4$/MWNTs cathode is much faster than that in the $LiMn_2O_4$ cathode. Tang *et al.* prepared $LiMn_2O_4$/CNT composite with a hydrothermal method. After calcinated at 700 °C for 8 h, the $LiMn_2O_4$/CNT electrode exhibited a high specific capacity (136 mAh g^{-1} at the current density of 500 mA g^{-1}) in 5 mol L^{-1} $LiNO_3$ **[97]**.

Besides, Dillon's group developed an aqueous paper battery, using $LiMn_2O_4$ as cathode, carbon coated TiP_2O_7 as anode, and carbon nanotube coated paper as current collector in 5 mol L^{-1} $LiNO_3$ solution **[98]**. Coated by SWNTs not only reduced the resistance of the paper, but also facilitated the penetration of anode and cathode materials into the conductive substrates, resulting in an improved rate capability, in comparison with the organic system.

2.3.3 Using Graphene as Conductive Additive to Increase the Electrical Conductivity of $LiMn_2O_4$ Cathode

2.3.3.1 Structure and Properties

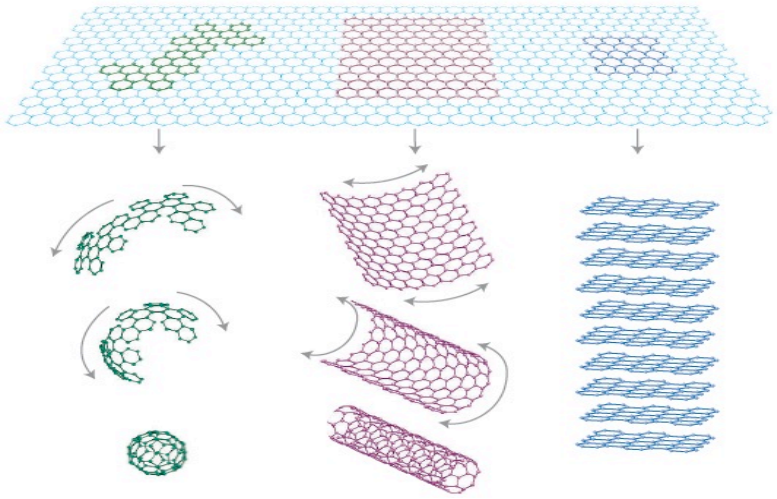

Fig. 2.10 Graphene is the fundamental structural units for other carbonaceous materials (0-D fullerenes, 1-D CNTs, and 3-D graphite).

Since being discovered by professor Geim in 2004, graphene has caused widespread concerns of scientists. Graphene is a two-dimensional (2-D) monolayer graphite sheet that consists of sp^2 carbon atoms arranged in a hexagonal crystal lattice, with a large specific surface area up to 2630 $m^2\ g^{-1}$ **[99, 100]**. It is considered as the fundamental structural units for other dimensional carbonaceous materials, such as zero-dimensional (0-D) fullerenes, 1-D CNTs, and three-dimensional (3-D) graphite, as shown in **Fig. 2.10**.

Graphene possesses unique mechanical and thermal properties. Graphene is the strongest material ever tested, with an intrinsic tensile strength up to 130 GPa **[101]**; the thermal conductivity of graphene is up to 5300 W $(m \cdot K)^{-1}$, which is three times higher than that of the

diamond **[102]**. What's more, the highly special electrical properties of graphene attract much more attentions of researchers: the giant intrinsic mobility of which is up to 15000 $cm^2 (V \cdot s)^{-1}$ **[103]**; the velocity of electrons in which is three hundredth of the speed of light, exceeding most of conductors **[104]**; anomalous quantum Hall effect exists in graphene at room temperature **[105]**. All of these electrical properties contribute to the best conductivity of graphene in room temperature. Graphene is expected to have a wide range of applications, such as energy storage, nanotechnology, electronic devices, biomedical materials, and so forth **[99, 106, 107]**.

2.3.3.2 Synthesis of Graphene

Currently, there are usually six different methods to prepare graphene: mechanical exfoliation **[108, 109]**, graphene oxide (GO) reduction **[110]**, CVD **[111, 112]**, epitaxial growth **[113]**, cutting carbon nanotubes **[114]**, direct sonication, and chemical reduction **[115]**. While among these methods, only GO reduction method and CVD method are suitable for large-scale graphene production. In this part, mechanical exfoliation, GO reduction, and CVD methods are introduced.

Mechanical exfoliation

Since 2004, Professor Geim and Professor Novoselov at University of Manchester first prepared graphene sheets by mechanical exfoliation of graphite **[116]**. The graphite crystals were split into thinner flakes with Scotch tape; then the flakes were dissolved in acetone with the tape, followed by a few further treatment, the flakes with monolayer were deposited on a Si base. Under an optical microscope, individual atomic planes were detected. Furthermore, they obtained large crystallites (larger than 1 mm) by a dry deposition, which can avoid soaking graphene sheets in liquid **[117]**.

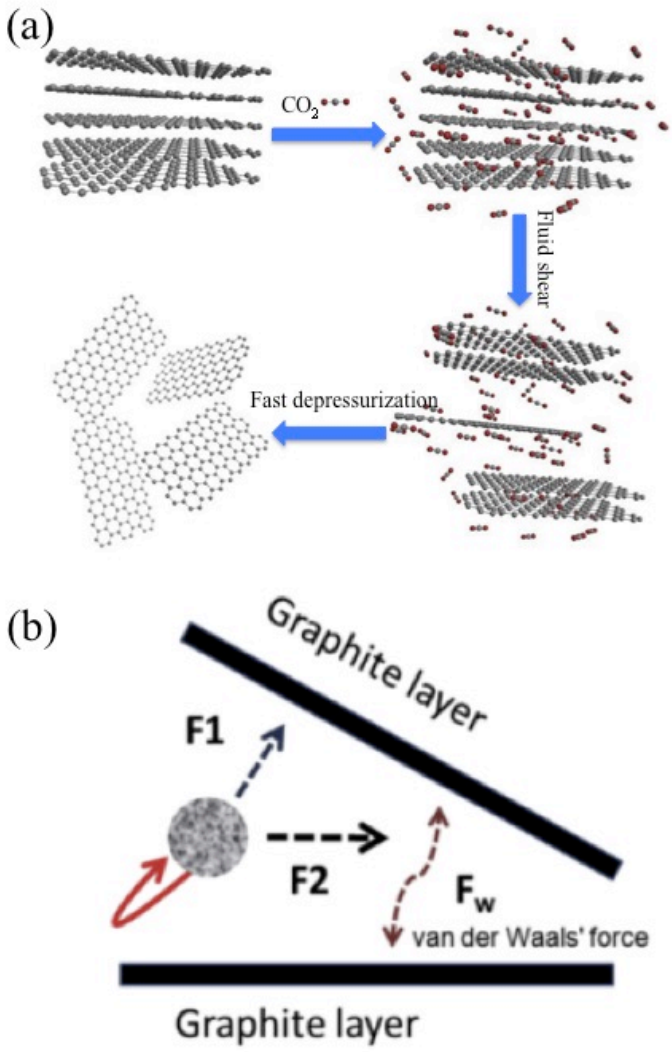

Fig. 2.11 (a) The exfoliation mechanism of graphite into graphene sheets under high-speed fluid shear with supercritical CO_2; (b) The delamination of graphite by a lateral force overcoming the resistance of van der Waals force. (Reprinted from **Ref. [109]**)

Recently, Li *et al.* prepared graphene nanosheets by a shear-assisted supercritical CO_2 exfoliation process **[109]**. The mechanism of this process is shown in **Fig. 2.11a**. CO_2 molecules invade into the interlayers of graphite under high-speed fluid shear stress. A lateral force is

generated due to the violent stirring, which can break the van der Waals force between graphite layers, resulting into the exfoliated graphene (**Fig. 2.11b**) with about 10 layers in thickness.

GO reduction method

Graphite consists of stacked graphene sheets, is cheap and abundant in nature. Preparation of graphene sheets from graphite is likely to be the least expensive route. Mechanical exfoliation of graphite into graphene sheets by tape is only suitable in lab experiments, making it impossible for large-scale preparation; besides, the graphene prepared by a high-speed fluid shear process has a high thickness of about 10 layers, which is very difficult to disperse **[109]**. Chemical conversion from graphite seems to be a promising method to produce graphene in large quantity at low cost **[118]**.

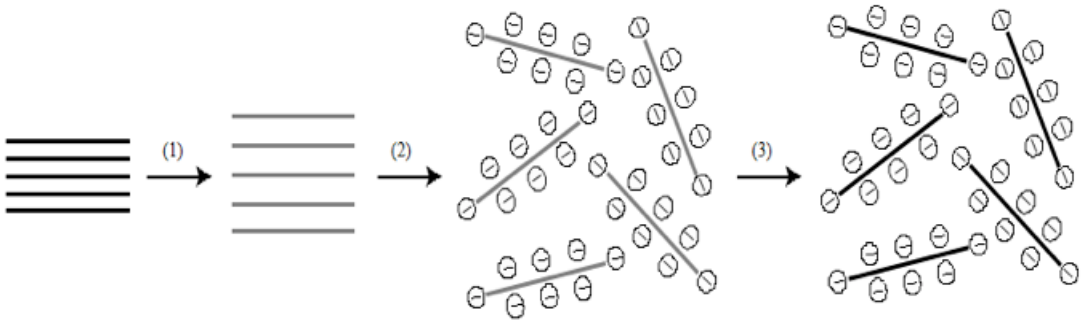

Fig. 2.12 Schematic illustration of the synthesis of reduced graphene oxide dispersions. (1) Graphite (black blocks) is oxidized to graphite oxide (lighter coloured blocks) with greater interlayer distance by a modified Hummers' method; (2) Graphite oxide is dispersed in water with an ultra-sonication agitation to form GO colloids; (3) GO colloids are reduced to reduced graphene oxide (RGO) by hydrazine. (Reprinted from **Ref. [119]**)

Li *et al.* **[120]** demonstrated the preparation of graphene through a GO reduction method, which includes three steps as following (**Fig. 2.12**): (1) oxidize graphite to hydrophilic GO with greater interlayer distance by modified Hummers' method; (2) disperse GO in water with ultra-sonication to form GO colloids that are stabilized by electrostatic repulsion; (3) convert the insulated GO back to conducting graphene by chemical reduction, for example, using hydrazine. The graphene prepared by the GO reduction method is named as reduced graphene oxide (RGO). The graphene oxide reduction method has inevitable disadvantages: the structure of graphene is destroyed by strong oxidant and reductant used in the preparation process, resulting in the loss of the electrochemical performance of RGO; besides, graphene oxide is easily accumulated in aqueous solution due to the van der Waals force. However, this method costs low and is suitable to prepare graphene derivatives, which expands the application of graphene.

Chemical Vapor deposition method

The CVD method provides a promising way to realize the controllable preparation of graphene **[112]**. Graphene with different properties can be obtained by selecting different substrates and carbonaceous sources, as well as controlling reaction temperature in the preparation process. In a typical CVD process, the substrate (include nonmetal substrates like MgO, NiO, *etc.*; metal substrates like Ni, Co, *etc.*) is exposed to one or more volatile precursors (usually carbon sources such as methane, ethylene, acetylene, *etc.*), which cracked at high temperature to form desired deposit on the surface of the substrate. Generally, volatile by-products produced in the CVD process flow out through the reactor. After the substrate is removed, the desired product is obtained.

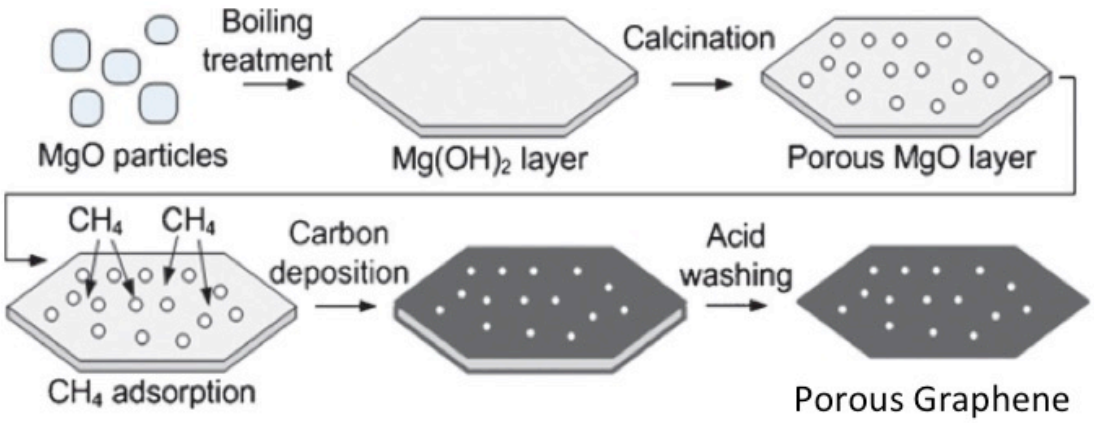

Fig. 2.13 Illustration of the formation of the porous graphene. (Modified from **Ref. [112]**)

Ning *et al.* prepared a kind of porous graphene (PG) with porous corrugated structure by a CVD method, using porous MgO as the template **[112, 121]**. The preparation of porous MgO layers and the template growth of PG are shown in **Fig. 2.13**. Lamella-like porous MgO layers were prepared by a boiling treatment. Firstly, the as-purchased MgO powder was mixed with deionized water under ultrasonic agitation. The mixture was boiled for 24 h in a reflux apparatus. After filtration, drying, and calcination at 500 °C for 30 min, porous MgO layers were obtained. Then, PG was prepared by a one-step CVD process, in which CH_4 was cracked at 875 °C with carbon deposited on MgO templates, followed by an acid washing to remove MgO and drying at 80 °C overnight in an oven, PG was obtained.

2.3.3.3 $LiMn_2O_4$/graphene Nanocomposites

Except for CNTs, graphene, a 2-D single layer of carbon atoms, possesses unique properties such as high surface area and superior electrical conductivity **[122]**. The high surface area can increase the interfacial contact between electrode and electrolyte, resulting in a fast transportation of Li ions; the superior electrical conductivity contributes to a fast electron

transport. Therefore, graphene is also attractive as an ideal template to construct a hybrid material with good dispersion of $LiMn_2O_4$ nanoparticles and improved electrical conductivity **[89, 123, 124]**. Recently, $LiMn_2O_4$/graphene **[125, 126]** and $LiMn_2O_4$/RGO **[127, 128]** composites have been prepared and studied as the cathodes of lithium ion batteries, the electrochemical performance especially the rate capability of $LiMn_2O_4$ was improved by graphene modified.

Besides, there are a few reports about using graphene in aqueous rechargeable battery to improve the electrical conductivity of $LiMn_2O_4$ **[125, 129-131]**. Jiang *et al.* used graphene nanosheets as a powerful conductive additive in the $LiMn_2O_4$ electrode directly. The electrochemical measurements were conducted in 5 mol L^{-1} $LiNO_3$ aqueous electrolyte. When graphene nanosheets and acetylene black nanoparticles co-existed with an appropriate weight ratio in the electrode, the rate performance of the $LiMn_2O_4$ electrode was highly enhanced. The high rate capability is attributed to the effective conducting network formed by graphene nanosheets and acetylene black nanoparticles **[125]**.

Chapter 3

Using Carbon Nanotube as New Conductive Additive to Enhance the Rate Performance of $LiMn_2O_4$ Cathode in ReHAB

3.1 Introduction

The low electrical conductivity of $LiMn_2O_4$ limits its rate performance **[1]**. One of the approaches is adding conductive additives to enhance the electrical conductivity of $LiMn_2O_4$ cathode **[2]**. Traditionally, electrodes are fabricated from mixtures of active materials, conductive additive (*e.g.*, acetylene black (AB)), and polymeric binders. However, nano-sized AB can't provide long-range conductivity. Carbon nanotubes (CNTs) are well known as an ideal material to improve the electrical conductivity of battery electrodes; they can provide long-range conductivity, better interfacial contacts between active materials and conducting pathways, and create more stable network structures **[3]**. Therefore, in this chapter, in order to improve the rate performance of the $LiMn_2O_4$ cathode of the ReHAB, a three-dimensional hierarchically structured CNT/AB network was fabricated to increase the conductive contacts among $LiMn_2O_4$ nanoparticles and conductive pathways, using a mechanical mixing method. The hierarchical CNT/AB/$LiMn_2O_4$ electrode was then studied as the cathode of the ReHAB.

3.2 Experimental

3.2.1 Material Preparation

Catalyst preparation **[4]**: Vermiculite (mined in Lingshou, Hebei province of China), a clay mineral, which composes of 42 wt% SiO_2, 12 wt% Al_2O_3, 28 wt% MgO, 13 wt% Fe_2O_3, 4 wt% K_2O, 0.5 wt% CaO, and 0.5 wt% H_2O, was used as substrate of the catalyst. Firstly, vermiculite

powder (size of 100-250 μm, bulk density of ~160 kg m^{-3}) was mixed with deionized to form a uniform suspension under vigorous stirring at 80 °C; then, a solution of $Fe(NO_3)_3 \cdot 9H_2O$ (Sigma-Aldrich, ≥ 99.95% purity) and $(NH_4)_6Mo_7O_{24} \cdot 4H_2O$ (Sigma-Aldrich, ≥ 99.98% purity) was added into the suspension quickly, keeping at 80 °C for 12 h. The weight ratio of vermiculite : Fe : Mo was 90 : 5 : 5. Followed by filtration, drying (110 °C for 12 h), and calcination (400 °C for 4 h), the lamellar Fe/Mo/vermiculite catalyst was obtained.

Synthesis of CNTs **[6, 7]**: Multi-walled CNTs were produced from a chemical vapor deposition (CVD) method. In a typical CVD run, 5 g Fe/Mo/vermiculite catalyst was loaded into a vertical-set quartz tube furnace (50 mm in diameter and 1500 mm in length) with a sintered porous plate as the gas distributor (**Fig. 3.1a**). The reactor was then heated to 650 °C under an Ar flow (1000 mL min^{-1}). After reduction under a flow of Ar and H_2 (10 : 1, v/v) at 1100 mL min^{-1} for 15 min, a mixture of C_2H_4 (600 mL min^{-1}), Ar (400 mL min^{-1}), and H_2 (50 mL min^{-1}) was introduced for 15 min to allow CNT growth. When the reactor cooled to the room temperature, the as-prepared material (vermiculite-CNT composite) was taken out, followed by a purification process with acid, using 18% HCl solution (Sigma-Aldrich, ≥ 99% purity) and 20% HF solution (Sigma-Aldrich, ≥ 99% purity) with reflux for 1 h, to remove the catalysts. Then, they were washed using deionized water and dried at 80 °C overnight before use.

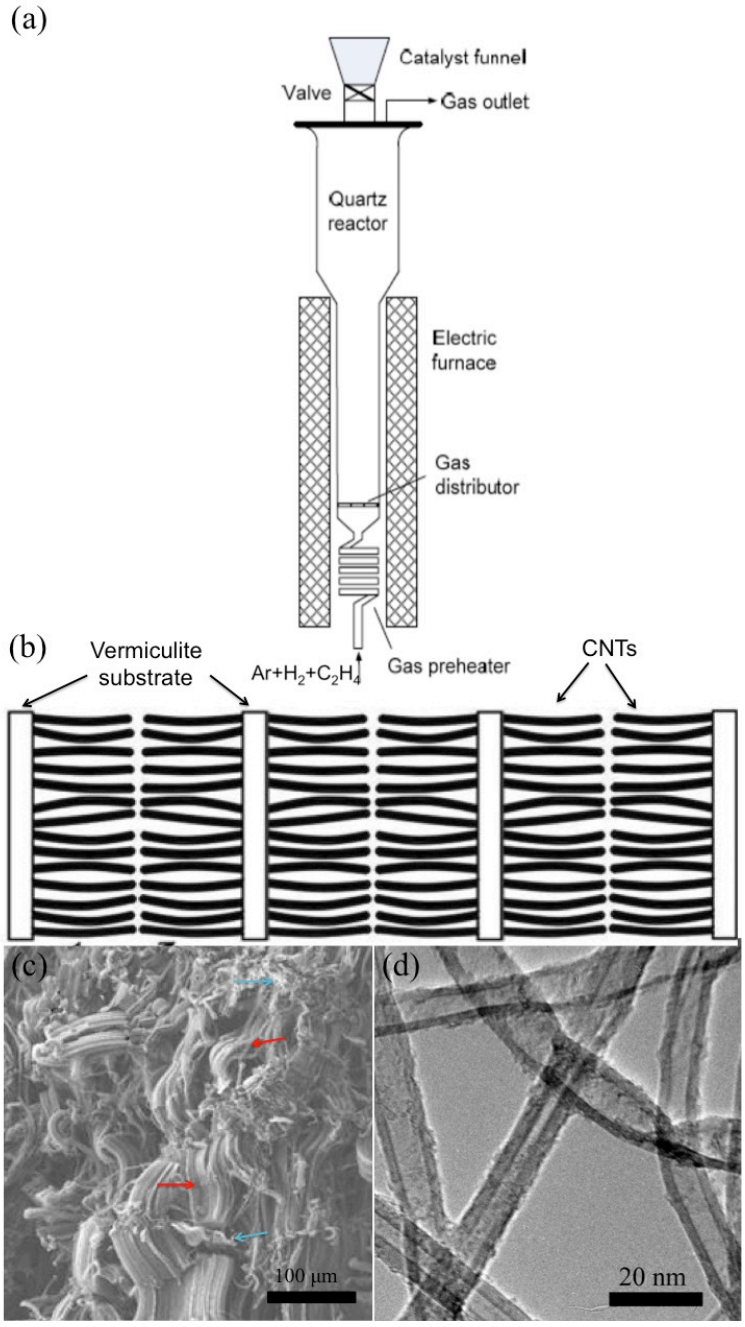

Fig. 3.1 (a) Schematic of the downer reactor for the synthesis of CNTs, (Modified from **Ref. [5]**); (b) Schematic illustration of a vermiculite-CNT composite, (Modified from **Ref. [4]**); (c) SEM image of a vermiculite-CNT composite, the blue arrows point to vermiculite substrates and the red arrows point to CNTs; (d) TEM image of the CNTs after purification.

During the CVD process, the catalysts on the vermiculite substrates catalyze the growth of CNTs, forming a vermiculite-CNT composite, which is illustrated in **Fig. 3.1b**. The morphology of the vermiculite-CNT composite is shown in **Fig. 3.1c**. From the SEM image of the vermiculite-CNT composite, we can clearly find that the length of the as-prepared CNTs is up to 100 micrometers; besides, the diameter of the CNTs is about 11 nm, which can be confirmed by TEM image in **Fig. 3.1d**.

3.2.2 Physical Characterization

The crystal structure of the cathodes was characterized using X-ray diffraction techniques (XRD, Advance D8, Bruker) with Cu-Kα radiation. For XRD analysis, the electrode sheets were stuck on the sample plate and then fixed on the objective table in the XRD equipment for analysis in the range of 5 to 90° (2θ) under 4° min^{-1}.

The morphology of the as-prepared sample (vermiculite-CNT composite) and cathodes were observed by scanning electron microscopy (SEM, JEOL JSM-6700, JEOL). Energy dispersive X-ray spectroscopy (EDS) analysis was performed on the LEO FESEM 1530 instrument using an equipped EDAX apparatus. For SEM analysis, a small amount of the powder of the sample (for the cathodes, a small piece of electrode sheet) was stuck on the conductive tape before observation. The same process was conducted for EDS analysis. The internal morphology of the as-prepared sample (CNTs) and cathodes was studied using transmission electron microscopy (TEM, FEI T12, FEI) operated at 120 kV. For TEM analysis, a tiny amount of the powder of the samples (for cathodes, a tiny piece of electrode sheet that removed the current collector) was dispersed in ethanol under ultra-sonication agitation for less than 10 seconds (inhibit CNTs from

breaking into short length), and then 0.5 mL of this solution was dropped onto a Cu grid coated by a lacey carbon; followed by drying at 80 °C for 20 min before observation.

3.2.3 Battery Assembly and Electrochemical Characterization

The composite cathodes were prepared by casting a slurry of 83 wt% $LiMn_2O_4$ (MTI Co. Ltd, ~ 0.2 μm), 10 wt% carbon conductor consisting of CNTs and acetylene black (AB, MTI) with different weight ratios (CNTs : AB = 1 : 9, 1 : 4, 1 : 2, 1 : 0, and 0 : 1), and 7 wt% polyvinylidene fluoride (PVdF, Kynar, HSV900) in 1-methyl-2-pyrrolidinone (NMP, Sigma-Aldrich, ≥ 99.5% purity) on graphite foil (Alfa Aesar), and vacuum drying at 60 °C for 24 h. The electrodes prepared are indicated as the 1wt%CNT/AB/$LiMn_2O_4$, 2wt%CNT/AB/$LiMn_2O_4$, 3.3wt%CNT/AB/$LiMn_2O_4$, 10wt%CNT/$LiMn_2O_4$, and 10wt%AB/$LiMn_2O_4$ electrodes, corresponding to different weight ratios of CNTs to AB as 1 : 9, 1 : 4, 1 : 2, 1 : 0, and 0 : 1. It is important to mention that the CNTs should be dispersed in NMP first before mixing with $LiMn_2O_4$ and AB particles to make the slurry. Disks of 12 mm in diameter were cut and soaked in the electrolyte under reduced pressure before battery assembly. Twelve millimeters in diameter polished zinc disks (Rotometals, thickness: 0.2 mm) were used as the anode. The solution of 2 mol L^{-1} Li_2SO_4 (Sigma-Aldrich, ≥ 99% purity) and 1 mol L^{-1} $ZnSO_4$ (Alfa Aesar, ≥ 98% purity) in deionized water was used as electrolyte. pH was adjusted to 4 by titration with 0.1 mol L^{-1} LiOH. Absorbed glass mat (AGM, NSG Corporation) was used as separator.

Cyclic voltammetry (CV) measurement was carried out on a Biologic-VMP3 electrochemical workstation at a scan rate of 0.1 mV s^{-1}. Electrochemical impedance spectroscopy (EIS) of the batteries was conducted at the DC potential of 10 mV, with the frequency range from 0.01 Hz to

100 KHz. Two-electrode Swagelok cells were used for galvanostatic charge/discharge cycling at room temperature, using a Neware battery tester at various C-rates, 1-20 C, calculated based on the nominal specific capacity of $LiMn_2O_4$ (1 C=120 mA g^{-1}), between 1.4 and 2.1 V.

3.3 Results and Discussion

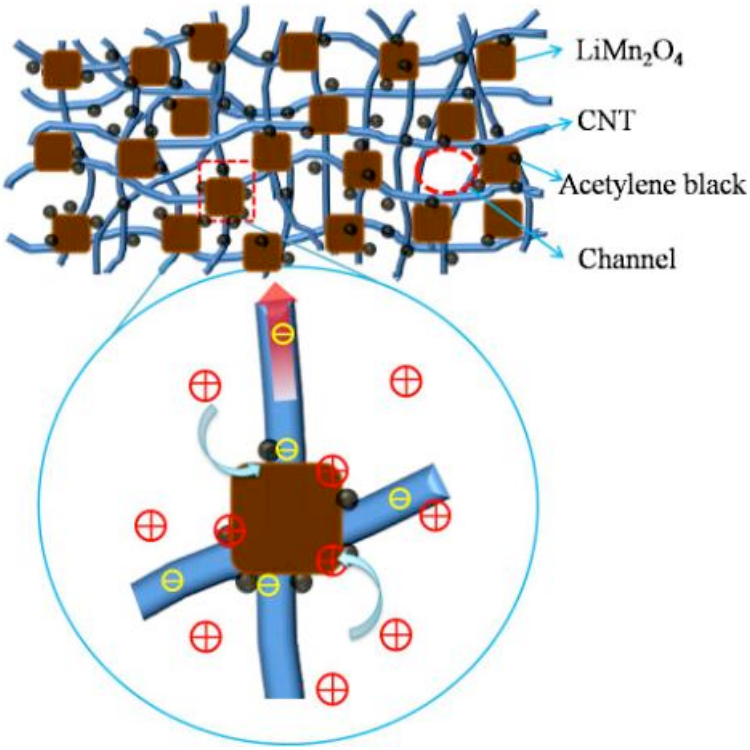

Fig. 3.2 Schematic illustration for preparing hierarchical CNT/AB/$LiMn_2O_4$ electrodes.

Figure 3.2 shows the schematic structure of hierarchical CNT/AB/$LiMn_2O_4$ electrodes. The small black dots represent AB nanoparticles, the brown squares represent $LiMn_2O_4$ nanoparticles, and the blue lines represent CNTs. The resulting CNT/AB network can provide: (i) hierarchical and long-range conductive pathways for fast electron transfer in the cathode, (ii) interconnected network structure within the electrode for better active material utilization, and (iii) a stable composite structure that enables a longer charge/discharge cycle life. Based on the

design and structure features, the resulting CNT/AB/$LiMn_2O_4$ electrodes exhibit excellent rate capability and cyclability in comparison with the cathodes prepared previously.

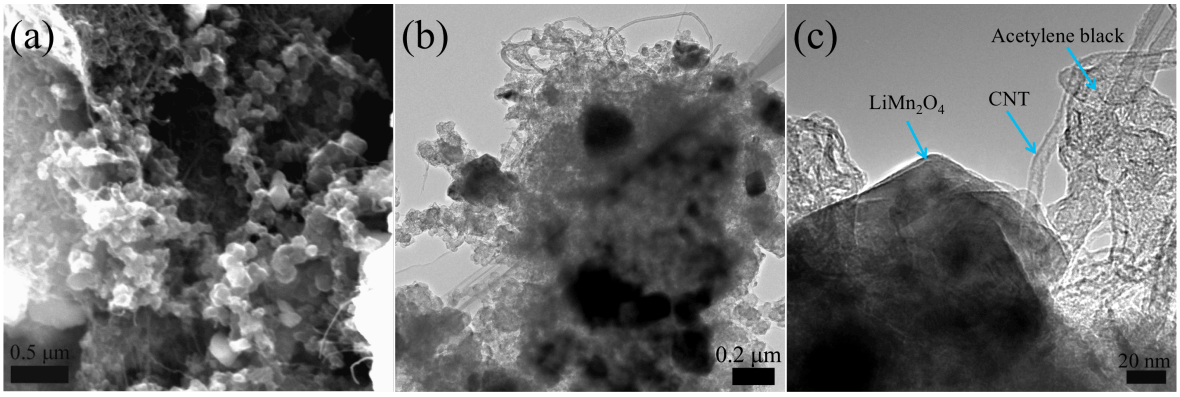

Fig. 3.3 (a) SEM and (b,c) TEM images of the 3.3wt%CNT/AB/$LiMn_2O_4$ electrode.

Figure 3.3a presents the representative SEM image of the pristine 3.3wt%CNT/AB/$LiMn_2O_4$ electrode, in which $LiMn_2O_4$ nanoparticles are uniformly dispersed in the carbon matrix. The CNTs can be clearly identified. The elemental mapping of the 3.3wt%CNT/AB/$LiMn_2O_4$ electrode was obtained by energy-dispersive X-ray spectroscopy (EDS, **Fig. 3.4**), which further confirms the uniform distribution of $LiMn_2O_4$ nanoparticles within the CNT/AB networks. TEM image at a low magnification also presents the three-dimensional hierarchical network composed by CNTs and AB nanoparticles (**Fig. 3.3b**). TEM observation at higher magnification (**Fig. 3.3c**) further confirms that CNTs interweave between AB and $LiMnO_4$ nanoparticles, increasing the interfacial contacts and thus electrical conductivity.

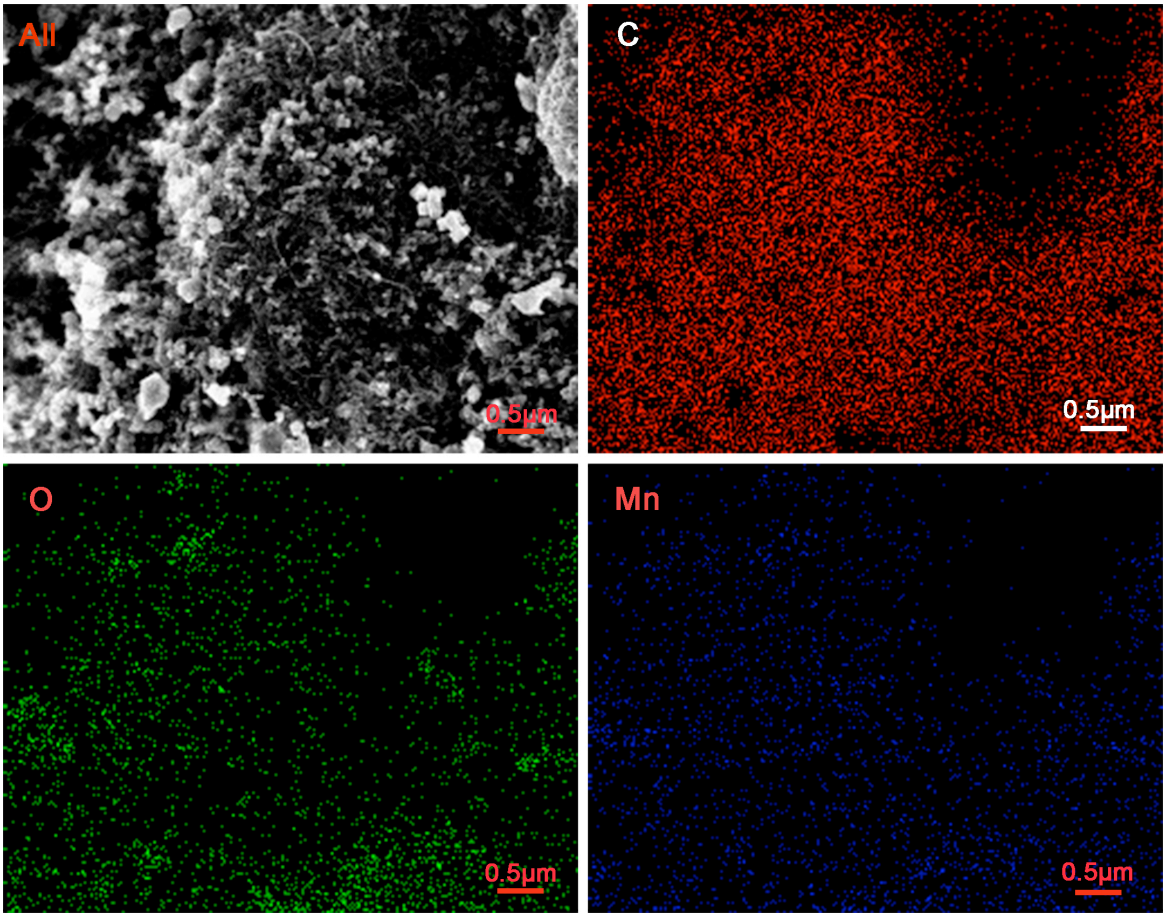

Fig. 3.4 SEM image and the corresponding EDS elemental maps of C, O, Mn of the 3.3wt%CNT/AB/$LiMn_2O_4$ electrode.

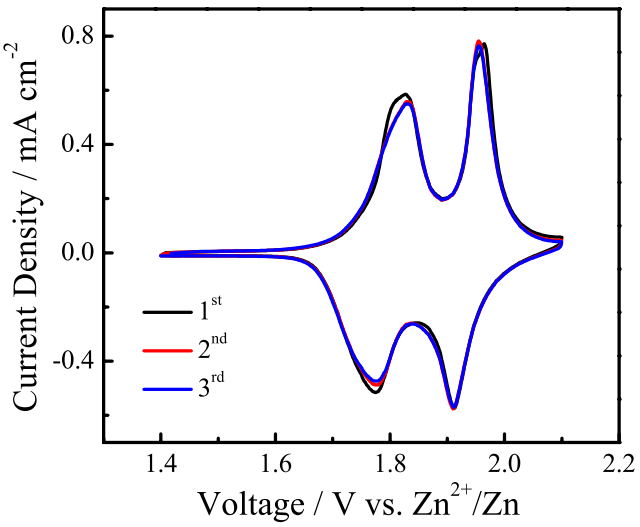

Fig. 3.5 CV curves of the 3.3wt%CNT/AB/$LiMn_2O_4$ electrode at 0.1 mV s^{-1}.

The three-dimensional hierarchical CNT/AB networks ensure the 3.3wt%CNT/AB/$LiMn_2O_4$ electrode with excellent lithium storage performance, which was examined by various electrochemical characterizations. Cyclic voltammetry (CV) studies were first conducted to investigate their lithium storage behaviors at a scan rate of 0.1 mV s^{-1} (**Fig. 3.5**). There are two redox couples located at 1.82/1.78 V and 1.96/1.92 V vs. Zn^{2+}/Zn, respectively. They are corresponding to the two stages of extraction and insertion of Li ions from/into the host spinel structure of $LiMn_2O_4$ in the aqueous electrolyte, which could be described as $LiMn_2O_4 \rightleftharpoons Li_{0.5}Mn_2O_4 + 0.5Li^+ + 0.5e^-$ and $Li_{0.5}Mn_2O_4 \rightleftharpoons 2MnO_2 + 0.5\ Li^+ + 0.5\ e^-$, respectively **[8]**. The potential differences between oxidation peaks and reduction peaks are contributed to the polarization of the electrode during CV testing. The potential difference between oxidation peaks and reduction peaks is as small as 0.04 V, resulting partially from the high ionic conductivity of the aqueous electrolyte. The symmetrical peaks reveal that the Li ion extraction/insertion process

can be regarded as highly reversible. In addition, the peaks retain the well-defined shapes and almost the same redox potential over the cycles of the scanning process, demonstrating the stability of the 3.3wt%CNT/AB/$LiMn_2O_4$ electrode.

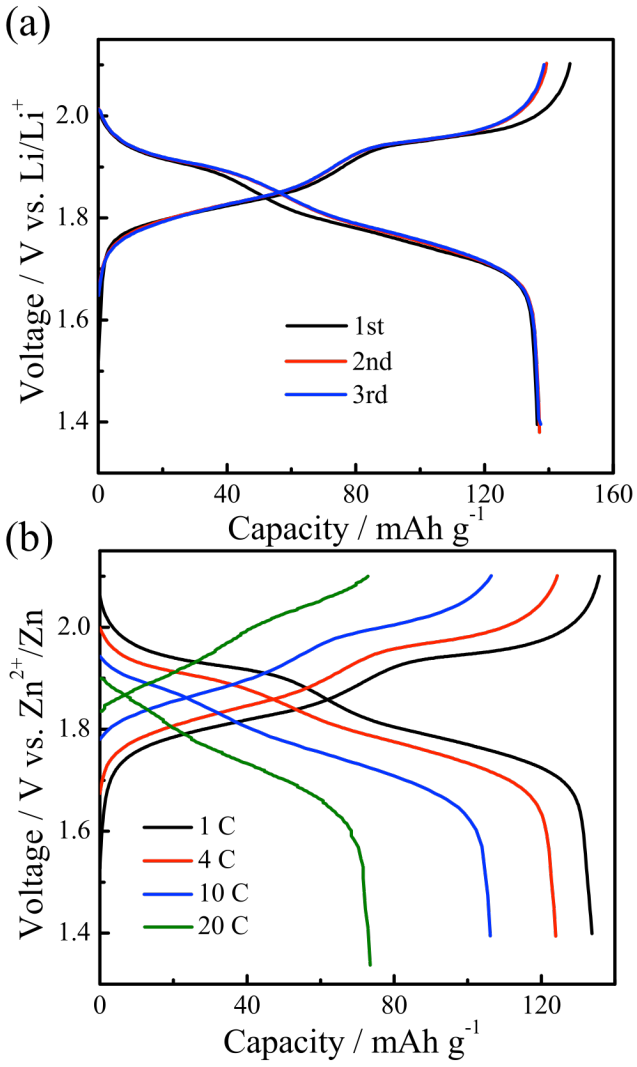

Fig. 3.6 (a) Galvanostatic charge/discharge profiles of the 3.3wt%CNT/AB/$LiMn_2O_4$ electrode at 4 C; (b) Galvanostatic charge/discharge profiles of the 3.3wt%CNT/AB/$LiMn_2O_4$ electrode at different rates (1 C, 4 C, 10 C, and 20 C).

To further quantify the lithium storage capability, galvanostatic charge/discharge was conducted. **Fig. 3.6a** shows the galvanostatic charge/discharge profiles of the 3.3wt%CNT/AB/$LiMn_2O_4$ electrode at 4 C. The charge/discharge curves present two distinguished plateaus, which reflect two-stage Li ion extraction/insertion behavior and are consistent with the obtained CV data. Initial specific charge and discharge capacities of the composite cathode are 146 and 139 mAh g^{-1}, respectively, corresponding to a Coulombic efficiency of 95.2%, which is much higher than that in the organic electrolyte **[6, 9, 10]**. In the following cycles, the Coulombic efficiency is close to 100% and remains stable, indicating good reversibility. It should be noted that the excellent specific discharge capacity of 139 mAh g^{-1} has never been reported for $LiMn_2O_4$ cathodes in other aqueous battery systems **[11-13]**, which may be due to a hierarchical and long-range conductive pathway built by high aspect ratio CNTs and AB nanoparticles, as well as a interconnected network structure within the electrode. Moreover, the charge/discharge curves at different current densities were also performed to evaluate the charge storage behaviors (**Fig. 3.6b**). It shows that the charge/discharge processes of the 3.3wt%CNT/AB/$LiMn_2O_4$ electrode are highly reversible, suggesting the excellent reaction kinetics and further confirming the stability of the CNT/AB network.

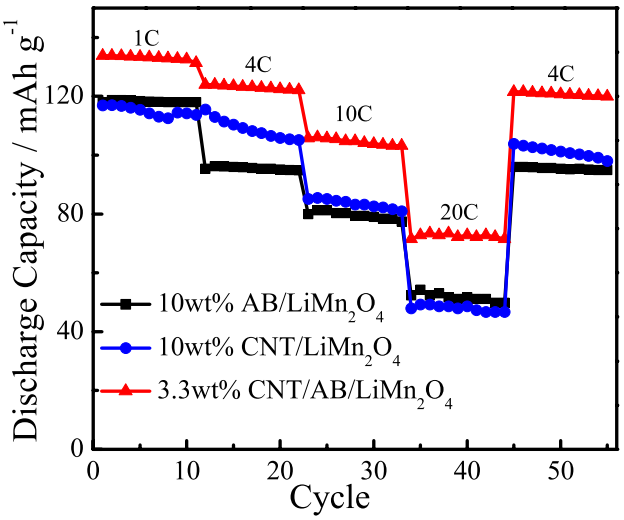

Fig. 3.7 Rate capability of the 3.3wt%CNT/AB/$LiMn_2O_4$, 10wt%CNT/$LiMn_2O_4$, and 10wt%AB/$LiMn_2O_4$ electrodes.

The rate capability of the 3.3wt%CNT/AB/$LiMn_2O_4$, 10wt%CNT/$LiMn_2O_4$, and 10wt%AB/$LiMn_2O_4$ electrodes were studied and compared (**Fig. 3.7**). The specific discharge capacity of the 3.3wt%CNT/AB/$LiMn_2O_4$ electrode is significantly larger than that of the 10wt%AB/$LiMn_2O_4$ and 10wt%CNT/$LiMn_2O_4$ electrodes at C-rates from 1 to 20 C. At 10 C, the 3.3wt%CNT/AB/$LiMn_2O_4$ electrode exhibits an extremely high specific discharge capacity of 105 mAh g^{-1}, corresponding to ~79% of that at 1 C. What's more, the 3.3wt%CNT/AB/$LiMn_2O_4$ electrode still exhibits 73 mAh g^{-1} at 20 C. Carbon nanotubes help to connect AB and $LiMn_2O_4$ nanoparticles, and improve the electrical conductivity of the cathode significantly, thereby enhancing the rate capability.

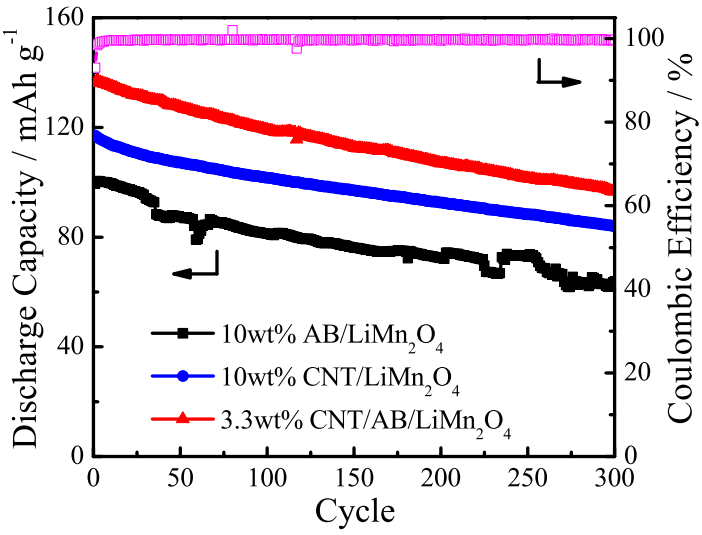

Fig. 3.8 Cyclability of the 3.3wt%CNT/AB/$LiMn_2O_4$, 10wt%CNT/$LiMn_2O_4$, and 10wt%AB/$LiMn_2O_4$ electrodes at 4 C.

Except for the excellent rate capability, the 3.3wt%CNT/AB/$LiMn_2O_4$ electrode also exhibits a good cycling performance at 4 C as shown in **Fig. 3.8**. After 300 cycles, the specific discharge capacity of 92 mAh g^{-1} is still obtained. Moreover, the Coulombic efficiency is close to 100%.

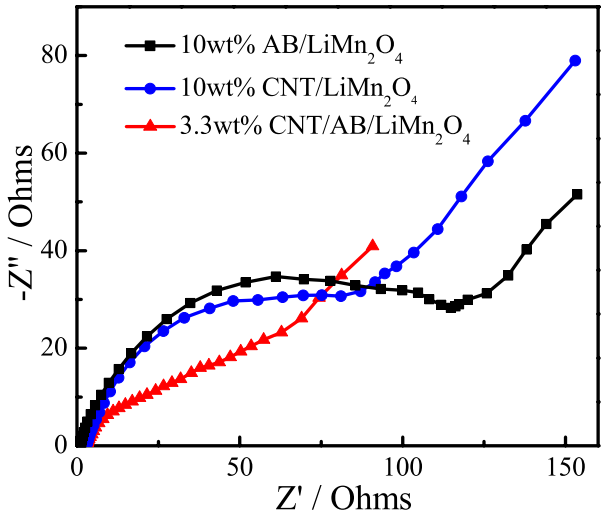

Fig. 3.9 EIS spectra of the batteries made of the 3.3wt%CNT/AB/$LiMn_2O_4$, 10wt%CNT/$LiMn_2O_4$, and 10wt%AB/$LiMn_2O_4$ electrodes after 300 charge/discharge cycles at 4 C.

Electrochemical impedance spectroscopy plots of the batteries made of the 3.3wt%CNT/AB/$LiMn_2O_4$, 10wt%CNT/$LiMn_2O_4$, and 10wt%AB/$LiMn_2O_4$ electrodes after 300 charge/discharge cycles at 4 C are shown in **Fig. 3.9**. Each plot consists of a depressed semicircle at the high-to-medium frequency region, corresponding to the charge transfer resistance and the double-layer capacitance; and an inclined line in the low frequency region, corresponding to the Li ion diffusion within $LiMn_2O_4$ nanoparticles **[14]**. The semicircle of the 3.3wt%CNT/AB/$LiMn_2O_4$ electrode is smaller than those of the 10wt%CNT/$LiMn_2O_4$ and 10wt%AB/$LiMn_2O_4$ electrodes, indicating a smaller charge transfer resistance. This smaller charge transfer resistance is consistent with the higher rate capability of the 3.3wt%CNT/AB/$LiMn_2O_4$ electrode.

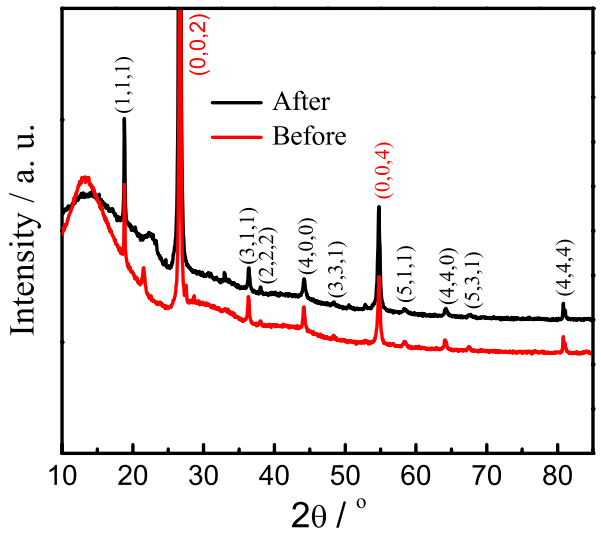

Fig. 3.10 XRD patterns of the 3.3wt%CNT/AB/$LiMn_2O_4$ electrode before and after 300 charge/discharge cycles at 4 C.

In order to verify the structure stability of the $LiMn_2O_4$, XRD patterns of the 3.3wt%CNT/AB/$LiMn_2O_4$ electrode before and after 300 charge/discharge cycles are shown in **Fig. 3.10**. All major peaks are indexed and fit well with the standard pattern **[6]**. Peak locations have not changed significantly before and after cycling, indicating the high stability of the $LiMn_2O_4$ during charge/discharge cycling. It is evident that the components of CNTs and AB in the electrodes are important for better battery performance. The three-dimensional, hierarchical structure of the CNT/AB networks is beneficial to obtain the good electrical conductivity and stability of the cathode. It is also important to note that the material preparation here is very simple and effective, making the approach commercially feasible in comparison with other sophisticated and complicated approaches.

The results above reveal that adding a certain amount of CNTs into the cathode can highly improve the power/energy density of the ReHAB. However, in order to make the CNT/AB/$LiMn_2O_4$ electrodes more competitive in comparison with traditional AB/$LiMn_2O_4$ electrodes, reducing the content of CNTs to reduce the cost is crucial. The price of Multi-walled CNTs (MWNTs) is about three times higher than that of AB with a high quality. The rate and cycling performances of the CNT/AB/$LiMn_2O_4$ electrodes with different content of CNTs are compared (**Fig. 3.11**). When the content of CNTs reduces to 2 wt%, the 2wt%CNT/AB/$LiMn_2O_4$ electrode still exhibits at least 23% higher rate capability than the 10wt%AB/$LiMn_2O_4$ electrode (**Fig. 3.11a**), and also keeps a high capacity retention of 72.8% after 300 cycles at 4 C (**Fig. 3.11b**).

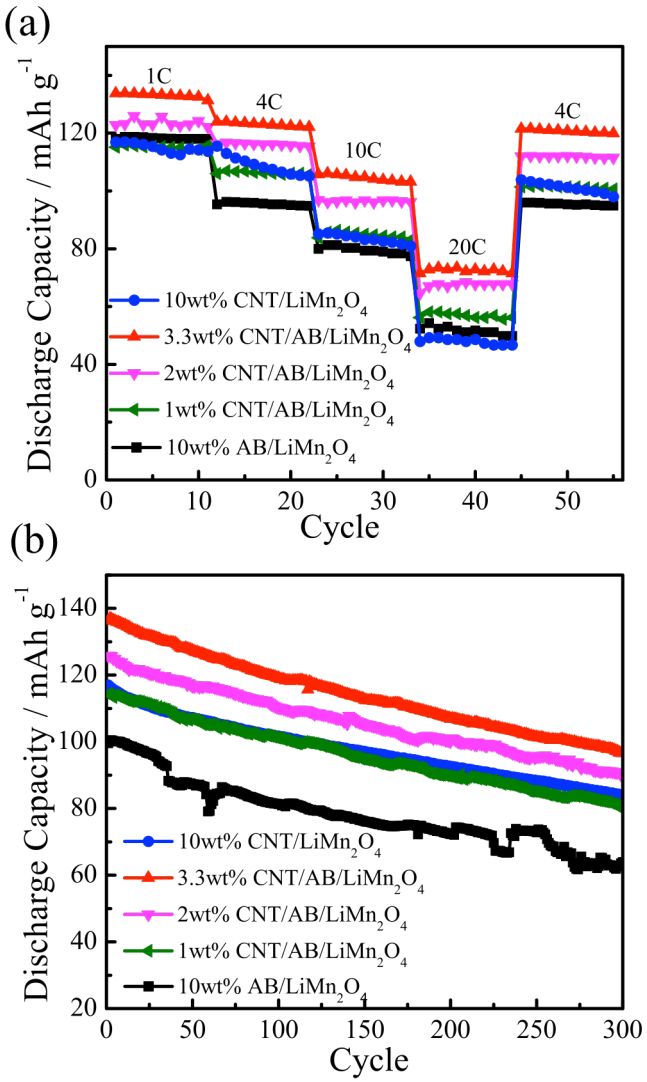

Fig. 3.11 (a) Rate capability of the CNT/AB/$LiMn_2O_4$ electrodes with different content of CNTs; (b) Cyclability of the CNT/AB/$LiMn_2O_4$ electrodes with different content of CNTs at 4 C.

3.4 Summary

A three-dimensional, hierarchical CNT/AB network was fabricated by a simple mixing approach to improve the rate and its related performance of the $LiMn_2O_4$ cathode in the ReHAB. Thanks to the hierarchical and long-range conductive pathways for fast electron transfer and the

stable composite structure, the 3.3wt%CNT/AB/$LiMn_2O_4$ electrode exhibits outstanding rate performance (specific discharge capacity of 105 mAh g^{-1} and 73 mAh g^{-1} at 10 C and 20 C, respectively), along with good cycling performance and reversibility (Coulombic efficiency of almost 100% over 300 charge/discharge cycles at 4 C). What's more, when the content of CNTs reduces to 2 wt%, the 2wt%CNT/AB/$LiMn_2O_4$ electrode still exhibits at least 23% higher rate capability than the traditional 10wt%AB/$LiMn_2O_4$ electrode. This approach is simple and highly effective to enhance the rate capability of the $LiMn_2O_4$ cathode. This hierarchical conductive network design is also useful in other battery applications for high charge/discharge rates.

Chapter 4

The Preparation of Binder-free Flexible $LiMn_2O_4$/CNT Network as High Power Cathode for ReHAB

4.1 Introduction

High-performance energy storage systems rely on effective transport of electrons and ions during their charge/discharge processes, where energy is reversely transformed as chemical energy and electric energy, respectively **[1-3]**. Reliability of such transport pathways is therefore one of the most essential criteria that governs the rate capability of the system. Traditionally, the electron-transport pathways are constructed by mixing active electrode materials with conductive additives and polymeric binders **[4-6]**. However, such approach utilizes a significant amount of inert components, inevitably compromising the device's energy density. Alternatively, binder-free $LiMn_2O_4$/CNT electrodes have been proposed and used in a lithium ion battery. Directed growth of $LiMn_2O_4$ on flexible carbon nanotubes (CNTs) was reported by Jia *et al.* **[7]**, using redox reactions between CNTs and $KMnO_4$ with a subsequent hydrothermal treatment in the presence of LiOH. Due to the highly conductive and porous CNTs support, the cathode showed good rate capability and cyclability.

Herein, in this chapter, a highly robust binder-free flexible $LiMn_2O_4$/CNT electrode composed of CNTs and $LiMn_2O_4$ was constructed by a vacuum filtration process and studied as the cathode of the Rechargeable Hybrid Aqueous Battery (ReHAB) **[8]**. It is worth mentioning that this is the first demonstration of using highly stable binder-free flexible $LiMn_2O_4$/CNT electrodes in an aqueous rechargeable battery.

4.2 Experimental

4.2.1 Material Preparation

Fabrication of binder-free flexible electrodes. A vacuum filtration method was used to fabricate the electrodes with controllable thickness **[7]**. Firstly, Multi-walled CNTs with length of ~100 μm and diameter of ~11 nm were produced and purified by the same process introduced in chapter 3.2.1. The purified CNTs were then dispersed in N-methyl-2-pyrrolidone (NMP, Sigma-Aldrich, ≥ 99.5% purity) using fluid shearing dispersion for 30 min to form 2.0 mg mL^{-1} solution. 10 mL of the CNT dispersion was mixed with 180 mg of the $LiMn_2O_4$ (MTI Co. Ltd) particles; and then filtered and dried under vacuum at 90 °C for 12 h to obtain the binder-free flexible films. The contents of CNT and $LiMn_2O_4$ are 10 and 90 wt%, respectively.

4.2.2 Physical Characterization

The cathode morphology was observed by scanning electron microscopy (SEM, JEOL JSM-6700, JEOL). For SEM analysis, a small piece of electrode sheet was stuck on the conductive tape before observation. The internal morphology was studied using transmission electron microscopy (TEM, FEI T12, FEI) operated at 120 kV. For TEM analysis, a tiny piece of electrode sheet was dispersed in ethanol under ultra-sonication agitation for less than 10 seconds (inhibit CNTs from breaking into short length), and then 0.5 mL of this solution was dropped onto a Cu grid coated by a lacey carbon; followed by drying at 80 °C for 20 min before observation. Nitrogen sorption isotherms were measured at 77 K with a Micromeritics ASAP 2020 analyzer. The electrode film (thickness: 0.2 mm, measured by a FJS025 Digital Spiral-micrometer) was cut into sheets (10 mm × 10 mm) for mechanical tests, which were conducted

on an INSTRON 5564 with a speed of 2.0 mm min^{-1} at room temperature. The resistance of the CNT dispersion and the composite electrode (cut into sheet with the size of 5 mm × 25 mm) under bending were both measured using a 266 Clamp Meter. The volume conductivity of the composite electrode was calculated based on the equation: $\kappa=L/(RA)$, where R is the resistance values that can be obtained from the 266 Clamp Meter, L is 25 mm, A= 0.2 mm × 5 mm.

4.2.3 Battery Assembly and Electrochemical Characterization

For electrochemical test, the flexible $LiMn_2O_4$/CNT films were cut into disks of 12 mm in diameter and soaked in the electrolyte under reduced pressure before assembling of batteries. The traditional electrodes were prepared by casting a slurry of 86 wt% $LiMn_2O_4$ (MTI Co. Ltd, ~0.2 μm), 7 wt% carbon conductor consisting of CNTs or acetylene black (AB, MTI), and 7 wt% polyvinylidene fluoride (PVdF, Kynar, HSV900) in 1-methyl-2-pyrrolidinone (NMP, Sigma-Aldrich, ≥ 99.5% purity) on graphite foil (Alfa Aesar), and vacuum drying at 60 °C for 24 h. Twelve millimeters in diameter polished zinc disks (Rotometals, thickness: 0.2 mm) were used as the anode. The solution of 2 mol L^{-1} Li_2SO_4 (Sigma-Aldrich, ≥ 99% purity) and 1 mol L^{-1} $ZnSO_4$ (Alfa Aesar, ≥ 98% purity) in deionized water was used as electrolyte. pH was adjusted to 4 by titration with 0.1 mol L^{-1} LiOH. Absorbed glass mat (AGM, NSG Corporation) was used as separator. Finally, the electrodes were assembled into Two-electrode Swagelok cells before electrochemical test.

Cyclic voltammetry (CV) measurement was carried out on a Biologic-VMP3 electrochemical workstation at a scan rate of 0.1 mV s^{-1}. Electrochemical impedance spectroscopy (EIS) of the batteries was conducted at the DC potential of 10 mV, with the frequency range from 0.01 Hz to

100 kHz. Two-electrode Swagelok cells were used for galvanostatic charge/discharge cycling at room temperature, using a Neware battery tester at various C-rates, 1-20 C, calculated based on the nominal specific capacity of $LiMn_2O_4$ (1 C=120 mA g^{-1}), between 1.4 and 2.1 V.

4.3 Results and Discussion

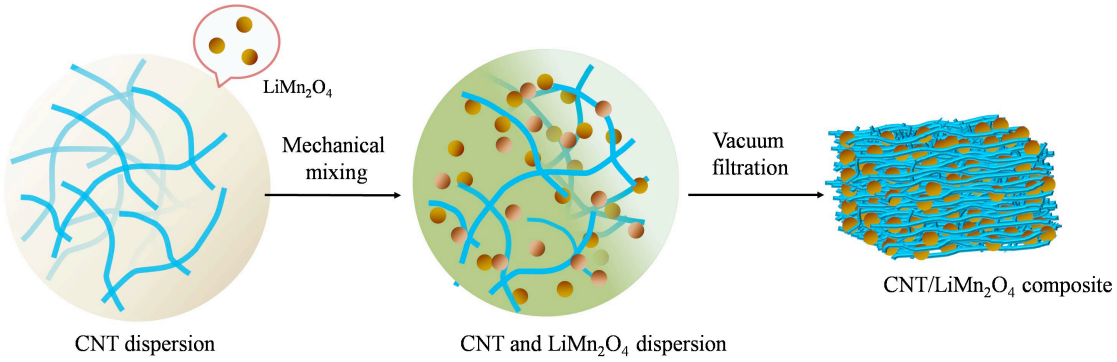

Fig. 4.1 Schematic fabrication of binder-free flexible $LiMn_2O_4$/CNT network electrodes through dispersion and vacuum filtration processes.

A schematic illustration of the formation process of a binder-free flexible $LiMn_2O_4$/CNT electrode is shown in **Fig. 4.1**. First, CNTs were dispersed into a sol-like dispersion using a high-speed fluid shearing method, where CNTs maintained their high aspect ratios, and steadily dispersed in the solvent. Owing to the high aspect ratios, CNTs formed a network structure, which can capture nanoparticles, just like "fishes on nets". After simple mixing and a vacuum filtration process, binder-free flexible $LiMn_2O_4$/CNT electrodes for the ReHAB were available.

Note that $LiMn_2O_4$ nanoparticles are tightly entangled into the composite electrode without binders, forming a porous yet integrated structure. Through our design of the electrode structure, the following benefits can be achieved: (1) the total weight of the electrode is highly reduced, since CNTs simultaneously act as the binder, conductive additive, and current collector; no other

electrochemically inactive additives are introduced in the electrode, increasing the total energy density; (2) the conductivity of the electrode is greatly enhanced due to the good conductivity of CNT networks compared with the traditional conductors and binders, and additives used in surfactant- and/or polymer-assisted synthesis that are usually insulating; (3) the continuous and porous CNT networks facilitate the electrolyte infiltration in addition to electron transfer, so $LiMn_2O_4$ nanoparticles can access Li ions more efficiently; (4) The resilient network structure also alleviates the volume changes of the active material during battery charge/discharge processes, enhancing cycling stability. It is noted that such a synthesis process does not require expensive facilities and extra chemicals, since the CNT dispersion can tightly capture nanoparticles, thereby enabling the fabrication of a structurally stable composite.

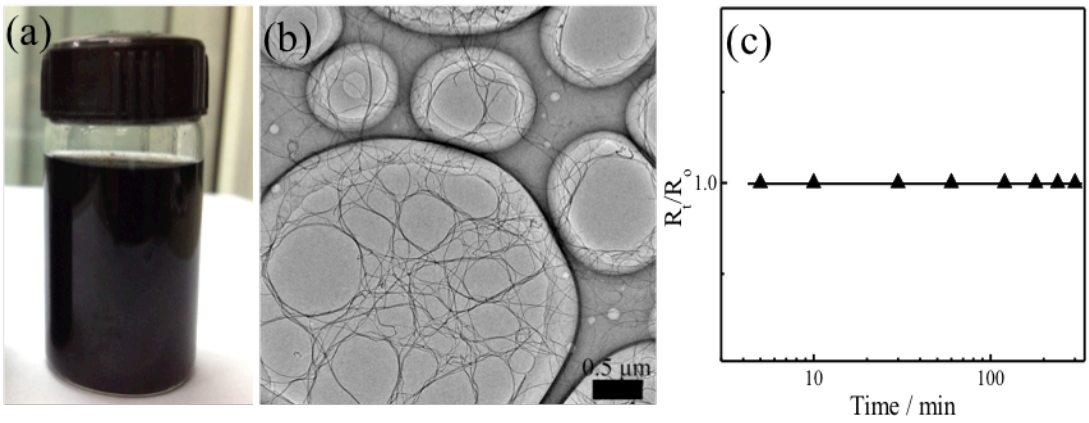

Fig. 4.2 (a) Digital photographs of CNT dispersion of 2.0 mg mL^{-1} after standing one week; (b) TEM image of dispersed CNTs, showing interconnected networks; (c) Resistance changes of 2.0 mg mL^{-1} CNT dispersion varying time.

To make the hybrid electrode, CNTs were dispersed into the networks using a high-speed fluid shearing dispersion, where the high-aspect ratio nanotubes effectively maintain their lengths.

Note that making the CNT dispersion and maintaining the lengths have been difficult. For example, the common methods using ultra-sonication or strong acid oxidation usually destroy CNTs **[9]**. The dispersion could be stably placed more than one week (**Fig. 4.2a**), suggesting the excellent stability of the dispersion. The reason is because that the CNTs were dispersed into the network structure, as confirmed by TEM observation (**Fig. 4.2b**). It displays that the CNTs are in single-dispersion state, and more importantly, form interconnected networks due to the high aspect ratios. **Fig. 4.2c** shows that the dispersion with a CNT concentration of 2.0 mg mL^{-1} has a stable conductivity varying time, further suggesting that the CNTs in the dispersion did not aggregate. Such network structure proves to have high capacity to capture nanoparticles, while mostly reported CNT dispersions with small lengths show very limited such capacity.

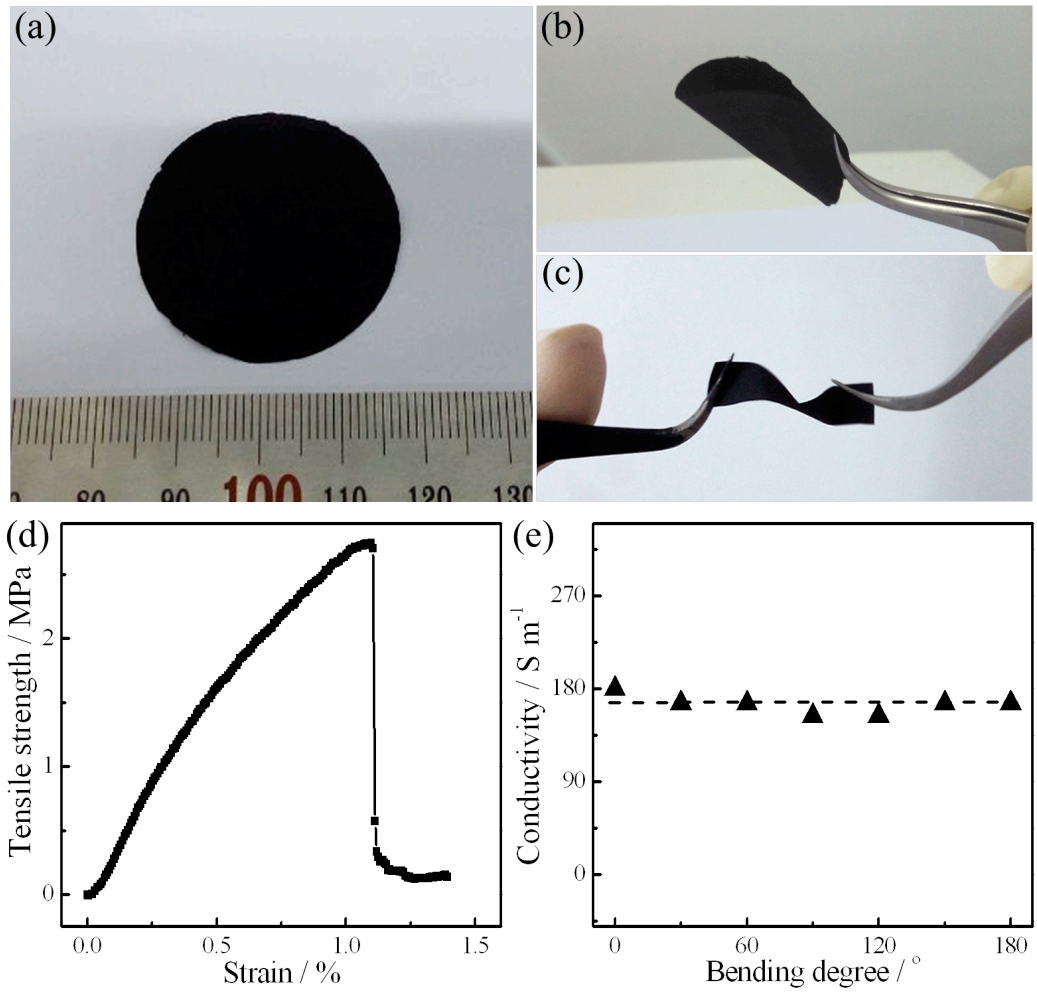

Fig. 4.3 Optical photographs of (a) the produced hybrid film, and the states under various deformations such as (b) bending and (c) twisting; (d) Stress-strain curve of the flexible electrode consisting 90 wt% $LiMn_2O_4$ nanoparticles; (e) Volume conductivity changes of the flexible electrode under bending.

Figure 4.3a shows that the prepared electrode maintains their integrity at large sizes (*e.g.*, 30 mm in diameter). Such hybrid electrode sheets are very flexible, and can be bent under force (**Fig. 4.3b**), or even twisted (**Fig. 4.3c**). Even at a high nanoparticle loading of 90 wt%, the prepared electrodes still retain the high flexibility. **Fig. 4.3d** displays the stress-strain curve of an electrode. Typically, a tensile strength of 2.7 MPa is achieved at a strain of 1.1%. The strength ensured the

stability of the electrode structure, making them promising in actual device applications. The robust structure was further confirmed through electrical conductivity measurements under bending (**Fig. 4.3e**). Indeed, the flexible electrodes with 90 wt% of $LiMn_2O_4$ had a constant conductivity of 170 S m^{-1} under different degrees of bending. Such flexibility was usually not observed in binder-bound electrodes.

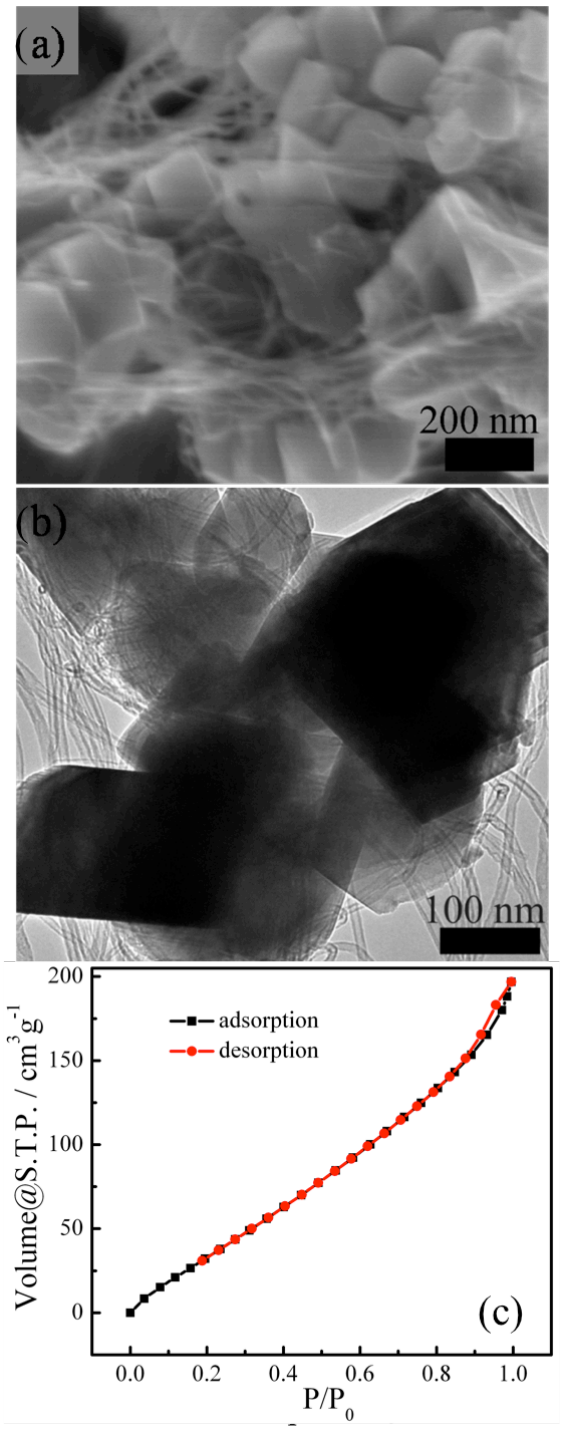

Fig. 4.4 (a) SEM and (b) TEM images of the binder-free flexible $LiMn_2O_4$/CNT electrode; (c) N_2 sorption isotherms of the hybrid electrode.

The structure of the binder-free flexible $LiMn_2O_4$/CNT hybrid is observed under scanning electron microscopy (SEM, **Fig. 4.4a**). Obviously, CNTs and $LiMn_2O_4$ nanoparticles are highly entangled, forming robust composite networks. Such structure endows the electrodes with mentioned mechanical strength. Close TEM observation of the composite shows that their texture is uniform, with threading CNTs interweaved through nanoparticles (**Fig. 4.4b**). The nanocomposites exhibit direct interfacial contact between the CNTs and $LiMn_2O_4$ components, key for the high performance of the electrodes. Moreover, nitrogen sorption isotherms of the binder-free flexible $LiMn_2O_4$/CNT hybrid conforms the interconnected porous channels of this material (**Fig. 4.4c**). The surface area of the electrodes was measured to be 42.7 m^2 g^{-1} with broad pore size distributions. Such pore structure facilitates electrolyte transport, a key factor affecting electrodes' rate performance.

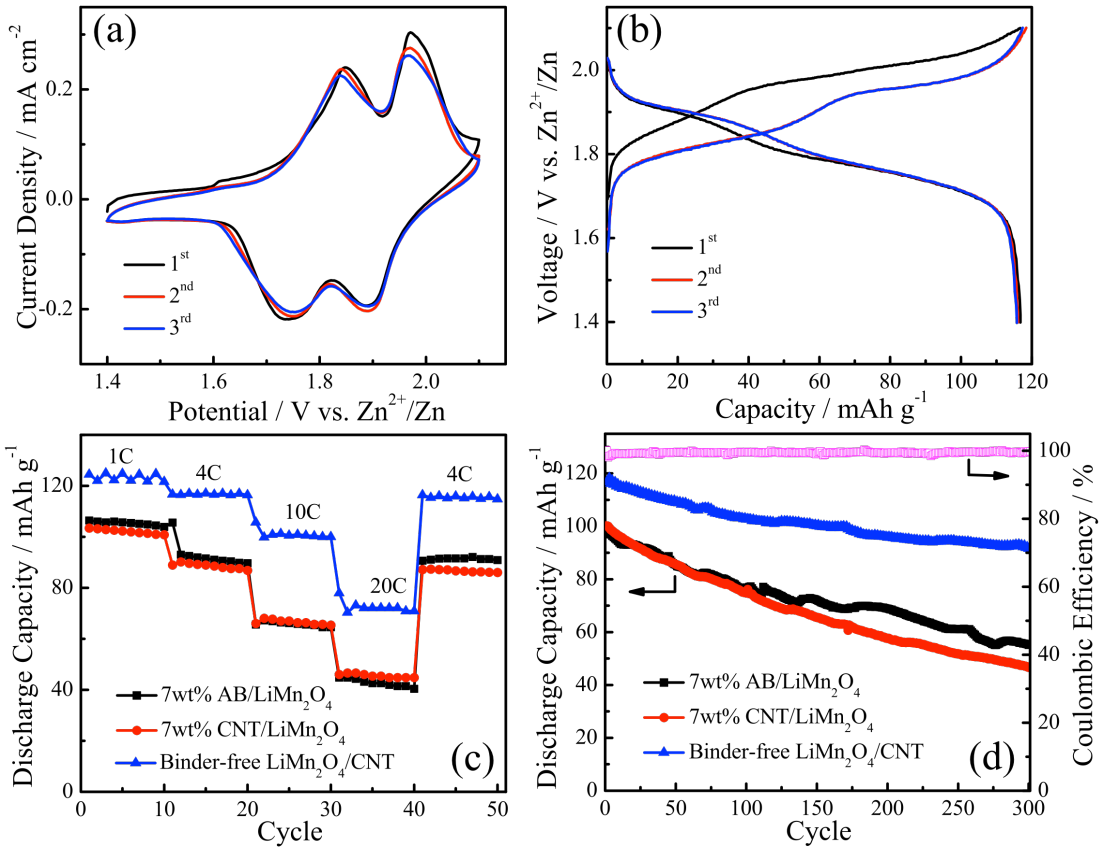

Fig. 4.5 Electrochemical performance of the binder-free $LiMn_2O_4$/CNT network electrode. (a) CV curves of the binder-free $LiMn_2O_4$/CNT electrode collected at a scan rate of 0.1 mV s^{-1}; (b) Charge/discharge curves of the binder-free $LiMn_2O_4$/CNT electrode at 4 C in the potential window of 1.4-2.1 V; (c) Comparison of rate capability of the binder-free $LiMn_2O_4$/CNT, 7wt%CNT/$LiMn_2O_4$, and 7wt%AB/$LiMn_2O_4$ electrodes; (d) Cycling stability of the binder-free $LiMn_2O_4$/CNT electrode at 4 C in comparison with that of the 7wt%CNT/$LiMn_2O_4$ and 7wt%AB/$LiMn_2O_4$ electrodes.

The electrochemical performance of the $LiMn_2O_4$/CNT film electrode was tested as the cathode for the ReHAB **[8, 10, 11]**. The robust structure of the $LiMn_2O_4$/CNT hybrid ensures binder-free electrodes with excellent ion storage performance. Cyclic voltammetry (CV) studies

were first conducted to investigate their lithium storage behaviors (**Fig. 4.5a**). There are two pairs of well-defined redox peaks located at 1.85/1.73 V (1st cycle), 1.84/1.75 V (2nd and 3rd cycle) and 1.98/1.89 V (1st cycle), 1.96/1.89 V (2nd and 3rd cycle) vs. Zn^{2+}/Zn, respectively. They are corresponding to the two stages of extraction/insertion of Li ions from/into the host spinel structure of $LiMn_2O_4$ in the aqueous electrolyte, which could be described as $LiMn_2O_4 \rightleftharpoons Li_{0.5}Mn_2O_4 + 0.5Li^+ + 0.5e^-$ and $Li_{0.5}Mn_2O_4 \rightleftharpoons 2MnO_2 + 0.5Li^+ + 0.5e^-$, respectively. The lithium extraction during the first cycle is slightly different from those observed in subsequent cycles due to the initial activation process of the electrode. From the second cycle, however, the extraction/insertion process becomes stable. The potential differences between oxidation peaks and reduction peaks are contributed to the polarization of the electrode during the CV testing. The potential differences between oxidation peaks and reduction peaks are as small as 0.07 V, resulting partially from the high ionic conductivity of the aqueous electrolyte. The symmetrical peaks reveal that the Li ion extraction/insertion process can be regarded as highly reversible. In addition, the peaks retain the well-defined shapes and almost the same redox potential over the cycles of the scanning process, demonstrating the stability of the $LiMn_2O_4$/CNT electrode.

To further quantify the lithium storage capability, galvanostatic charge/discharge was conducted. **Fig. 4.5b** shows the charge/discharge profiles of the binder-free flexible $LiMn_2O_4$/CNT electrode at 4 C. There are two distinguished plateaus that reflect two-stage Li ion extraction/insertion behavior and are consistent with the obtained CV data. During the cycles, the Coulombic efficiency is close to 100% and remains stable, indicating good reversibility. This further confirms the stability of the binder-free flexible $LiMn_2O_4$/CNT

electrode. It should be noted that the specific discharge capacity of 116 mAh g^{-1} can be comparable to other excellent aqueous battery systems with $LiMn_2O_4$ cathodes **[12]**. Moreover, the charge/discharge curves at different current densities were also performed to evaluate the charge storage behaviors. It shows that the charge/discharge processes of the binder-free flexible $LiMn_2O_4$/CNT electrode are highly reversible, suggesting the excellent reaction kinetics. The excellent ion storage performance contributes to the improved transport in the porous structure of the electrodes and, more importantly, increased electrical conductivity due to ultra-long CNT networks.

The rate capability of the binder-free flexible $LiMn_2O_4$/CNT, 7wt%CNT/$LiMn_2O_4$, and 7wt%AB/$LiMn_2O_4$ electrodes were studied and compared (**Fig. 4.5c**). The specific discharge capacity of the binder-free flexible $LiMn_2O_4$/CNT electrode is significantly larger than that of the 7wt%AB/$LiMn_2O_4$ and 7wt%CNT/$LiMn_2O_4$ electrodes at C-rates from 1 to 20 C. At 20 C, the binder-free flexible $LiMn_2O_4$/CNT electrode still exhibits a specific discharge capacity of 72 mAh g^{-1}, which is much higher than the 7wt%CNT/$LiMn_2O_4$ (45 mAh g^{-1}) and 7wt%AB/$LiMn_2O_4$ (42 mAh g^{-1}) electrodes. Note that such excellent rate performance is comparable or even better than that of $LiMn_2O_4$ cathodes in other aqueous battery systems **[13-24]**.

Except for the excellent rate capability, the binder-free flexible $LiMn_2O_4$/CNT electrode also exhibits remarkable cycling stability. As shown in **Fig. 4.5d**, the composite electrode was cycled at the rate of 4 C. After 300 cycles, the specific discharge capacity of 92 mAh g^{-1} is still retained. Moreover, the Coulombic efficiency is close to 100% during the cycling. In contrast, control electrodes fabricated by mixing $LiMn_2O_4$ with CNTs or AB, and PVdF show significantly lower

stability. The results indicate that the $LiMn_2O_4$/CNT hybrid electrode does significantly improve the cycling stability due to its robust network structure. Since the mechanical test, conductivity test, and EIS measurements all suggest that the binder-free $LiMn_2O_4$/CNT electrode has a stable structure, the capacity fading during cycling may be related to other factors, such as the stability of the Zn anode. Systematic studies on protection of the Zn anode are underway **[25]**. It is expected to improve the cyclability of the battery with this binder-free electrode **[26-28]**.

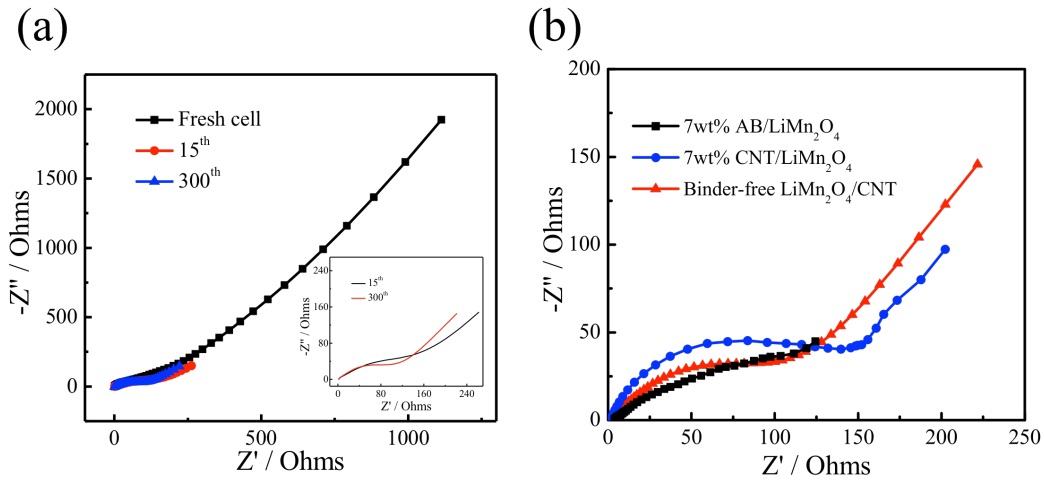

Fig. 4.6 (a) EIS spectra of the batteries made of the pristine binder-free $LiMn_2O_4$/CNT network electrode, after 15 and 300 cycles at 4 C (Inset is the enlarged EIS spectra of the composite electrode after 15 and 300 cycles); (b) EIS spectra of the batteries made of the binder-free $LiMn_2O_4$/CNT network electrode compared to that of the 7wt%CNT/$LiMn_2O_4$ and 7wt%AB/$LiMn_2O_4$ electrodes after 300 cycles at 4 C.

To further investigate the structure and interface stability of the hybrid electrodes during cycling, EIS was conducted along with galvanostaic charge/discharge (**Fig. 4.6a**). The Nyquist plots exhibit a single semicircle at high-to-medium frequency, which is due to the charge transfer resistance and the double-layer capacitance **[29]**. The ohmic resistance of the electrode is nearly constant during cycling, indicating good contacts of the ReHAB as well as structure integrity of

the electrode. Very interestingly, EIS plots of the following cycles almost maintain the same (inset of **Fig. 4.6a**, 15th and 300th), thereby suggesting that the resistances are relatively stable. This suggests that the $LiMn_2O_4$/CNT network structure formed a robust and stable electrode and accordingly, electrode capacity was well maintained. In addition, the EIS plots of the batteries made of the 7wt%CNT/$LiMn_2O_4$ and 7wt%AB/$LiMn_2O_4$ electrodes were measured, and compared with that of the binder-free $LiMn_2O_4$/CNT electrode. As shown in **Fig. 4.6b**, the binder-free flexible $LiMn_2O_4$/CNT electrode displayed a smaller resistance, thereby offering a better rate performance.

4.4 Summary

Highly robust, flexible, binder-free electrodes were synthesized by using long CNTs to capture $LiMn_2O_4$ nanoparticles. Such an robust network architecture possesses abundant porous structures and excellent electrical conductivity, which enables effective charge transport; at the same time, the electrode can be bent and twisted under high mechanical strength, endowing the electrode with high capacity, high rate capability and excellent cyclability for high-performance flexible device applications.

Chapter 5

Using Graphene as New Conductive Additive to Enhance the Rate Performance of $LiMn_2O_4$ Cathode in ReHAB

5.1 Introduction

In the previous chapters, carbon nanotubes (CNTs) have been studied as effective additives for the cathode of the ReHAB. Co-usage of acetylene black (AB) and CNTs in electrodes delivers three-dimensional conductive scaffolds for effective charge transport **[1]**. Graphene, a two-dimensional macromolecular sheet of carbon atoms with a honeycomb structure, has excellent electrical conductivity and mechanical strength; and may be another potential conductive additive in battery electrodes **[2, 3]**. However, graphene is difficult to disperse into electrodes due to its hydrophobic interfacial properties. There are few reports to improve the battery performance sharply when graphene is directly dispersed in electrode **[3]**. It will be exciting to offer a new graphene additive that can highly improve the battery performance by simple mechanical mixing in the electrode.

In this chapter, porous graphene (PG) was synthesized and used as a new conductive additive for the $LiMn_2O_4$ cathode of the ReHAB (**Fig. 5.1**). It is worth mentioning that the PG was used in aqueous batteries for the first time, and it was added into the electrode directly by a simple mechanical mixing method. It indicates that this kind of porous graphene can be easily dispersed compared to the in-plane graphene **[4]**. Also, the porous structure of the PG can store electrolyte for easy access to the active material **[5, 6]**. Based on the structural features of the new conductive additive, the resulting 10wt%PG/$LiMn_2O_4$ electrode exhibits excellent rate capability

and cyclability.

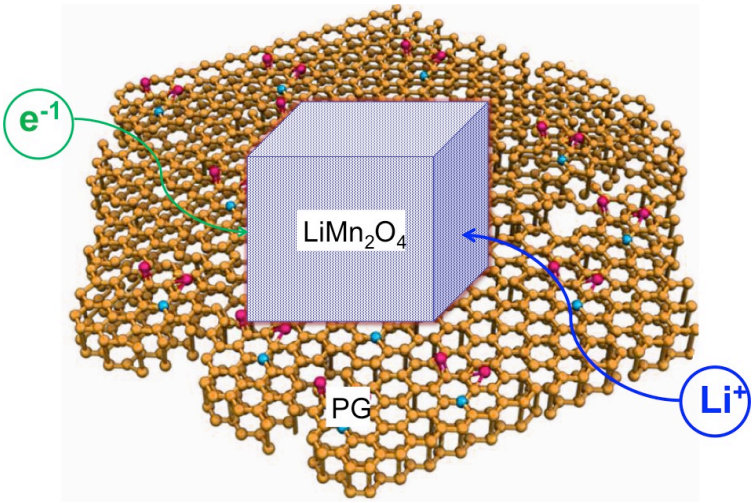

Fig. 5.1 Schematic illustration for the structure of PG we synthesized: the porous structure offering facile aqueous electrolyte access; the graphene sheet providing excellent conductivity.

It needs to point out that the exfoliated graphene (EG) sheets are hydrophobic **[7]**, making the aqueous electrolyte difficult to access. The commonly used reduced graphene oxide, or RGO, has many defects, which are highly susceptible to chemical attack, making the aqueous batteries unstable **[8]**. PG has the following structure features: (1) PG has a porous structure that can allow higher amounts of electrolyte uptake for facile ion transport; (2) PG is prepared from high-temperature chemical vapor deposition, which endows PG with a good conductivity; (3) PG has a sheet-like structure with the size of several hundreds of nanometers, which could offer longer-range continuous conductivity. Based on the key structure properties, PG has obvious advantages that RGO and EG do not have. The synthesis method of this kind of PG is a fluidized-bed CVD method, which has high potential for scaling up to industrial level **[4, 5]**. It is worth mentioning that our electrode preparation method is very simple and effective, making this approach commercially feasible in comparison with other sophisticated and complicated approaches.

5.2 Experimental

5.2.1 Material Preparation

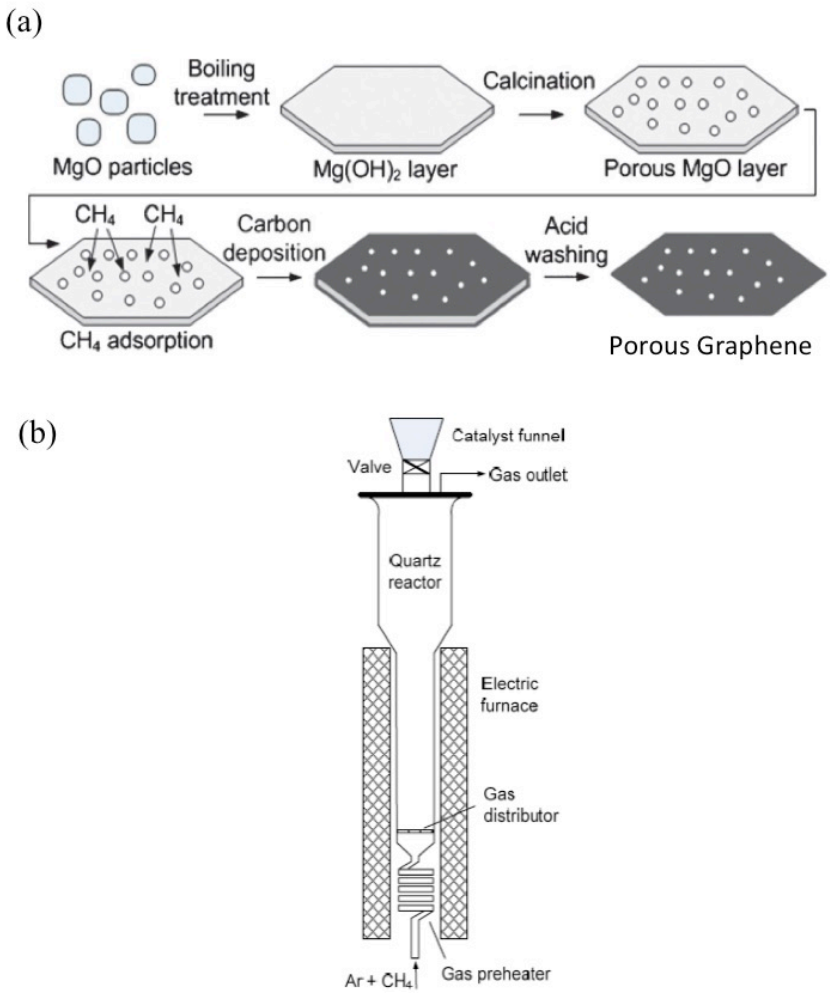

Fig. 5.2 (a) Illustration of the formation of porous graphene; (b) Schematic of the downer reactor for the synthesis of porous graphene (Modified from **Ref. [4]**).

Synthesis of PG **[4, 9]**: the strategy for the preparation of porous MgO layers and the template growth of PG is illustrated in **Fig. 5.2a**. Lamella-like porous MgO layers were prepared by a boiling treatment. First, the as-purchased MgO powder (analytical purity, 20-30 nm particles, Beijing Chemical Reagent Company) was mixed with deionized water under ultrasonic agitation.

The mixture was boiled for 24 h in a reflux apparatus. After filtration and drying, the obtained material was ground into fine powder. Finally, the powder was calcined at 500 °C for 30 min to remove water, resulting in the formation of porous MgO layers.

PG was prepared by a one-step CVD process by using MgO as catalyst. In a typical CVD run, 30 g MgO was loaded into a vertical-set quartz tube furnace with a sintered porous plate as the gas distributor (**Fig. 5.2b**). The reactor was then heated under an Ar flow (1000 mL min^{-1}). Once the temperature reached 875 °C, a methane flow (800 mL min^{-1}) was introduced for 10 min. After cooled to the room temperature, the as-prepared material was taken out, followed by an acid washing using excessive amount of 32% HCl solution (Sigma-Aldrich, ≥ 99% purity) and deionized water, with volume ratio of 1 : 2) with reflux for 1 h to remove MgO. This was followed by filtration and drying at 80 °C overnight in an oven. The material obtained was ground into fine powder.

Synthesis of RGO: RGO was reduced from graphene oxide (GO). GO was synthesized from natural graphite flakes by a modified Hummer's method **[10]**. Firstly, excessive amount of 95.0~98.0% H_2SO_4 solution (Sigma-Aldrich, ≥ 99% purity) and 85% H_3PO_4 solution (Sigma-Aldrich, ≥ 99% purity) were mixed together with the weight ratio of 9 : 1 in a round bottom flask with three necks, then 18 g $KMnO_4$ (Sigma-Aldrich, ≥ 99% purity) was added into the solution; the mixture was placed in an ice bath to prevent the temperature from increasing in the upcoming exothermic reaction. 3 g graphite flake (Alfa Aesar, natural, ~10 mesh, ≥99.9% purity) was then added and the temperature was observed constantly to ensure that it remained between 30 to 40 °C. The mixture was stirred with a rotating speed of 750 rpm at 40 °C for 16 h. After cooled to room temperature, it was poured into 400 mL ice with the temperature remained around 30 °C.

Then, 30% H_2O_2 solution (Sigma-Aldrich, ≥ 99% purity) was added to remove the residue $KMnO_4$. Finally, after centrifugation, washing with 32% HCl solution (Sigma-Aldrich, ≥ 99% purity) and deionized water, as well as sieving (300 μm sieve), the GO was obtained.

Then, 50 mL of GO suspension (1 mg mL^{-1}) was ultra-sonicated for 1 h, in which 0.5 g of reducing agent (hydrazine hydrate) was added. The mixture was treated at 60 °C for 12 h. Finally, the as-prepared sample was freeze-dried overnight to get RGO.

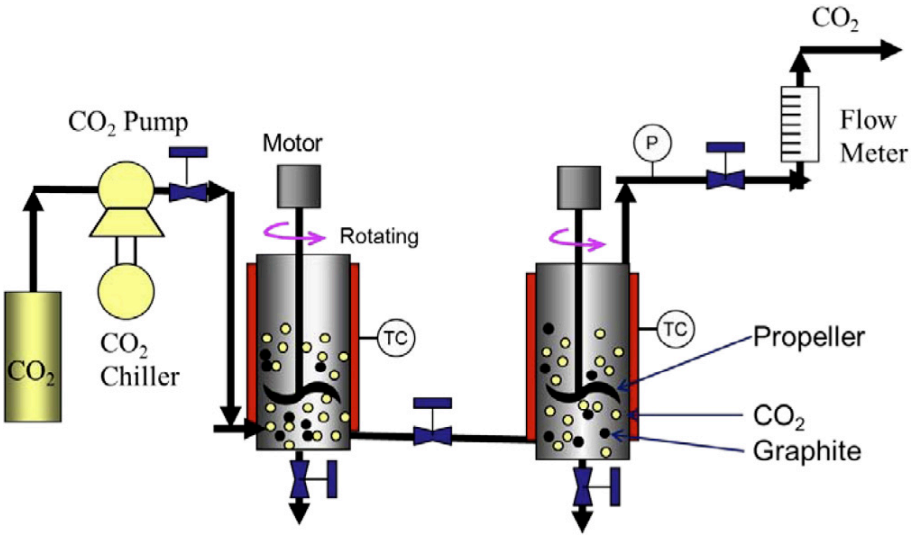

Fig. 5.3 The schematic drawing of experiment device for the synthesis of exfoliated graphene. (Reprinted from **Ref. [7]**)

Synthesis of EG: EG was prepared by a high-speed fluid shearing in supercritical CO_2 **[7]**. The schematic illustration of the experiment device, including a gas cylinder, a chiller, a pump and reactors, is shown in **Fig. 5.3**. Firstly, 1 g graphite was put into the reactor (1.5 L) and heated to 55 °C by an electric furnace. Then, the liquid CO_2 cooled by a chiller was pumped into the reactor. The graphite was exfoliated into graphene under high-speed fluid shear by supercritical CO_2. The exfoliation parameters used in this process are listed: temperature of 55 °C, pressure of

12 MPa, rotating speed of 2000 rpm, and process time of 1 h. After exfoliation, CO_2 was emitted through the vent, and graphene powders were collected. The EG used in my research was provided by Li's group in China University of Petroleum (Beijing).

5.2.2 Physical Characterization

The crystal structure of the as-prepared samples (PG, RGO, and EG) and cathodes was characterized using X-ray diffraction techniques (XRD, Advance D8, Bruker) with Cu-Kα radiation. For XRD analysis of the samples, the grinded powder was filled into the recessed center of the sample plate and compacted by a glass slide, making sure that the surface was flat and kept at the same high as the sample plate; then the sample plate was fixed on the objective table in the XRD equipment for analysis in a range of 5 to 90° (2θ) under 4° min^{-1}; As for the cathodes, an electrode sheet was stuck on the sample plate and then fixed on the objective table in the XRD equipment for analysis in the range of 5 to 90° (2θ) under 4° min^{-1}.

The morphology of the as-prepared samples (PG, RGO, and EG) and cathodes were observed by scanning electron microscopy (SEM, JEOL JSM-6700, JEOL). For SEM analysis, a small amount of the grinded powder of the samples (for the cathodes, a small piece of electrode sheet) was stuck on the conductive tape before observation. The internal morphology was studied using transmission electron microscopy (TEM, FEI T12, FEI) operated at 120 kV. For TEM analysis, a tiny amount of the grinded powder of the samples (for cathodes, a tiny piece of electrode sheet that removed the current collector) was dispersed in ethanol under ultra-sonication agitation for 30 min, and then 0.5 mL of this solution was dropped onto a Cu grid coated by a lacey carbon; followed by drying at 80 °C for 20 min before observation.

The specific surface area (SSA) was calculated by the Brunauer-Emmett-Teller (BET) method with a Micromeritics ASAP 2020 analyzer. The N_2 adsorption-desorption isotherm was collected using a Quantachrome Instrument Autosorb-IQ2-MP-C system at 77 K. Pore-size distribution was calculated based on the Quenched Solid Density Function Theory using the adsorption branch. The conductivities of the as-prepared samples were calculated from the resistance values obtained from a 266 Clamp Meter. Firstly, 0.1 g grinded sample (PG, RGO, and EG) was pressed to disks (diameter: 13 mm, thickness: 2 mm) under 1 MPa with an XRF Briquetting Press (Manual 12 Ton Force, Chemplex Industries, INC.); then the disks were cut into sheets (10 mm × 5 mm) before measurement. The conductivity was calculated based on the equation: $\kappa=L/(RA)$, where R is the resistance values that can be obtained from the 266 Clamp Meter, L is 10 mm, A= 2 mm × 5 mm.

5.2.3 Battery Assembly and Electrochemical Characterization

The composite cathodes were prepared by casting a slurry of 83 wt% $LiMn_2O_4$ (MTI Co. Ltd, ~0.2 μm), 10 wt% carbon conductor (PG, RGO, and EG), and 7 wt% polyvinylidene fluoride (PVdF, Kynar, HSV900) in 1-methyl-2-pyrrolidinone (NMP, Sigma-Aldrich, ≥ 99.5% purity) on graphite foil (Alfa Aesar), and vacuum drying at 60 °C for 24 h. Disks of 12 mm in diameter were cut and soaked in the electrolyte under reduced pressure before battery assembly. Twelve millimeters in diameter polished zinc disks (Rotometals, thickness: 0.2 mm) were used as the anode. The solution of 2 mol L^{-1} Li_2SO_4 (Sigma-Aldrich, ≥ 99% purity) and 1 mol L^{-1} $ZnSO_4$ (Alfa Aesar, ≥ 98% purity) in deionized water was used as electrolyte. pH was adjusted to 4 by titration with 0.1 mol L^{-1} LiOH. Absorbed glass mat (AGM, NSG Corporation) was used as separator.

Cyclic voltammetry (CV) measurement was carried out on a Biologic-VMP3 electrochemical workstation at a scan rate of 0.1 mV s^{-1}. Electrochemical impedance spectroscopy (EIS) of the batteries was conducted at the DC potential of 10 mV, with the frequency range from 0.01 Hz to 100 kHz. Two-electrode Swagelok cells were used for galvanostatic charge/discharge cycling at room temperature, using a Neware battery tester at various C-rates, 1-20 C, calculated based on the nominal specific capacity of $LiMn_2O_4$ (1 C=120 mA g^{-1}), between 1.4 and 2.1 V.

5.3 Results and Discussion

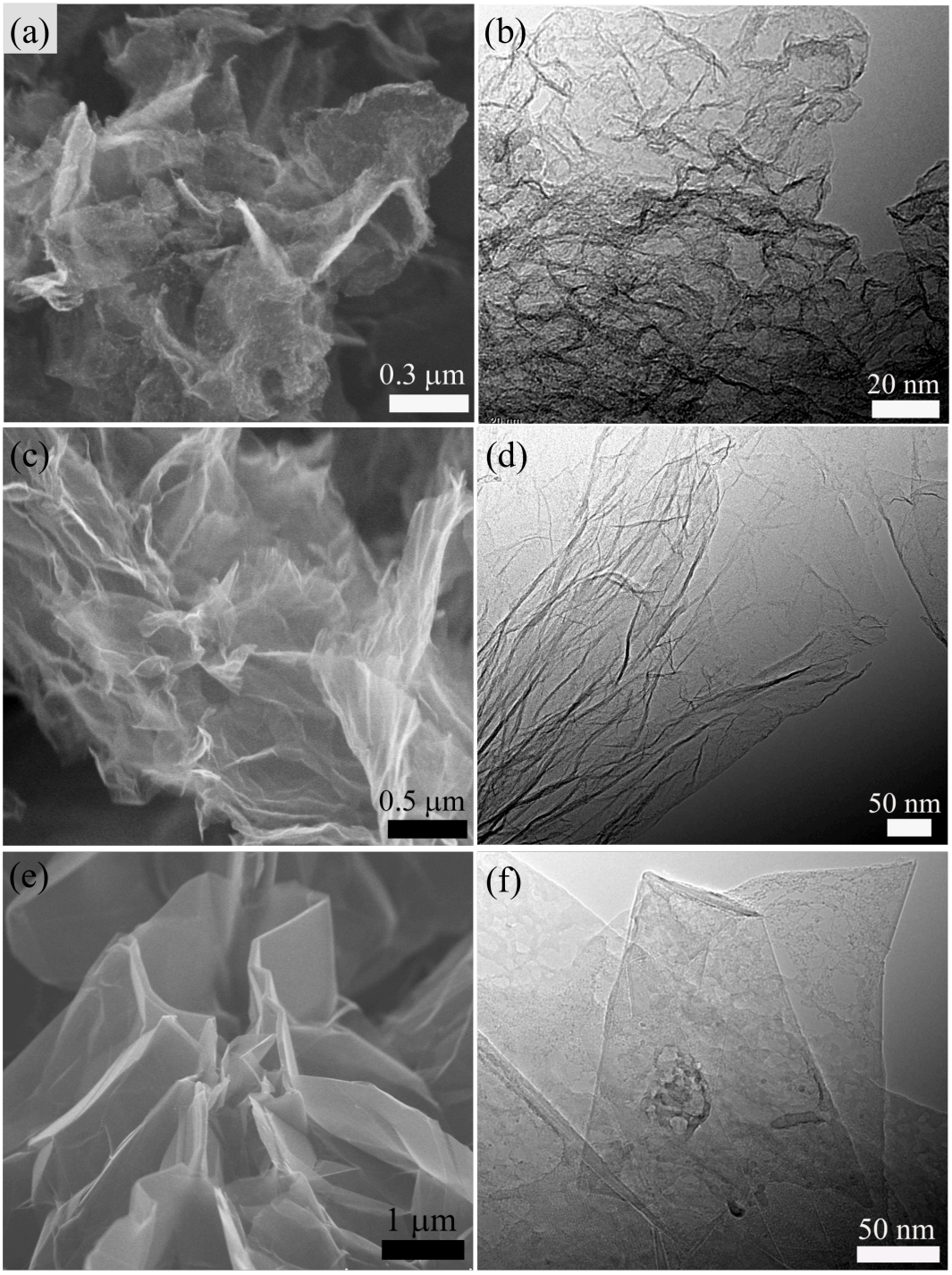

Fig. 5.4 SEM and TEM images of the (a, b) PG, (c, d) RGO, and (e, f) EG.

Porous graphene nanosheet material was prepared by a one-step CVD process, using MgO as the catalyst. **Fig. 5.4a** and **b** display the structure features of the PG. The size of the PG is in the range of several hundreds of nanometers, with the thickness more than several nanometers (**Fig. 5.4a**). In the close observation under TEM, the material's network is continuous, and provides long-range ion and electron access (**Fig. 5.4b**). By comparison, the RGO shows un-regular size, and aggregates randomly (**Fig. 5.4c, d**). The EG displays a typical in-plane structure. It is very difficult to separate them into single or even few layers of sheets (**Fig. 5.4e**). The TEM observation shows that they are still thick; only some of them are separated into few layer sheets (**Fig. 5.4f**). Quite different from the PG, no porous and corrugated structure is observed in the RGO and EG.

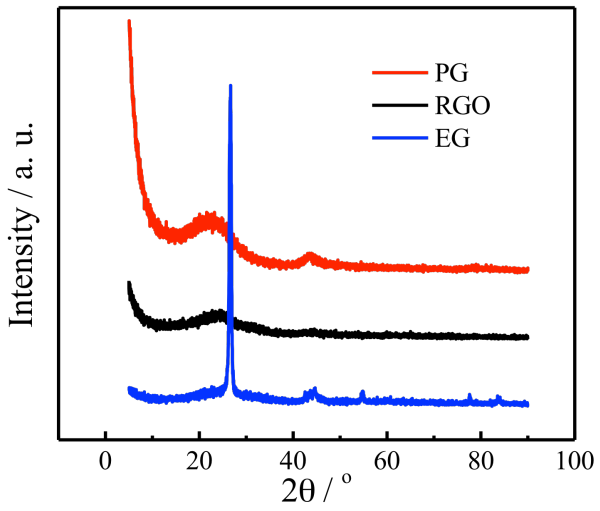

Fig. 5.5 XRD pattern of the PG compared with that of the RGO and EG.

To further compare the structure of the PG with the RGO and EG, XRD characterization was carried out on the three samples. In **Fig. 5.5**, the XRD pattern of the PG displays two weak and

broad diffraction peaks at ~22.6 and 43.8°, which are similar to the porous carbonaceous structure. The broad diffraction peaks could be ascribed to the highly porous structure of the PG that would be further confirmed by N_2 sorption measurement. On the other hand, the XRD pattern of the RGO also shows broad peak at ~22.8°. In contrast, the EG shows high intensity peaks of (002) at 26.5°, due to the high thickness of graphitic layers. The XRD data is consistent with structure morphology observed under electron microscopies.

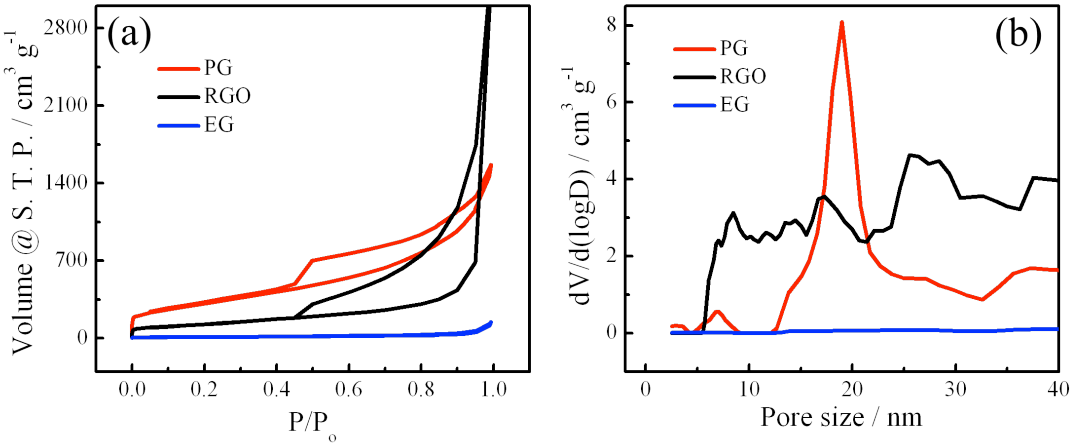

Fig. 5.6 (a) N_2 sorption isotherm and (b) the DFT pore size distribution of the PG, RGO, and EG from nitrogen gas sorption measurement.

PG made from this method has highly porous structure, thereby offering high specific surface areas. Nitrogen gas sorption measurements of the PG shows characteristic of type IV (**Fig. 5.6a**), with a Brunauer-Emmett-Teller (BET) surface area of 1100 m^2 g^{-1}. The specific surface area of the PG is much higher than that of the RGO (450 m^2 g^{-1}) and EG (29 m^2 g^{-1}). The pore size distribution of the PG calculated by the density functional theory model shows an averaged size of 17.2 nm (**Fig. 5.6b**) **[11]**, which is consistent with the TEM observation. On the other hand, the pore size distribution of the RGO is widespread, while there is no obvious pore structure for

the EG. The porous structure of the PG is critical for facile electrolyte transport, which is key for high power performance of the electrodes. In addition, the bulk conductivities of the PG, RGO, and EG were measured, offering the conductivities of 16.4, 12.3, and 920 S cm^{-1}, respectively (**Fig. 5.7** and **Table 5.1**).

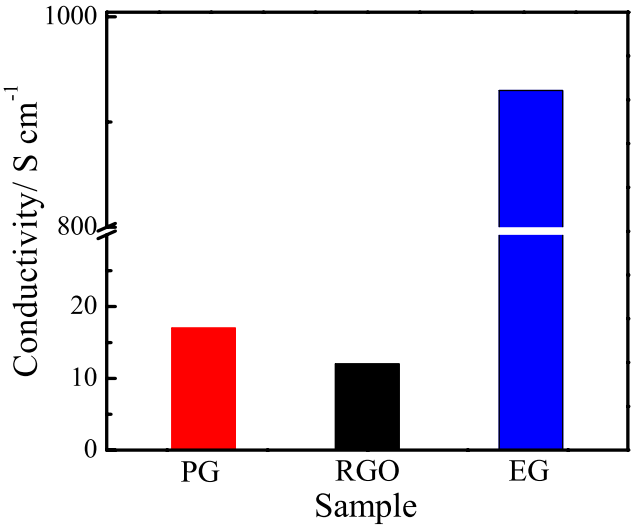

Fig. 5.7 Electrical conductivity of the PG compared with that of the RGO and EG.

Table 5.1 Specific surface area, pore size, and electrical conductivity of the PG, RGO, and EG.

Sample	Surface area / m^2 g^{-1}	Pore size / nm	Conductivity / S cm^{-1}
PG	1100	17.2	16.4
RGO	450	40	12.3
EG	29	-	920

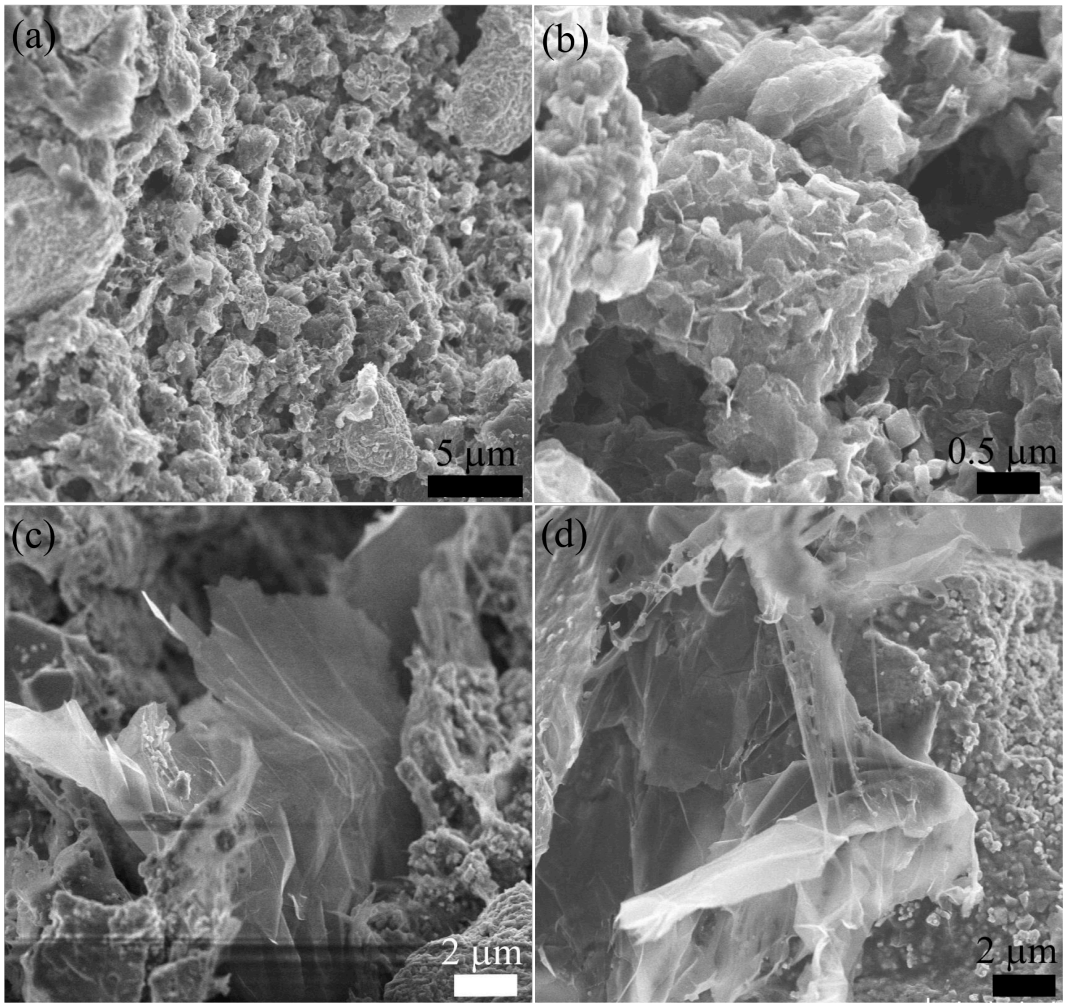

Fig. 5.8 Electrode morphology made from the (a, b) PG, (c) RGO, and (d) EG.

Figure 5.8 compares the SEM images of the electrodes prepared from the PG, RGO, and EG, respectively. In the SEM image of the 10wt%PG/$LiMn_2O_4$ electrode, $LiMn_2O_4$ nanoparticles are uniformly mixed with PG nanosheets. No obviously aggregated PG is observed (**Fig. 5.8a**), although they are only mixed by a simple mechanical stirring method. Moreover, the morphology further confirms that PG nanosheets and $LiMnO_4$ nanoparticles have tight interfacial contacts (**Fig. 5.8b**), thereby offers multiple pathways for effective electrical conductivity. In contrast, in the RGO (**Fig. 5.8c**) and EG (**Fig. 5.8d**) electrodes, the aggregates can be clearly

identified. This is because the difficult dispersion of the RGO during the use in electrodes. As for the EG, the large size and the thickness, as well as the rigid in-plane structure make it difficult to directly disperse in electrodes by simple mechanical mixing.

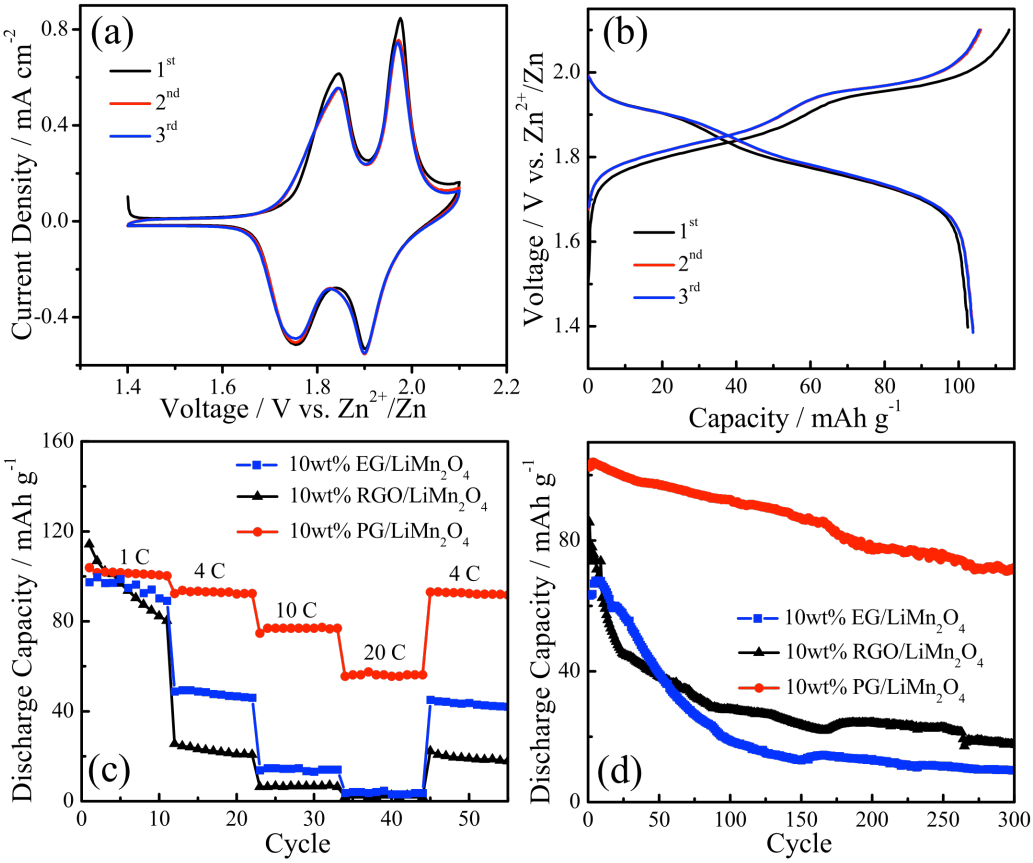

Fig. 5.9 (a) CV curves of the 10wt%PG/$LiMn_2O_4$ electrode collected at a scan rate of 0.1 mV s^{-1}; (b) Charge/discharge curves of the 10wt%PG/$LiMn_2O_4$ electrode at 4 C in the potential window of 1.4-2.1 V; (c) Comparison of rate capability of the 10wt%PG/$LiMn_2O_4$, 10wt%RGO/$LiMn_2O_4$, and 10wt%EG/$LiMn_2O_4$ electrodes; (d) Cycling stability of the 10wt%PG/$LiMn_2O_4$ electrode at a rate of 4 C in comparison with that of the 10wt%RGO/$LiMn_2O_4$ and 10wt%EG/$LiMn_2O_4$ electrodes.

The porous structure of the PG facilitates the transport of Li ions, and its excellent electrical conductivity ensures the 10wt%PG/$LiMn_2O_4$ electrode with excellent Li ion storage performance, which was investigated by various electrochemical characterizations. **Fig. 5.9a** shows the cyclic voltammetry (CV) curves of the 10wt%PG/$LiMn_2O_4$ electrode collected at a scan rate of 0.1 mV s^{-1}. Two pairs of well-defined redox peaks located at 1.85/1.76 V and 1.98/1.90 V vs. Zn^{2+}/Zn are exhibited in the CVs, respectively. They are corresponding to the two stages of extraction/insertion of Li ions from/into the host spinel structure of $LiMn_2O_4$ in the aqueous electrolyte, which could be described as

$LiMn_2O_4 \rightleftharpoons Li_{0.5}Mn_2O_4 + 0.5Li^+ + 0.5e^-$ and $Li_{0.5}Mn_2O_4 \rightleftharpoons 2MnO_2 + 0.5Li^+ + 0.5e^-$, respectively. The small potential differences between oxidation peaks and reduction peaks (0.08 V) are partially due to the high ionic conductivity of the aqueous electrolyte, which also reveals that the Li ion extraction/insertion process can be regarded as highly reversible. Moreover, the well-defined shapes and almost the same redox potential of the peaks over the cycles of the scanning process reveal the stability of the 10wt%PG/$LiMn_2O_4$ electrode. Excellent cycling and rate performance are expected based on the CV response.

Figure 5.9b shows the charge/discharge curves of the 10wt%PG/$LiMn_2O_4$ electrode at 4 C. The 10wt%PG/$LiMn_2O_4$ electrode exhibits the typical voltage platforms, which correspond to the two-stage Li ion extraction/insertion behavior and are consistent with the obtained CV data. The Coulombic efficiency in the fist cycle reaches 90.3%, which is much higher than that in the organic electrolyte **[2, 5, 6, 12]**. In the following cycles, the Coulombic efficiency stays close to 100%, which indicates a good reversibility and further confirms the stability of the 10wt%PG/$LiMn_2O_4$ electrode. The highly reversible charge/discharge processes of the

10wt%PG/$LiMn_2O_4$ electrode are attributed to the excellent reaction kinetics.

Figure 5.9c shows the rate capability of the 10wt%PG/$LiMn_2O_4$, 10wt%RGO/$LiMn_2O_4$, and 10wt%EG/$LiMn_2O_4$ electrodes. Although the initial discharge capacity of the 10wt%PG/$LiMn_2O_4$ electrode (104 mAh g^{-1} at 1 C) is less than that of the 10wt%RGO/$LiMn_2O_4$ electrode (114 mAh g^{-1}), the specific discharge capacity of the 10wt%PG/$LiMn_2O_4$ electrode remains stable, while the specific discharge capacity of the 10wt%RGO/$LiMn_2O_4$ electrode decreases sharply. Additionally, the 10wt%PG/$LiMn_2O_4$ electrode shows significantly higher specific discharge capacity than that of the 10wt%RGO/$LiMn_2O_4$ and 10wt%EG/$LiMn_2O_4$ electrodes in the following cycles at C-rates from 1 to 20 C. Even at 20 C, the 10wt%PG/$LiMn_2O_4$ electrode still delivers a specific discharge capacity of 56 mAh g^{-1}, while the specific discharge capacities of the 10wt%RGO/$LiMn_2O_4$ and 10wt%EG/$LiMn_2O_4$ electrodes are almost zero due to the severe aggregation of the RGO and EG. Therefore, compared to the hydrophobic EG and RGO with huge levels of defects, porous conductive PG exhibits an excellent rate performance.

Except for the excellent rate capability, the 10wt%PG/$LiMn_2O_4$ electrode also exhibits wonderful cycling stability. **Fig. 5.9d** shows the cycling performance of the 10wt%PG/$LiMn_2O_4$, 10wt%RGO/$LiMn_2O_4$, and 10wt%EG/$LiMn_2O_4$ electrodes at the rate of 4 C. Compared to the 10wt%RGO/$LiMn_2O_4$ and 10wt%EG/$LiMn_2O_4$ electrodes, the 10wt%PG/$LiMn_2O_4$ electrode exhibits significantly higher stability. After 300 cycles, the specific discharge capacity of the 10wt%PG/$LiMn_2O_4$ electrode still remains 72 mAh g^{-1}, which is much higher than that of the 10wt%RGO/$LiMn_2O_4$ and 10wt%EG/$LiMn_2O_4$ electrodes, 18 and 10 mAh g^{-1}, respectively. Besides, the Coulombic efficiency of the 10wt%PG/$LiMn_2O_4$ electrode is close to 100% during

the cycling. The electrochemical properties of the 10wt%PG/$LiMn_2O_4$ electrode are compared to those of $LiMn_2O_4$-based aqueous batteries **[2, 13-15]**, and the results suggest that PG nanosheets used in this work show comparable or even better rate capability and cyclability compared to that used carbon blacks and carbon nanotubes **[16]**.

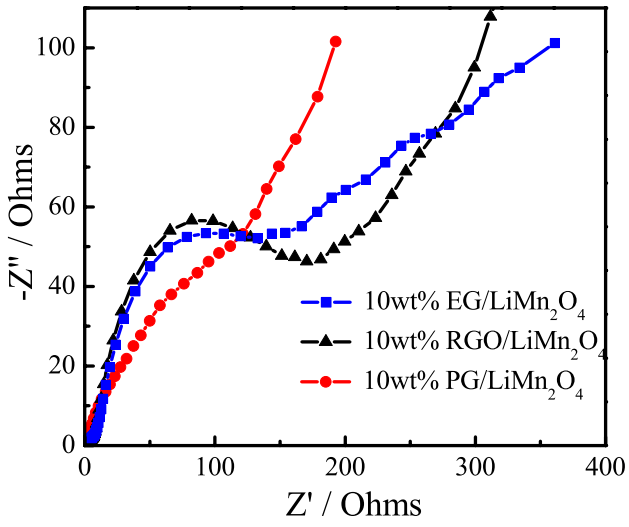

Fig. 5.10 EIS spectra of the batteries made of the 10wt%PG/$LiMn_2O_4$ electrode compared to that of the 10wt%RGO/$LiMn_2O_4$ and 10wt%EG/$LiMn_2O_4$ electrodes after 300 cycles at 4 C.

Electrochemical impedance spectroscopy (EIS) analysis provides evidence to support the excellent electrochemical performance of the 10wt%PG/$LiMn_2O_4$ electrode. **Fig. 5.10** shows the EIS plots of the batteries made of the 10wt%PG/$LiMn_2O_4$, 10wt%RGO/$LiMn_2O_4$, and 10wt%EG/$LiMn_2O_4$ electrodes after 300 charge/discharge cycles at 4 C. The high-to-medium frequency semicircle in EIS plots corresponds to the charge transfer resistance and the double layer capacitance; the inclined line in the low frequency region of the EIS plots corresponds to the Li ion diffusion within $LiMn_2O_4$ particles **[17, 18]**. The size of the semicircle of the

10wt%PG/$LiMn_2O_4$ electrode is smaller than those of the 10wt%RGO/$LiMn_2O_4$ and 10wt%EG/$LiMn_2O_4$ electrodes, indicating a lower charge transfer resistance in the 10wt%PG/$LiMn_2O_4$ electrode. The lower charge transfer resistance contributes to the higher rate capability of the 10wt%PG/$LiMn_2O_4$ electrode.

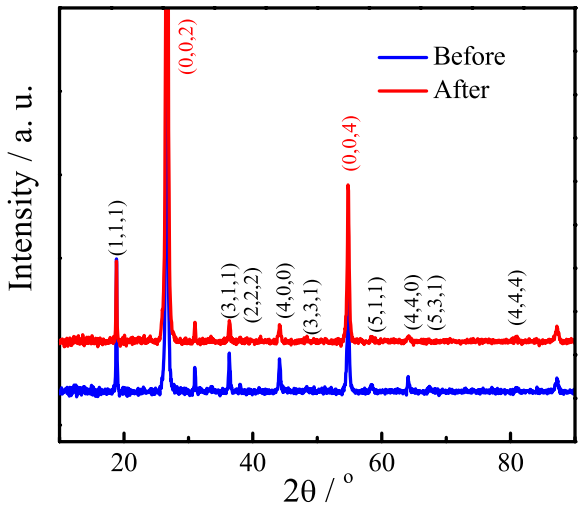

Fig. 5.11 XRD patterns of the 10wt%PG/$LiMn_2O_4$ electrode before and after 300 charge/discharge cycles at 4 C.

Figure 5.11 shows the XRD pattern of the 10wt%PG/$LiMn_2O_4$ electrode before and after 300 charge/discharge cycles. All major peaks are indexed and fit well with the standard pattern **[19]**. After 300 cycles, the peak locations have not changed significantly, which indicates the high stability of $LiMn_2O_4$ during charge/discharge process. The SEM and TEM images of the 10wt%PG/$LiMn_2O_4$ electrode after 300 cycles are shown in **Fig. 5.12**. The morphology of the electrode keeps the closely mixed state (**Fig. 5.12a**). In addition, the PG after cycling retains the corrugated pores (**Fig. 5.12b**), suggesting the robust porous structure. These results further

confirm the stability of the 10wt%PG/$LiMn_2O_4$ electrode during charge/discharge processes; and further convince that the excellent rate capability and cyclability are due to the PG nanosheets, which can provide efficient diffusion channels for Li ions and a highly conductive pathway for electrons.

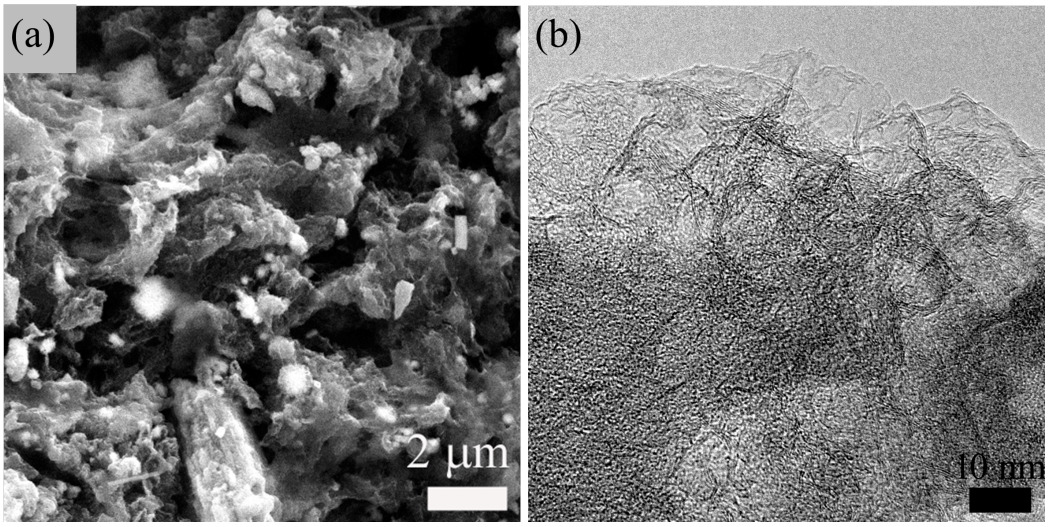

Fig. 5.12 (a) SEM and (b) TEM images of the 10wt%PG/$LiMn_2O_4$ electrode after 300 cycles at 4 C.

5.4 Summary

Porous graphene, or PG, was fabricated, and for the first time used as a conductive additive to the cathode. The PG provides facile access for the electrolyte and high electrical conductivity in the cathode. The PG is easily dispersed into the electrode materials. By simple mechanical mixing, this new conductive nanocarbon highly increases the electrochemical performance of the $LiMn_2O_4$ cathode. It exhibits good cycling performance and reversibility (Coulombic efficiency of almost 100% over 300 charge/discharge cycles at 4 C), along with outstanding rate performance (specific discharge capacity of 56 mAh g^{-1} at 20 C). By comparison, the reduced graphene oxide and exfoliated graphene offer very limited performance improvement, especially

at high C-rates, due to their difficult dispersion in the electrode materials. Porous graphene is an effective graphene additive for aqueous batteries, and it is also expected to be effective in other energy storage applications.

Chapter 6

Building Porous Graphene/Acetylene Black Conductive Network to Enhance the Rate Performance of $LiMn_2O_4$ Cathode in ReHAB

6.1 Introduction

In Chapter 5, the porous graphene (PG) has been investigated as a new conductive additive of the $LiMn_2O_4$ cathode for the ReHAB. Thanks to its porous structure and high electrical conductivity, the $LiMn_2O_4$ cathode with the PG as a conductive additive shows a more excellent rate capability than the other graphene materials, the exfoliated graphene and the reduced graphene oxide. However, the price of the PG is about US \$3000 kg^{-1}, which is about 100 times higher than acetylene black (AB) with a high quality, although the production of the PG has huge potential to scale-up **[1]**. In order to make the battery more competitive, reducing the content of the PG to reduce the cost is crucial. In this Chapter, PG/AB conductive networks were constructed to increase the electrical conductivity of the $LiMn_2O_4$ cathode by a simple mechanical mixing method. At the same time, the effects of the PG nanosheets and AB nanoparticles to the performance of the electrode were investigated. It is interesting to find that the rate performance of the $LiMn_2O_4$ cathode is significantly improved when PG nanosheets and AB nanoparticles coexist in the $LiMn_2O_4$ cathode. The PG/AB conductive networks can provide: (1) conductive contacts between $LiMn_2O_4$ and AB nanoparticles; (2) conductive contacts between $LiMn_2O_4$ nanoparticles and PG nanosheets; (3) physical contacts between AB nanoparticles and PG nanosheets. The PG/AB networks facilitate the transfer of electrons, resulting in an excellent rate performance of the ReHAB.

6.2 Experimental

6.2.1 Material Preparation

Porous graphene (PG) was prepared by the same procedure as present in Chapter 5.2.1.

6.2.2 Physical Characterization

The cathode morphology was observed by scanning electron microscopy (SEM, JEOL JSM-6700, JEOL). For SEM analysis, small pieces of electrode sheets were stuck on the conductive tape before observation. The internal morphology was studied using transmission electron microscopy (TEM, FEI T12, FEI) operated at 120 kV. For TEM analysis, a tiny piece of electrode sheet that removed the current collector was dispersed in ethanol under ultra-sonication agitation for 30 min, and then 0.5 mL of this solution was dropped onto a Cu grid coated by a lacey carbon; followed by drying at 80 °C for 20 min before observation. The electrode structure was characterized using X-ray diffraction techniques (XRD, Advance D8, Brüker) with Cu-Kα radiation. For XRD analysis, the electrode sheets were stuck on the sample plate and then fixed on the objective table in the XRD equipment for analysis in the range of 5 to 90° (2θ) under 4° min^{-1}.

6.2.3 Battery Assembly and Electrochemical Characterization

The composite cathodes were prepared by casting a slurry of 83 wt% $LiMn_2O_4$ (MTI Co. Ltd, ~ 0.2 μm), 10 wt% carbon conductor consisting of PG and acetylene black (AB, MTI) with different weight ratios (PG : AB = 0.5 : 9.5, 1 : 9, 1 : 4, 1 : 2, 1 : 0, and 0 : 1), and 7 wt% polyvinylidene fluoride (PVdF, Kynar, HSV900) in 1-methyl-2-pyrrolidinone (NMP, Sigma-Aldrich, ≥ 99.5% purity) on graphite foil (Alfa Aesar), and vacuum drying at 60 °C for 24 h. The

cathodes prepared are indicated as the 0.5wt%PG/AB/$LiMn_2O_4$, 1wt%PG/AB/$LiMn_2O_4$, 2wt%PG/AB/$LiMn_2O_4$, 3.3wt%PG/AB/$LiMn_2O_4$, 10wt%PG/$LiMn_2O_4$, and 10wt%AB/$LiMn_2O_4$ electrodes, corresponding to different weight ratios of PG to AB as 0.5 : 9.5, 1 : 9, 1 : 4, 1 : 2, 1 : 0, and 0 : 1. Disks of 12 mm in diameter were cut and soaked in the electrolyte under reduced pressure before battery assembly. Twelve millimeters in diameter polished zinc disks (Rotometals, thickness: 0.2 mm) were used as the anode. The solution of 2 mol L^{-1} Li_2SO_4 (Sigma-Aldrich, ≥ 99% purity) and 1 mol L^{-1} $ZnSO_4$ (Alfa Aesar, ≥ 98% purity) in deionized water was used as electrolyte. pH was adjusted to 4 by titration with 0.1 mol L^{-1} LiOH. Absorbed glass mat (AGM, NSG Corporation) was used as separator.

Cyclic voltammetry (CV) measurement was carried out on a Biologic-VMP3 electrochemical workstation at a scan rate of 0.1 mV s^{-1}. Electrochemical impedance spectroscopy (EIS) of the batteries was conducted at the DC potential of 10 mV, with the frequency range from 0.01 Hz to 100 KHz. Two-electrode Swagelok cells were used for galvanostatic charge/discharge cycling at room temperature, using a Neware battery tester at various C-rates, 1-20 C, calculated based on the nominal specific capacity of $LiMn_2O_4$ (1 C=120 mA g^{-1}), between 1.4 and 2.1 V.

6.3 Results and Discussion

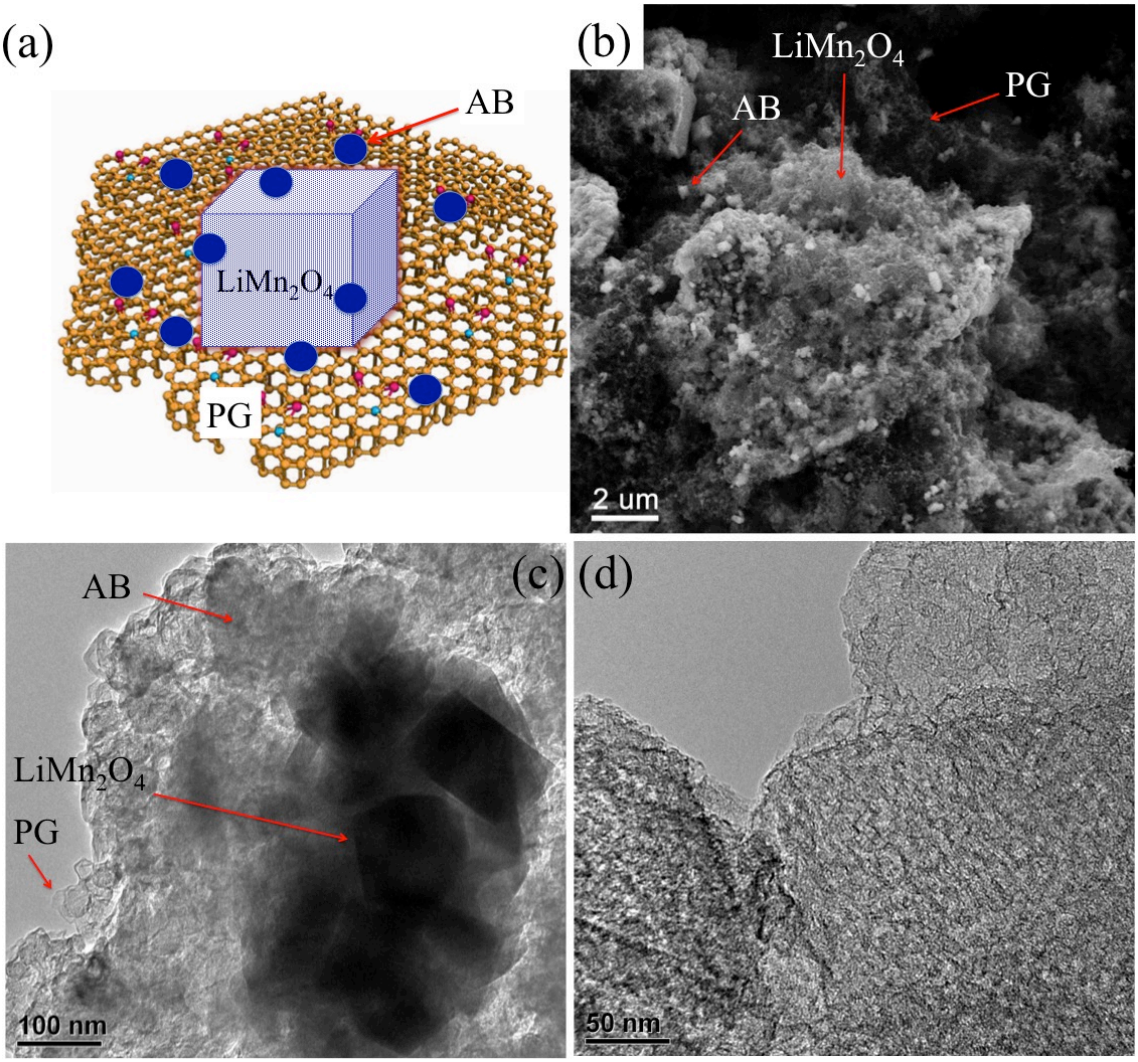

Fig. 6.1 (a) Schematic illustration of the conducting mode of PG/AB/$LiMn_2O_4$ electrodes; SEM (b) and TEM (c, d) of the 3.3wt%PG/AB/$LiMn_2O_4$ electrode.

Figure 6.1a shows the schematic illustration of the conducting mode of PG/AB/$LiMn_2O_4$ electrodes. The PG/AB conductive network can provide: (1) conductive contacts between $LiMn_2O_4$ and AB nanoparticles; (2) conductive contacts between $LiMn_2O_4$ nanoparticles and PG nanosheets; (3) physical contacts between AB nanoparticles and PG nanosheets. As shown in

Fig. 6.1a, the conducting contact between $LiMn_2O_4$ nanoparticles and PG nanosheets is more efficient than that between $LiMn_2O_4$ and AB nanoparticles due to the large surface contact; besides, PG nanosheets with high surface area can provide efficient diffusion channels for Li ions and a highly conductive pathway for electrons **[2]**. It is worth mentioning that the contact between AB nanoparticles and PG nanosheets is necessary to further improve the conductivity of the PG/AB/$LiMn_2O_4$ electrodes. The PG/AB conductive network facilitates the transfer of electron, resulting in an excellent rate capability in comparison with the electrodes prepared previously.

Fig. 6.1b shows the SEM image of the 3.3wt%PG/AB/$LiMn_2O_4$ electrode. As shown in **Fig. 6.1b**, AB nanoparticles distribute effectively on PG nanosheets, constructing PG/AB conductive network; $LiMn_2O_4$ nanoparticles contact with PG nanosheets and AB nanoparticles at the same time. TEM image at a low-magnification also presents the distribution mode of the 3.3wt%PG/AB/$LiMn_2O_4$ electrode (**Fig. 6.1c**) and the more specific morphology of the PG is shown in **Fig. 6.1d**. The PG exhibits a porous morphology with obvious surface corrugations. This pore structure makes the transfer of Li ions much faster. SEM and TEM observations confirm that the PG/AB conductive network can highly increase the effective conductive contacts and thus enhance the electrical conductivity.

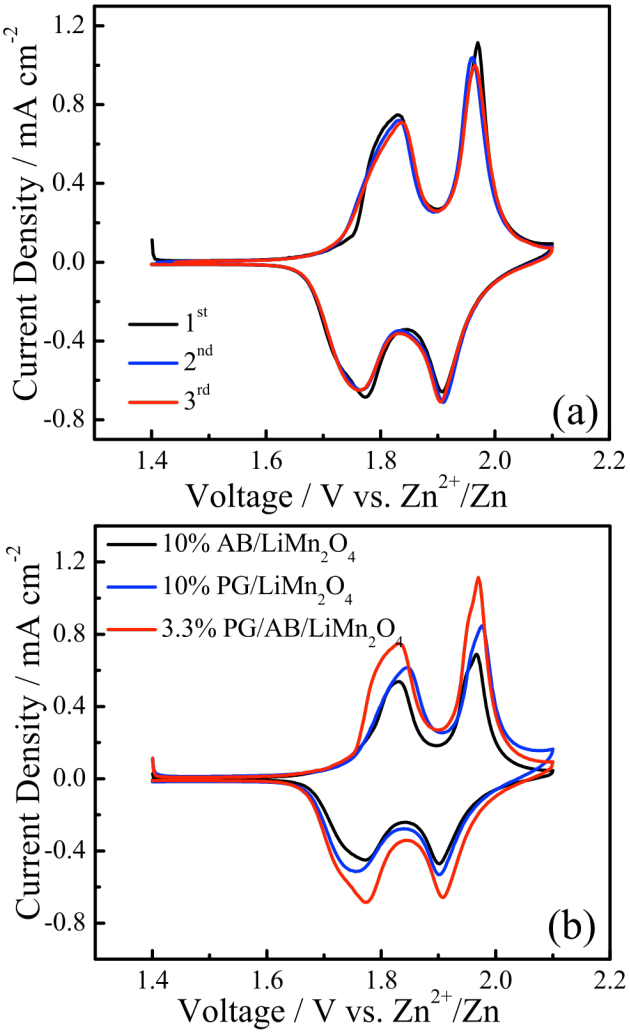

Fig. 6.2 (a) CV curves of the 3.3wt%PG/AB/$LiMn_2O_4$ electrode at 0.1 mV s^{-1}; (b) CV curves of the 10wt%AB/$LiMn_2O_4$, 10wt%PG/$LiMn_2O_4$, and 3.3wt%PG/AB/$LiMn_2O_4$ electrodes at 0.1 mV s^{-1}.

Figure 6.2a shows the CV curves of the 3.3wt%PG/AB/$LiMn_2O_4$ electrode to investigate its Li ion storage behaviors at a scan rate of 0.1 mV s^{-1}. There are two redox couples located at 1.83/1.77 V and 1.97/1.91 V vs. Zn^{2+}/Zn, respectively. They are corresponding to the two stages

of extraction/insertion of Li ions from/into the host spinel structure of $LiMn_2O_4$ in the aqueous electrolyte, which could be described as

$LiMn_2O_4 \rightleftharpoons Li_{0.5}Mn_2O_4 + 0.5Li^+ + 0.5e^-$ and $Li_{0.5}Mn_2O_4 \rightleftharpoons 2MnO_2 + 0.5Li^+ + 0.5e^-$, respectively **[3]**. The potential differences between oxidation/reduction peaks that are due to the polarization of the electrode during CV testing are as small as 0.06 V, resulting partially from the high ionic conductivity of the aqueous electrolyte. The symmetrical peaks indicate that the Li ion extraction/insertion process can be regarded as highly reversible. In addition, the peaks retain the well-defined shapes and almost the same redox potential over the cycles of the scanning process, revealing the stability of the 3.3wt%PG/AB/$LiMn_2O_4$ electrode. Moreover, the CV curves of the 10wt%AB/$LiMn_2O_4$, 10wt%PG/$LiMn_2O_4$, and 3.3wt%PG/AB/$LiMn_2O_4$ electrodes are compared (**Fig. 6.2b**). As shown in **Fig. 6.2b**, the 3.3wt%PG/AB/$LiMn_2O_4$ electrode displays a much larger sectional area than the 10wt%AB/$LiMn_2O_4$ and 10wt%PG/$LiMn_2O_4$ electrodes in the CV curves, which means a larger quantity of Li ions could be reversibly stored/released for the 3.3wt%PG/AB/$LiMn_2O_4$ electrode. This is consistent with the fact that the 3.3wt%PG/AB/$LiMn_2O_4$ electrode has higher specific capacities and better rate performance during charge/discharge tests (see the later parts). Meanwhile, the current densities of the redox peaks in the CV curves for the 3.3wt%PG/AB/$LiMn_2O_4$ electrode are higher than the 10wt%AB/$LiMn_2O_4$ and 10wt%PG/$LiMn_2O_4$ electrodes, which means a lower resistance of the battery made of the 3.3wt%PG/AB/$LiMn_2O_4$ electrode. This can demonstrate that the PG conductive additive (3.3 wt%) has effectively increased the conductivity of the PG/AB/$LiMn_2O_4$ electrode, which contributes to the excellent rate capability.

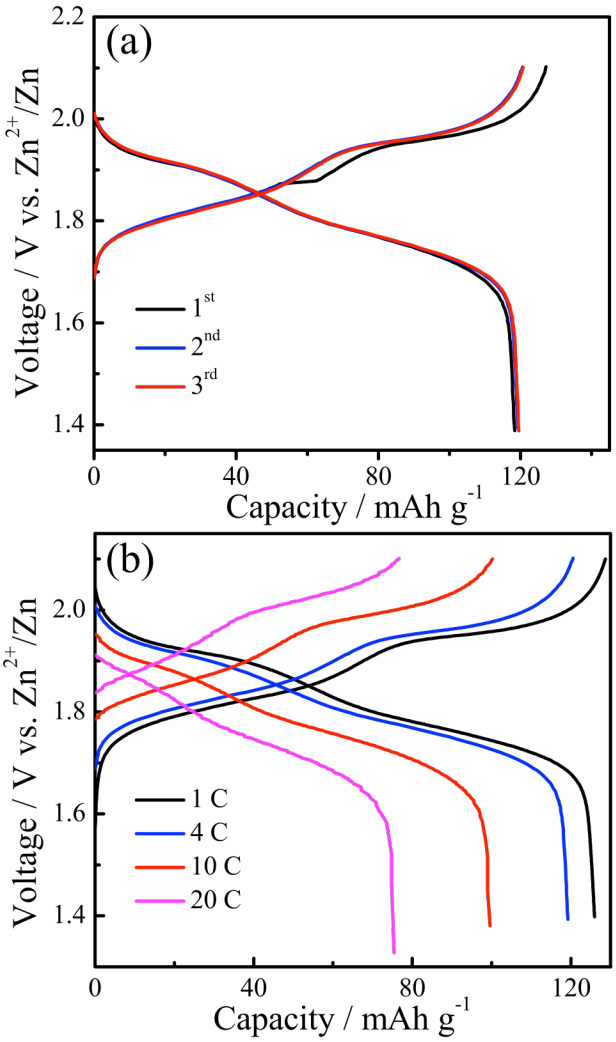

Fig. 6.3 (a) Galvanostatic charge/discharge profiles of the 3.3wt%PG/AB/$LiMn_2O_4$ electrode at 4 C; (b) Galvanostatic charge/discharge profiles of the 3.3wt%PG/AB/$LiMn_2O_4$ electrode at different rates (1 C, 4 C, 10 C, and 20 C).

The galvanostatic charge/discharge processes were conducted to further quantify the Li ion storage capability of the 3.3wt%PG/AB/$LiMn_2O_4$ electrode. **Fig. 6.3a** shows the galvanostatic charge/discharge profiles of the 3.3wt%PG/AB/$LiMn_2O_4$ electrode at 4 C. The two distinguished

plateaus shown on the charge/discharge curves represent the two-stage Li ion extraction/insertion behavior and are consistent with the obtained CV data. Initial specific charge and discharge capacities of the composite cathode are 127 and 118 mAh g^{-1}, respectively, corresponding to a Coulombic efficiency of 92.9%, which is much higher than that in the organic electrolyte **[4-6]**. In the following cycles, the Coulombic efficiency is close to 100% and remains stable, indicating good reversibility. Moreover, the charge/discharge curves at different current densities were also performed to evaluate the charge storage behaviors (**Fig. 6.3b**). It shows that the charge/discharge processes of the 3.3wt%PG/AB/$LiMn_2O_4$ electrode are highly reversible, suggesting the excellent reaction kinetics and further confirming the stability of the composite structure.

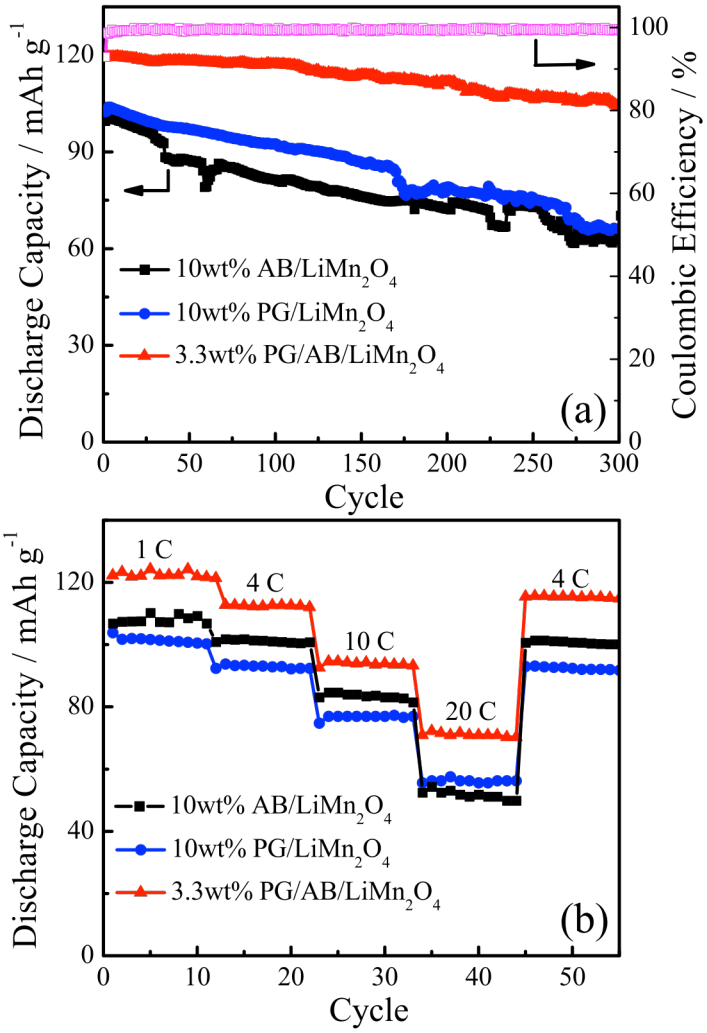

Fig. 6.4 (a) Cyclability of the 3.3wt%PG/AB/$LiMn_2O_4$, 10wt%PG/$LiMn_2O_4$, and 10wt%AB/$LiMn_2O_4$ electrodes at 4 C; (b) Rate capability of the 3.3wt%PG/AB/$LiMn_2O_4$, 10wt%PG/$LiMn_2O_4$, and 10wt%AB/$LiMn_2O_4$ electrodes.

The 3.3wt%PG/AB/$LiMn_2O_4$ electrode exhibits excellent cycling and rate performance (**Fig. 6.4**). **Fig. 6.4a** shows the cycling performance of the 3.3wt%PG/AB/$LiMn_2O_4$ electrode compared with the 10wt%PG/$LiMn_2O_4$ and 10wt%AB/$LiMn_2O_4$ electrodes. The specific

discharge capacity of the 3.3wt%PG/AB/$LiMn_2O_4$ electrode is much higher than the other electrodes. After 300 cycles, the specific discharge capacity of 104 mAh g^{-1} (87.4% of the initial) is still retained. The Coulombic efficiency of the first charge/discharge cycle is ~92.9% due to the instability of charge/discharge process; the Coulombic efficiencies for the following cycles are close to 100%. **Fig. 6.4b** shows the rate performance of the 3.3wt%PG/AB/$LiMn_2O_4$, 10wt%PG/$LiMn_2O_4$, and 10wt%AB/$LiMn_2O_4$ electrodes. The 3.3wt%PG/AB/$LiMn_2O_4$ electrode exhibits higher specific discharge capacity than the other electrodes from 1 C to 20 C. At 20 C, the specific discharge capacity of the 3.3wt%PG/AB/$LiMn_2O_4$ electrode still retains 71 mAh g^{-1}, which is much higher than the 10wt%PG/$LiMn_2O_4$ (56 mAh g^{-1}) and 10wt%AB/$LiMn_2O_4$ (52 mAh g^{-1}) electrodes.

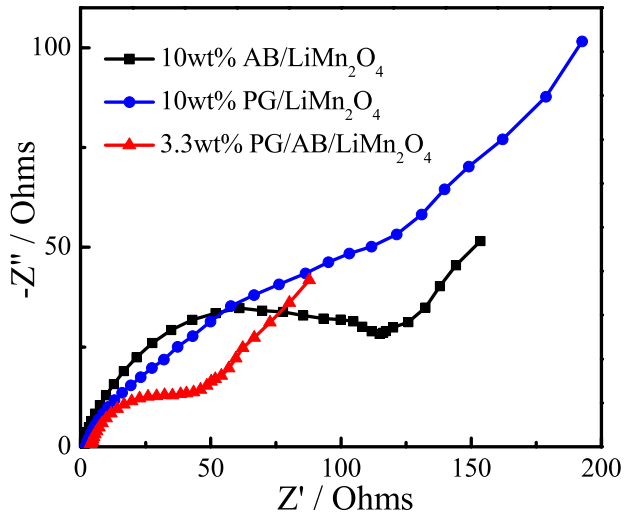

Fig. 6.5 EIS spectra of the batteries made of the 3.3wt%PG/AB/$LiMn_2O_4$, 10wt%PG/$LiMn_2O_4$, and 10wt%AB/$LiMn_2O_4$ electrodes after 300 charge/discharge cycles at 4 C.

Electrochemical impedance spectroscopy plots of the batteries made of the

3.3wt%PG/AB/$LiMn_2O_4$, 10wt%PG/$LiMn_2O_4$, and 10wt%AB/$LiMn_2O_4$ electrodes after 300 charge/discharge cycles at 4 C are shown in **Fig. 6.5**. Each plot consists of a depressed semicircle at the high-to-medium frequency region, corresponding to the charge transfer resistance and the double layer capacitance, and an inclined line in the low frequency region, corresponding to the Li ion diffusion within $LiMn_2O_4$ particles **[7-10]**. The semicircle of the 3.3wt%PG/AB/$LiMn_2O_4$ electrode is smaller than those of the 10wt%AB/$LiMn_2O_4$ and 10wt%PG/$LiMn_2O_4$ electrodes, indicating a smaller charge transfer resistance. This smaller charge transfer resistance is consistent with the higher rate capability of the 3.3wt%PG/AB/$LiMn_2O_4$ electrode.

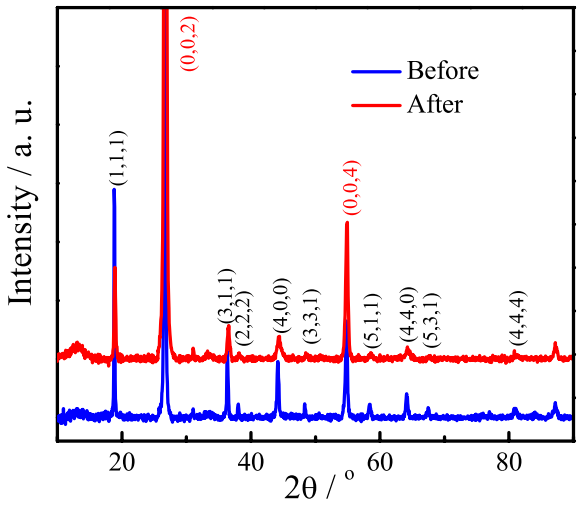

Fig. 6.6 XRD patterns of the 3.3wt%PG/AB/$LiMn_2O_4$ electrode before and after 300 charge/discharge cycles at 4 C.

Figure 6.6 shows the XRD patterns of the 3.3wt%PG/AB/$LiMn_2O_4$ electrode before and after 300 charge/discharge cycles. All major diffraction peaks are fit well with the standard profiles **[5]**. Besides, the locations of the peaks have not changed obviously before and after cycling,

indicating the high stability of the $LiMn_2O_4$ during charge/discharge process. It further confirms that the PG/AB network contributes to the high electrical conductivity and stability of the $LiMn_2O_4$ cathode.

The results above reveal that the electrochemical performances of the battery are highly improved when PG and AB coexist. However, in order to make PG/AB/$LiMn_2O_4$ electrodes more competitive in the market, reducing the content of the PG to reduce the cost of the battery is crucial. The cycling and rate performances of the PG/AB/$LiMn_2O_4$ electrodes with different content of the PG are compared (**Fig. 6.7**). When the content of the PG reduces to 1 wt%, the 1wt%PG/AB/$LiMn_2O_4$ cathode still exhibits at least 19% higher rate capability than the 10wt%AB/$LiMn_2O_4$ cathode (**Fig. 6.7a**), and also keeps a high capacity retention of 82.1% after 300 cycles at 4 C (**Fig. 6.7b**).

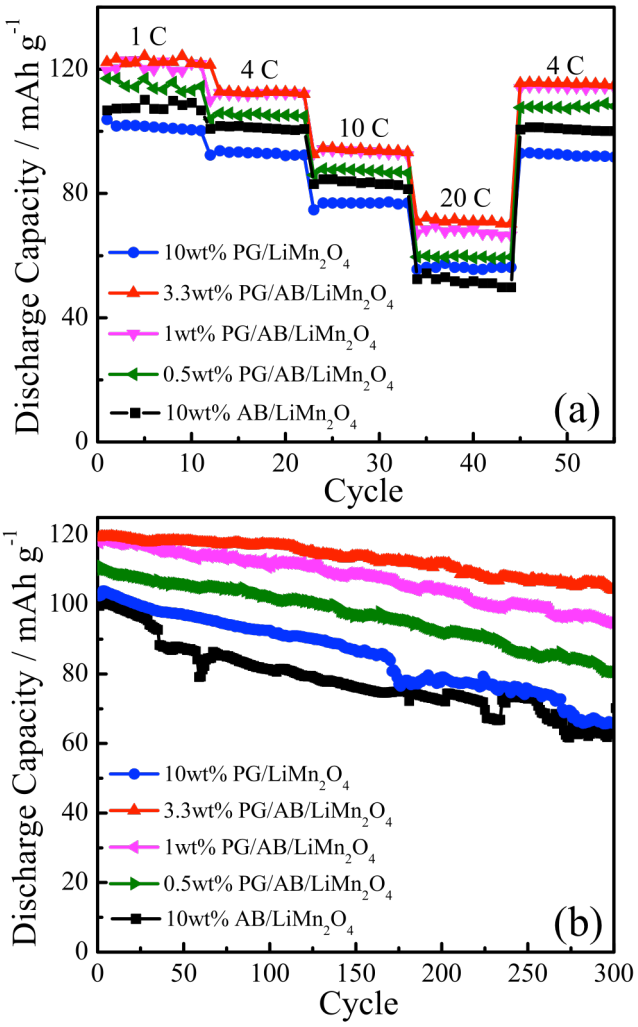

Fig. 6.7 (a) Rate capability of the PG/AB/$LiMn_2O_4$ electrodes with different content of the PG; (b) Cyclability of the PG/AB/$LiMn_2O_4$ electrodes with different content of the PG at 4 C.

6.4 Summary

In order to improve the rate capability of the $LiMn_2O_4$ cathode, PG/AB conductive networks were constructed by simple mechanical mixing. The excellent rate capability contributes to the PG/AB conductive networks, which facilitate the transfer of electrons. Among all

PG/AB/$LiMn_2O_4$ cathodes, the 3.3wt%PG/AB/$LiMn_2O_4$ electrode exhibits the best electrochemical performance with outstanding rate capability (specific discharge capacity of 94 and 71 mAh g^{-1} at 10 C and 20 C, respectively) and good cyclability (Coulombic efficiency of almost 100% over 300 charge/discharge cycles at 4 C). What's more, when the content of the PG reduces to 1 wt%, the 1wt%PG/AB/$LiMn_2O_4$ electrode still exhibits at least 19% higher rate capability than the traditional 10wt%AB/$LiMn_2O_4$ electrode. This is a very simple and effective approach to enhance the rate capability of the $LiMn_2O_4$ cathode, which makes it commercially feasible.

Chapter 7

Final Conclusions and Future Directions

7.1 Final Conclusions

Large-scale energy storage systems are urgently needed to integrate the renewable energy sources into the grid. Aqueous rechargeable batteries are more suitable than lithium ion batteries to be used as large-scale energy storage systems because of their safety, high ionic conductivity and low cost. Among various aqueous batteries that have been used commercially, lead-acid batteries are the most widely used large-scale energy storage system. However, the highly poisoning metal of lead contaminates the environment severely. Our new aqueous Zn/$LiMn_2O_4$ batteries, or ReHAB, are not only environment friendly, but also show comparable power/energy density to lead-acid batteries. Hence, it is extremely meaningful to do research on the ReHAB. Further, improving the rate performance of the $LiMn_2O_4$ cathode is one of the crucial parts of research to get high power density of the ReHAB.

The thesis is focused on preparation of new carbon materials (CNT and graphene) as conductive additives to improve the rate performance of $LiMn_2O_4$ cathode for the ReHAB. The electrochemical performance of the composites prepared by our work is shown in **Table 7.1**.

(1) Mechanical mixing CNTs (PG) and AB with the ratio of 1 : 2 can highly improve the rate capability of $LiMn_2O_4$ cathode, corresponding to the 3.3wt% CNT/AB/$LiMn_2O_4$ and 3.3wt%PG/AB/$LiMn_2O_4$ electrode; PG/AB/$LiMn_2O_4$ cathodes show at least 10% higher capacity retention than CNT/AB/$LiMn_2O_4$ cathodes after 300 cycles at 4 C.

(2) Compared with the 10wt%AB/$LiMn_2O_4$ electrode, the rate capability of the 2wt%CNT/AB/$LiMn_2O_4$ electrode (the weight ratio of CNTs to AB is 1 : 4) can still improve by at least 23%; the rate capability of the 1wt%PG/AB/$LiMn_2O_4$ electrode (the weight ratio of PG to AB is 1 : 9) can still improve by at least 19%.

(3) Binder-free flexible $LiMn_2O_4$/CNT electrode is firstly used in aqueous rechargeable batteries and also shows excellent rate capability and cyclability.

(4) The Nyquist plots of the batteries prepared by our work after 300 charge/discharge cycles were simulated by the equivalent circuit shown in **Fig. 7.1**. The R values of the batteries are obtained and listed in **Table 7.2**. As shown in **Table 7.2**, the R2 values of the batteries with the 3.3wt%CNT/AB/$LiMn_2O_4$, 2wt%CNT/AB/$LiMn_2O_4$, 3.3wt%PG/AB/$LiMn_2O_4$, and 1wt%PG/AB/$LiMn_2O_4$ electrodes are 29.49, 48.13, 35.71 and 45.1 Ω, respectively, which are obviously smaller than those of the batteries with other electrodes. The smaller R2 values mean smaller charge transfer resistances, which contribute to the better rate capability of the batteries.

Table 7.1 The electrochemical performances of the electrodes prepared by our work, where the capacities represent discharge capacity (1 C=120 mAh g^{-1}).

Cathode	Capacity in first cycle at 4C / mAh g^{-1}	Capacity in 300 cycles at 4C / mAh g^{-1}	Capacity retention after 300 cycles at 4 C / %	Capacity at 10 C / mAh g^{-1}	Capacity at 20 C / mAh g^{-1}
10wt%AB/$LiMn_2O_4$	100	64	64	79	51
10wt%CNT/$LiMn_2O_4$	117	84	71.8	84	49
3.3wt%CNT/AB/$LiMn_2O_4$	139	97	69.8	105	73
2wt%CNT/AB/$LiMn_2O_4$	125	91	72.8	97	68
7wt%AB/$LiMn_2O_4$	97	55	56.7	66	45
7wt%CNT/$LiMn_2O_4$	100	47	47	67	47
flexible $LiMn_2O_4$/CNT	117	93	79.5	100	72
10wt%EG/$LiMn_2O_4$	63	10	15.9	15	4
10wt%RGO/$LiMn_2O_4$	85	18	21.2	7	2
10wt%PG/$LiMn_2O_4$	102	72	70.6	77	56
3.3wt%PG/AB/$LiMn_2O_4$	119	104	87.4	94	71
1wt%PG/AB/$LiMn_2O_4$	117	96	82.1	94	68

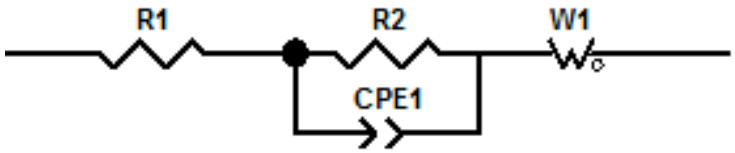

Fig. 7.1 The equivalent circuits for the EIS analysis. R1 represents electrolyte resistance; R2 represents charge transfer resistance; CPE1 represents the double-layer capacitance; W1 represents Warburg impedance.

Table 7.2 The R values of the batteries made of the electrodes prepared by our work calculated from the equivalent circuits.

Cathode	R1 / Ω	R2 / Ω
10wt%AB/$LiMn_2O_4$	1.024	102.3
10wt%CNT/$LiMn_2O_4$	2.728	79.02
3.3wt%CNT/AB/$LiMn_2O_4$	2.632	29.49
2wt%CNT/AB/$LiMn_2O_4$	2.41	48.13
7wt%AB/$LiMn_2O_4$	3.269	105.7
7wt%CNT/$LiMn_2O_4$	1.726	110.5
flexible $LiMn_2O_4$/CNT	2.456	76.8
10wt%EG/$LiMn_2O_4$	2.453	120.2
10wt%RGO/$LiMn_2O_4$	3.129	123
10wt%PG/$LiMn_2O_4$	1.818	91
3.3wt%PG/AB/$LiMn_2O_4$	3.869	35.71
1wt%PG/AB/$LiMn_2O_4$	3.291	45.1

7.2 Future Directions

The experimental results reveal that mixing AB with CNTs or PG at an appropriate weight ratio can obviously improve the rate performance of the $LiMn_2O_4$ cathode. Note that the electrode preparation here is very simple and effective, making this approach commercially feasible in comparison with other sophisticated and complicated approaches. However, many issues still remain unsolved and intensive research efforts are needed to address them, for example:

(1) The normal prices for high quality AB, MWNTs, and PG are about US \$30 kg^{-1}, US \$100 kg^{-1}, and US \$3000 kg^{-1}, respectively. It is competitive to replace 2 wt% of AB with MWNTs to improve the rate capability by 20%. Nevertheless, it is not attractive to obtain the same

improvement by replacing 1 wt% of AB with PG due to the extremely high price of PG. It is thus crucial to achieve the mass production of PG with lower price and high quality.

(2) Substitutional doping of CNTs (graphene) with different atoms (*e.g.*, B, N, and S) can not only tailor the electronic properties of the sp^2 carbon structures but also alter their chemical reactivity; therefore, atom-doped CNTs (graphene) will be prepared and used as conductive additives of $LiMn_2O_4$ cathode for the ReHAB.

(3) The deposition and dissolution rate of zinc at the anode also affects the rate capability of the ReHAB, systematic studies of the Zn anode are needed. Besides, active carbon or PG can be developed as new anode materials to solve this problem.

Although many obstacles still need to be overcome before the commercialization of the ReHAB, major advances in both the performance enhancement and the mechanism elucidation of the ReHAB have been reported. It is believed that further investigation will eventually lead to the practical application of the ReHAB in the near future.

Letter of Copyright Permission

Copyright Clearance Center RightsLink®

Home | Account Info | Help

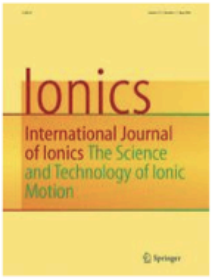

Title: Enhancing rate performance of LiMn2O4 cathode in rechargeable hybrid aqueous battery by hierarchical carbon nanotube/acetylene black conductive pathways

Author: Xiao Zhu

Publication: Ionics

Publisher: Springer

Date: Jan 1, 2015

Copyright © 2015, Springer-Verlag Berlin Heidelberg

Logged in as:
Xiao Zhu
Account #:
3001156985
LOGOUT

Order Completed

Thank you for your order.

This Agreement between Ms. Xiao Zhu ("You") and Springer ("Springer") consists of your license details and the terms and conditions provided by Springer and Copyright Clearance Center.

Your confirmation email will contain your order number for future reference.

Printable details.

License Number	4119550128922
License date	May 31, 2017
Licensed Content Publisher	Springer
Licensed Content Publication	Ionics
Licensed Content Title	Enhancing rate performance of LiMn2O4 cathode in rechargeable hybrid aqueous battery by hierarchical carbon nanotube/acetylene black conductive pathways
Licensed Content Author	Xiao Zhu
Licensed Content Date	Jan 1, 2015
Licensed Content Volume	22
Licensed Content Issue	1
Type of Use	Thesis/Dissertation
Portion	Full text
Number of copies	6
Author of this Springer article	Yes and you are the sole author of the new work
Order reference number	
Title of your thesis / dissertation	Nanocarbon-containing High Power Cathode for Rechargeable Hybrid Aqueous Battery
Expected completion date	May 2017
Estimated size(pages)	140
Requestor Location	Ms. Xiao Zhu 200 University Avenue West waterloo, ON N2L 3G1 Canada Attn: Ms. Xiao Zhu
Billing Type	Invoice
Billing address	Ms. Xiao Zhu 255 sunview waterloo, ON N2L 3V8 Canada Attn: Ms. Xiao Zhu
Total	0.00 CAD

ORDER MORE | CLOSE WINDOW

Copyright Clearance Center RightsLink®

Home | Account Info | Help

Title: Binder-free flexible LiMn2O4/carbon nanotube network as high power cathode for rechargeable hybrid aqueous battery

Author: Xiao Zhu,Xianwen Wu,The Nam Long Doan,Ye Tian,Hongbin Zhao,P. Chen

Publication: Journal of Power Sources

Publisher: Elsevier

Date: 15 September 2016

Logged in as:
Xiao Zhu
Account #:
3001156985
LOGOUT

Order Completed

Thank you for your order.

This Agreement between Ms. Xiao Zhu ("You") and Elsevier ("Elsevier") consists of your license details and the terms and conditions provided by Elsevier and Copyright Clearance Center.

Your confirmation email will contain your order number for future reference.

Printable details.

License Number	4119550968755
License date	May 31, 2017
Licensed Content Publisher	Elsevier
Licensed Content Publication	Journal of Power Sources
Licensed Content Title	Binder-free flexible LiMn2O4/carbon nanotube network as high power cathode for rechargeable hybrid aqueous battery
Licensed Content Author	Xiao Zhu,Xianwen Wu,The Nam Long Doan,Ye Tian,Hongbin Zhao,P. Chen
Licensed Content Date	Sep 15, 2016
Licensed Content Volume	326
Licensed Content Issue	n/a
Licensed Content Pages	7
Type of Use	reuse in a thesis/dissertation
Portion	full article
Format	both print and electronic
Are you the author of this Elsevier article?	Yes
Will you be translating?	No
Order reference number	
Title of your thesis/dissertation	Nanocarbon-containing High Power Cathode for Rechargeable Hybrid Aqueous Battery
Expected completion date	May 2017
Estimated size (number of pages)	140
Elsevier VAT number	GB 494 6272 12
Requestor Location	Ms. Xiao Zhu 200 University Avenue West waterloo, ON N2L 3G1 Canada Attn: Ms. Xiao Zhu
Total	0.00 CAD

ORDER MORE | CLOSE WINDOW

References

Chapter 1

[1] P. Simon, Y. Gogotsi, Materials for electrochemical capacitors, Nature Materials 7 (2008) 845-854.

[2] W. Li, J. Dahn, Lithium-ion cells with aqueous electrolytes, Journal of The Electrochemical Society 142 (1995) 1742-1746.

[3] C.D. Wessells, S.V. Peddada, R.A. Huggins, Y. Cui, Nickel hexacyanoferrate nanoparticle electrodes for aqueous sodium and potassium ion batteries, Nano Letters 11 (2011) 5421-5425.

[4] W. Tang, L. Liu, S. Tian, L. Li, Y. Yue, Y. Wu, S. Guan, K. Zhu, Nano-$LiCoO_2$ as cathode material of large capacity and high rate capability for aqueous rechargeable lithium batteries, Electrochemistry Communications 12 (2010) 1524-1526.

[5] H. Heli, H. Yadegari, A. Jabbari, Investigation of the lithium intercalation behavior of nanosheets of LiV_3O_8 in an aqueous solution, The Journal of Physical Chemistry C 115 (2011) 10889-10897.

[6] M. Pasta, C.D. Wessells, R.A. Huggins, Y. Cui, A high-rate and long cycle life aqueous electrolyte battery for grid-scale energy storage, Nature Communications 3 (2012) 1149.

[7] E. Hosono, T. Kudo, I. Honma, H. Matsuda, H. Zhou, Synthesis of single crystalline spinel $LiMn_2O_4$ nanowires for a lithium ion battery with high power density, Nano Letters 9 (2009) 1045-1051.

[8] D.K. Kim, P. Muralidharan, H.W. Lee, R. Ruffo, Y. Yang, C.K. Chan, H. Peng, R.A. Huggins, Y. Cui, Spinel $LiMn_2O_4$ nanorods as lithium ion battery cathodes, Nano Letters 8 (2008) 3948-3952.

[9] X. Jia, Z. Chen, X. Cui, Y. Peng, X. Wang, G. Wang, F. Wei, Y. Lu, Building robust architectures of carbon and metal oxide nanocrystals toward high-performance anodes for lithium-ion batteries, ACS Nano 6 (2012) 9911-9919.

[10] C. Wu, Z. Hu, W. Wang, M. Zhang, J. Yang, Y. Xie, Synthetic paramontroseite VO_2 with good aqueous lithium-ion battery performance, Chemical Communications 33 (2008) 3891-3893.

[11] W. Tang, S. Tian, L. Liu, L. Li, H. Zhang, Y. Yue, Y. Bai, Y. Wu, K. Zhu, Nanochain $LiMn_2O_4$ as ultra-fast cathode material for aqueous rechargeable lithium batteries, Electrochemistry Communications 13 (2011) 205-208.

[12] Q. Qu, L. Fu, X. Zhan, D. Samuelis, J. Maier, L. Li, S. Tian, Z. Li, Y. Wu, Porous $LiMn_2O_4$ as cathode material with high power and excellent cycling for aqueous rechargeable lithium batteries, Energy & Environmental Science 4 (2011) 3985-3990.

[13] W. Tang, L. Liu, S. Tian, L. Li, Y. Yue, Y. Wu, K. Zhu, Aqueous supercapacitors of high energy density based on MoO_3 nanoplates as anode material, Chemical Communications 47 (2011) 10058-10060.

[14] Q. Qu, Y. Zhu, X. Gao, Y. Wu, Core-shell structure of polypyrrole grown on V_2O_5 nanoribbon as high performance anode material for supercapacitors, Advanced Energy Materials 2 (2012) 950-955.

[15] W. Tang, X. Gao, Y. Zhu, Y. Yue, Y. Shi, Y. Wu, K. Zhu, A hybrid of V_2O_5 nanowires and MWCNTs coated with polypyrrole as an anode material for aqueous rechargeable lithium batteries with excellent cycling performance, Journal of Materials Chemistry 22 (2012) 20143-20145.

[16] C. Wessells, R.A. Huggins, Y. Cui, Recent results on aqueous electrolyte cells, Journal of Power Sources 196 (2011) 2884-2888.

[17] W. Li, J. Dahn, D. Wainwright, Rechargeable lithium batteries with aqueous electrolytes, Science 264 (1994) 1115-1118.

[18] H. Wang, K. Huang, Y. Zeng, S. Yang, L. Chen, Electrochemical properties of TiP_2O_7 and $LiTi_2(PO_4)_3$ as anode material for lithium ion battery with aqueous solution electrolyte, Electrochimica Acta 52 (2007) 3280-3285.

[19] J.Y. Luo, W.J. Cui, P. He, Y.Y. Xia, Raising the cycling stability of aqueous lithium-ion batteries by eliminating oxygen in the electrolyte, Nature Chemistry 2 (2010) 760-765.

[20] X. Wang, Y. Hou, Y. Zhu, Y. Wu, R. Holze, An aqueous rechargeable lithium battery using coated Li metal as anode, Scientific Reports 3 (2013) 1401.

[21] C. Xu, B. Li, H. Du, F. Kang, Energetic zinc ion chemistry: The rechargeable zinc ion battery, Angewandte Chemie 124 (2012) 957-959.

[22] J. Whitacre, A. Tevar, S. Sharma, $Na_4Mn_9O_{18}$ as a positive electrode material for an aqueous electrolyte sodium-ion energy storage device, Electrochemistry Communications 12 (2010) 463-466.

[23] S.I. Park, I. Gocheva, S. Okada, J.i. Yamaki, Electrochemical properties of $NaTi_2(PO_4)_3$ anode for rechargeable aqueous sodium-ion batteries, Journal of The Electrochemical Society 158 (2011) A1067-A1070.

[24] W. Wu, A. Mohamed, J. Whitacre, Microwave synthesized $NaTi_2(PO_4)_3$ as an aqueous sodium-ion negative electrode, Journal of The Electrochemical Society 160 (2013) A497-A504.

[25] Z. Li, D. Young, K. Xiang, W.C. Carter, Y.Ä. Chiang, Towards high power high energy aqueous sodium batteries: The $NaTi_2(PO_4)_3/Na_{0.44}MnO_2$ System, Advanced Energy Materials 3 (2013) 290-294.

[26] C.D. Wessells, R.A. Huggins, Y. Cui, Copper hexacyanoferrate battery electrodes with long cycle life and high power, Nature Communications 2 (2011) 550.

[27] G.L. Soloveichik, Battery technologies for large-scale stationary energy storage, Annual Review of Chemical and Biomolecular Engineering 2 (2011) 503-527.

[28] Y. Shen, K. Kordesch, The mechanism of capacity fade of rechargeable alkaline manganese dioxide zinc cells, Journal of Power Sources 87 (2000) 162-166.

[29] A. Shukla, S. Venugopalan, B. Hariprakash, Nickel-based rechargeable batteries, Journal of Power Sources 100 (2001) 125-148.

[30] U. Köhler, C. Antonius, P. Bäuerlein, Advances in alkaline batteries, Journal of Power Sources 127 (2004) 45-52.

[31] H. Wang, Y. Liang, M. Gong, Y. Li, W. Chang, T. Mefford, J. Zhou, J. Wang, T. Regier, F. Wei, An ultrafast nickel-iron battery from strongly coupled inorganic nanoparticle/nanocarbon hybrid materials, Nature Communications 3 (2012) 917.

[32] X.P. Gao, S.M. Yao, T.Y. Yan, Z. Zhou, Alkaline rechargeable Ni/Co batteries: Cobalt hydroxides as negative electrode materials, Energy & Environmental Science 2 (2009) 502-505.

[33] G. Wang, L. Fu, B. Wang, N. Zhao, Y. Wu, R. Holze, An aqueous rechargeable lithium battery based on LiV_3O_8 and $Li[Ni_{1/3}Co_{1/3}Mn_{1/3}]O_2$, Journal of Applied Electrochemistry 38 (2008) 579-581.

[34] W. Tang, L. Liu, S. Tian, L. Li, L. Li, Y. Yue, Y. Bai, Y. Wu, K. Zhu, R. Holze, $LiMn_2O_4$ nanorods as a super-fast cathode material for aqueous rechargeable lithium batteries, Electrochemistry Communications 13 (2011) 1159-1162.

[35] J.M. Tarascon, M. Armand, Issues and challenges facing rechargeable lithium batteries, Nature 414 (2001) 359-367.

[36] M. Armand, J.M. Tarascon, Building better batteries, Nature 451 (2008) 652-657.

[37] T.H. Kim, J.S. Park, S.K. Chang, S. Choi, J.H. Ryu, H.K. Song, The current move of lithium ion batteries towards the next phase, Advanced Energy Materials 2 (2012) 860-872.

[38] L. Tian, A. Yuan, Electrochemical performance of nanostructured spinel $LiMn_2O_4$ in different aqueous electrolytes, Journal of Power Sources 192 (2009) 693-697.

[39] S. Chen, C. Mi, L. Su, B. Gao, Q. Fu, X. Zhang, Improved performances of mechanical-activated $LiMn_2O_4$/MWNTs cathode for aqueous rechargeable lithium batteries, Journal of Applied Electrochemistry 39 (2009) 1943-1948.

[40] B. Kang, G. Ceder, Battery materials for ultrafast charging and discharging, Nature 458 (2009) 190-193.

[41] X.M. Liu, Z.d.H. , S.w.O. , B.Z. , P.C.M. , M.M.F.Y. , J.K.K. , Carbon nanotube (CNT)-based composites as electrode material for rechargeable Li-ion batteries: A review, Composites Science and Technology 72 (2012) 121-144.

[42] X. Jia, F. Wei, Advances in production and applications of carbon nanotubes, Topics in Current Chemistry 375 (2017) 18.

[43] K. Sun, D.A. Juarez, H. Huang, E. Jung, S.J. Dillon, Aqueous lithium ion batteries on paper substrates, Journal of Power Sources 248 (2014) 582-587.

[44] Y. Sharma, N. Sharma, G. Rao, B. Chowdari, Li-storage and cyclability of urea combustion derived $ZnFe_2O_4$ as anode for Li-ion batteries, Electrochimica Acta 53 (2008) 2380-2385.

[45] Y. Fu, Y. Wan, H. Xia, X. Wang, Nickel ferrite-graphene heteroarchitectures: Toward high-performance anode materials for lithium-ion batteries, Journal of Power Sources 213 (2012) 338-342.

[46] Y. Wang, Z.S. Feng, J.J. Chen, C. Zhang, Synthesis and electrochemical performance of $LiFePO_4$/graphene composites by solid-state reaction, Materials Letters 71 (2012) 54-56.

[47] X. Zhao, C.M. Hayner, H.H. Kung, Self-assembled lithium manganese oxide nanoparticles on carbon nanotube or graphene as high-performance cathode material for lithium-ion batteries, Journal of Materials Chemistry 21 (2011) 17297-17303.

[48] G. Yu, L. Hu, M. Vosgueritchian, H. Wang, X. Xie, J.R. McDonough, X. Cui, Y. Cui, Z. Bao, Solution-processed graphene/MnO_2 nanostructured textiles for high-performance electrochemical capacitors, Nano Letters 11 (2011) 2905-2911.

[49] Z. Fan, J. Yan, T. Wei, L. Zhi, G. Ning, T. Li, F. Wei, Asymmetric supercapacitors based on graphene/MnO_2 and activated carbon nanofiber electrodes with high power and energy density, Advanced Functional Materials 21 (2011) 2366-2375.

[50] Z.S. Wu, W. Ren, D.W. Wang, F. Li, B. Liu, H.M. Cheng, High-energy MnO_2 nanowire/graphene and graphene asymmetric electrochemical capacitors, ACS Nano 4 (2010) 5835-5842.

[51] R. Jiang, C. Cui, H. Ma, Using graphene nanosheets as a conductive additive to enhance the rate performance of spinel $LiMn_2O_4$ cathode material, Physical Chemistry Chemical Physics 15 (2013) 6406-6415.

Chapter 2

[1] G.L. Soloveichik, Battery technologies for large-scale stationary energy storage, Annual Review of Chemical and Biomolecular Engineering 2 (2011) 503-527.

[2] F. Wang, S. Xiao, Y. Hou, C. Hu, L. Liu, Y. Wu, Electrode materials for aqueous asymmetric supercapacitors, RSC Advances 3 (2013) 13059.

[3] N. Alias, A.A. Mohamad, Advances of aqueous rechargeable lithium-ion battery: A review, Journal of Power Sources 274 (2015) 237-251.

[4] Y. Shen, K. Kordesch, The mechanism of capacity fade of rechargeable alkaline manganese dioxide zinc cells, Journal of Power Sources 87 (2000) 162-166.

[5] A. Shukla, S. Venugopalan, B. Hariprakash, Nickel-based rechargeable batteries, Journal of Power Sources 100 (2001) 125-148.

[6] U. Köhler, C. Antonius, P. Bäuerlein, Advances in alkaline batteries, Journal of Power Sources 127 (2004) 45-52.

[7] H. Wang, Y. Liang, M. Gong, Y. Li, W. Chang, T. Mefford, J. Zhou, J. Wang, T. Regier, F. Wei, An ultrafast nickel-iron battery from strongly coupled inorganic nanoparticle/nanocarbon hybrid materials, Nature Communications 3 (2012) 917.

[8] X.P. Gao, S.M. Yao, T.Y. Yan, Z. Zhou, Alkaline rechargeable Ni/Co batteries: Cobalt hydroxides as negative electrode materials, Energy & Environmental Science 2 (2009) 502-505.

[9] W. Li, J. Dahn, D. Wainwright, Rechargeable lithium batteries with aqueous electrolytes, Science 264 (1994) 1115-1118.

[10] G. Wang, L. Fu, N. Zhao, L. Yang, Y. Wu, H. Wu, An aqueous rechargeable lithium battery with good cycling performance, Angewandte Chemie 119 (2007) 299-301.

[11] H. Wang, K. Huang, Y. Zeng, S. Yang, L. Chen, Electrochemical properties of TiP_2O_7 and $LiTi_2(PO_4)_3$ as anode material for lithium ion battery with aqueous solution electrolyte, Electrochimica Acta 52 (2007) 3280-3285.

[12] J.Y. Luo, W.J. Cui, P. He, Y.Y. Xia, Raising the cycling stability of aqueous lithium-ion batteries by eliminating oxygen in the electrolyte, Nature Chemistry 2 (2010) 760-765.

[13] X. Wang, Y. Hou, Y. Zhu, Y. Wu, R. Holze, An aqueous rechargeable lithium battery using coated Li metal as anode, Scientific Reports 3 (2013) 1401.

[14] M. Pasta, C.D. Wessells, R.A. Huggins, Y. Cui, A high-rate and long cycle life aqueous electrolyte battery for grid-scale energy storage, Nature Communications 3 (2012) 1149.

[15] C. Xu, B. Li, H. Du, F. Kang, Energetic zinc ion chemistry: The rechargeable zinc ion battery, Angewandte Chemie 124 (2012) 957-959.

[16] J. Whitacre, A. Tevar, S. Sharma, $Na_4Mn_9O_{18}$ as a positive electrode material for an aqueous electrolyte sodium-ion energy storage device, Electrochemistry Communications 12 (2010) 463-466.

[17] S.I. Park, I. Gocheva, S. Okada, J.i. Yamaki, Electrochemical properties of $NaTi_2(PO_4)_3$ anode for rechargeable aqueous sodium-ion batteries, Journal of The Electrochemical Society 158 (2011) A1067-A1070.

[18] W. Wu, A. Mohamed, J.F. Whitacre, Microwave synthesized $NaTi_2(PO_4)_3$ anode materials for rechargeable aqueous electrolyte sodium-ion battery, in: Meeting Abstracts, The Electrochemical Society 15 (2012) 1859-1859.

[19] Z. Li, D. Young, K. Xiang, W.C. Carter, Y.M. Chiang, Towards high power high energy aqueous sodium-ion batteries: The $NaTi_2(PO_4)_3/Na_{0.44}MnO_2$ system, Advanced Energy Materials 3 (2013) 290-294.

[20] C.D. Wessells, R.A. Huggins, Y. Cui, Copper hexacyanoferrate battery electrodes with long cycle life and high power, Nature Communications 2 (2011) 550.

[21] L. Chen, Q. Gu, X. Zhou, S. Lee, Y. Xia, Z. Liu, New-concept batteries based on aqueous Li^+/Na^+ mixed-ion electrolytes, Scientific Reports 3 (2013) 1946.

[22] C.D. Wessells, S.V. Peddada, M.T. McDowell, R.A. Huggins, Y. Cui, The effect of insertion species on nanostructured open framework hexacyanoferrate battery electrodes, Journal of The Electrochemical Society 159 (2012) A98.

[23] M. Minakshi, P. Singh, S. Thurgate, K. Prince, Electrochemical behavior of olivine-type $LiMnPO_4$ in aqueous solutions, Electrochemical and Solid-State Letters 9 (2006) A471-A474.

[24] J. Yan, J. Wang, H. Liu, Z. Bakenov, D. Gosselink, P. Chen, Rechargeable hybrid aqueous batteries, Journal of Power Sources 216 (2012) 222-226.

[25] T. Ohzuku, M. Kitagawa, T. Hirai, Electrochemistry of manganese dioxide in lithium nonaqueous cell III. X-ray diffractional study on the reduction of spinel-related manganese dioxide, Journal of The Electrochemical Society 137 (1990) 769-775.

[26] A. Czerwiński, M. Żelazowska, M. Grdeń, K. Kuc, J. Milewski, A. Nowacki, G. Wojcik, M. Kopczyk, Electrochemical behavior of lead in sulfuric acid solutions, Journal of Power Sources 85 (2000) 49-55.

[27] K. Popov, B. Grgur, S.S. Djokić, Fundamental aspects of electrometallurgy, Springer Science & Business Media 2007.

[28] K.M. Shaju, P.G. Bruce, A stoichiometric nano-$LiMn_2O_4$ spinel electrode exhibiting high power and stable cycling, Chemistry of Materials 20 (2008) 5557-5562.

[29] F. Jiao, J. Bao, A.H. Hill, P.G. Bruce, Synthesis of ordered mesoporous Li-Mn-O spinel as a positive electrode for rechargeable lithium batteries, Angewandte Chemie International Edition 47 (2008) 9711-9716.

[30] G. Wang, Q. Qu, B. Wang, Y. Shi, S. Tian, Y. Wu, R. Holze, Electrochemical behavior of $LiCoO_2$ in a saturated aqueous Li_2SO_4 solution, Electrochimica Acta 54 (2009) 1199-1203.

[31] G. Wang, L. Yang, Q. Qu, B. Wang, Y. Wu, R. Holze, An aqueous rechargeable lithium battery based on doping and intercalation mechanisms, Journal of Solid State Electrochemistry 14 (2010) 865-869.

[32] M. Winter, J.O. Besenhard, M.E. Spahr, P. Novak, Insertion electrode materials for rechargeable lithium batteries, Advanced Materials 10 (1998) 725-763.

[33] T. Ohzuku, A. Ueda, Solid-state redox reactions of $LiCoO_2$ for secondary lithium cells, Journal of The Electrochemical Society 141 (1994) 2972-2977.

[34] M. Manickam, P. Singh, S. Thurgate, K. Prince, Redox behavior and surface characterization of $LiFePO_4$ in lithium hydroxide electrolyte, Journal of Power Sources 158 (2006) 646-649.

[35] Q. Qu, Y. Shi, S. Tian, Y. Chen, Y. Wu, R. Holze, A new cheap asymmetric aqueous supercapacitor: Activated carbon//$NaMnO_2$, Journal of Power Sources 194 (2009) 1222-1225.

[36] Q. Qu, L. Li, S. Tian, W. Guo, Y. Wu, R. Holze, A cheap asymmetric supercapacitor with high energy at high power: Activated carbon//$K_{0.27}MnO_2 \cdot 0.6H_2O$, Journal of Power Sources 195 (2010) 2789-2794.

[37] Q. Qu, L. Fu, X. Zhan, D. Samuelis, J. Maier, L. Li, S. Tian, Z. Li, Y. Wu, Porous $LiMn_2O_4$ as cathode material with high power and excellent cycling for aqueous rechargeable lithium batteries, Energy & Environmental Science 4 (2011) 3985-3990.

[38] G. Wang, Q. Qu, B. Wang, Y. Shi, S. Tian, Y. Wu, An aqueous electrochemical energy storage system based on doping and intercalation: Ppy//$LiMn_2O_4$, ChemPhysChem 9 (2008) 2299-2301.

[39] J.M. Tarascon, M. Armand, Issues and challenges facing rechargeable lithium batteries, Nature 414 (2001) 359-367.

[40] M. Armand, J.M. Tarascon, Building better batteries, Nature 451 (2008) 652-657.

[41] T.H. Kim, J.S. Park, S.K. Chang, S. Choi, J.H. Ryu, H.K. Song, The current move of lithium ion batteries towards the next phase, Advanced Energy Materials 2 (2012) 860-872.

[42] H. Xia, H. Wang, W. Xiao, L. Lu, M. Lai, Properties of $LiNi_{1/3}Co_{1/3}Mn_{1/3}O_2$ cathode material synthesized by a modified Pechini method for high-power lithium-ion batteries, Journal of Alloys and Compounds 480 (2009) 696-701.

[43] H. Xia, M. Lai, L. Lu, Nanoflaky MnO_2/carbon nanotube nanocomposites as anode materials for lithium-ion batteries, Journal of Materials Chemistry 20 (2010) 6896-6902.

[44] I.B. Stojkovic, N.D. Cvjeticanin, S.V. Mentus, The improvement of the Li-ion insertion behaviour of $Li_{1.05}Cr_{0.10}Mn_{1.85}O_4$ in an aqueous medium upon addition of vinylene carbonate, Electrochemistry Communications 12 (2010) 371-373.

[45] A. Yuan, L. Tian, W. Xu, Y. Wang, Al-doped spinel $LiAl_{0.1}Mn_{1.9}O_4$ with improved high-rate cyclability in aqueous electrolyte, Journal of Power Sources 195 (2010) 5032-5038.

[46] F. Wang, S. Xiao, Y. Shi, L. Liu, Y. Zhu, Y. Wu, J. Wang, R. Holze, Spinel $LiNi_xMn_{2-x}O_4$ as cathode material for aqueous rechargeable lithium batteries, Electrochimica Acta 93 (2013) 301-306.

[47] Y. Tong, M. Shao, Y. Ni, G. Qian, Y. Ye, P. Zhang, Low temperature route to nanocrystalline $LiMn_2O_4$ spinel, Materials Letters 60 (2006) 2578-2581.

[48] S. Vivekanandhan, M. Venkateswarlu, N. Satyanarayana, P. Suresh, D. Nagaraju, N. Munichandraiah, Effect of calcining temperature on the electrochemical performance of nanocrystalline $LiMn_2O_4$ powders prepared by polyethylene glycol (PEG-400) assisted Pechini process, Materials Letters 60 (2006) 3212-3216.

[49] X. Wang, X. Chen, L. Gao, H. Zheng, M. Ji, T. Shen, Z. Zhang, Citric acid-assisted sol-gel synthesis of nanocrystalline $LiMn_2O_4$ spinel as cathode material, Journal of Crystal Growth 256 (2003) 123-127.

[50] C.Z. Lu, G.T.K. Fey, Nanocrystalline and long cycling $LiMn_2O_4$ cathode material derived by a solution combustion method for lithium ion batteries, Journal of Physics and Chemistry of Solids 67 (2006) 756-761.

[51] S.H. Park, S.T. Myung, S.W. Oh, C.S. Yoon, Y.K. Sun, Ultrasonic spray pyrolysis of nano crystalline spinel $LiMn_2O_4$ showing good cycling performance in the 3 V range, Electrochimica Acta 51 (2006) 4089-4095.

[52] K. Sathiyaraj, G.D. Bhuvaneswari, N. Kalaiselvi, A. Peter, H_2O_2-aided one-pot hydrothermal synthesis of nanocrystalline $LiMn_2O_4$ cathode for lithium batteries, IEEE Transactions on Nanotechnology 11 (2012) 314-320.

[53] Y. Chen, K. Xie, Y. Pan, C. Zheng, Nano-sized $LiMn_2O_4$ spinel cathode materials exhibiting high rate discharge capability for lithium-ion batteries, Journal of Power Sources 196 (2011) 6493-6497.

[54] P. Ragupathy, H. Vasan, N. Munichandraiah, Microwave driven hydrothermal synthesis of $LiMn_2O_4$ nanoparticles as cathode material for Li-ion batteries, Materials Chemistry and Physics 124 (2010) 870-875.

[55] L. Fu, H. Liu, C. Li, Y. Wu, E. Rahm, R. Holze, H. Wu, Electrode materials for lithium secondary batteries prepared by sol-gel methods, Progress in Materials Science 50 (2005) 881-928.

[56] M. Zhao, X. Song, F. Wang, W. Dai, X. Lu, Electrochemical performance of single crystalline spinel $LiMn_2O_4$ nanowires in an aqueous $LiNO_3$ solution, Electrochimica Acta 56 (2011) 5673-5678.

[57] W. Tang, Y. Hou, F. Wang, L. Liu, Y. Wu, K. Zhu, $LiMn_2O_4$ nanotube as cathode material of second-level charge capability for aqueous rechargeable batteries, Nano Letters 13 (2013) 2036-40.

[58] W. Tang, L. Liu, S. Tian, L. Li, L. Li, Y. Yue, Y. Bai, Y. Wu, K. Zhu, R. Holze, $LiMn_2O_4$ nanorods as a super-fast cathode material for aqueous rechargeable lithium batteries, Electrochemistry Communications 13 (2011) 1159-1162.

[59] W. Tang, S. Tian, L. Liu, L. Li, H. Zhang, Y. Yue, Y. Bai, Y. Wu, K. Zhu, Nanochain $LiMn_2O_4$ as ultra-fast cathode material for aqueous rechargeable lithium batteries, Electrochemistry Communications 13 (2011) 205-208.

[60] D.K. Kim, P. Muralidharan, H.W. Lee, R. Ruffo, Y. Yang, C.K. Chan, H. Peng, R.A. Huggins, Y. Cui, Spinel $LiMn_2O_4$ nanorods as lithium ion battery cathodes, Nano Letters 8 (2008) 3948-3952.

[61] W. Sun, F. Cao, Y. Liu, X. Zhao, X. Liu, J. Yuan, Nanoporous $LiMn_2O_4$ nanosheets with exposed {111} facets as cathodes for highly reversible lithium-ion batteries, Journal of Materials Chemistry 22 (2012) 20952-20957.

[62] L. Wang, N. Sakai, Y. Ebina, K. Takada, T. Sasaki, Inorganic multilayer films of manganese oxide nanosheets and aluminum polyoxocations: fabrication, structure, and electrochemical behavior, Chemistry of Materials 17 (2005) 1352-1357.

[63] L. Tian, A. Yuan, Electrochemical performance of nanostructured spinel $LiMn_2O_4$ in different aqueous electrolytes, Journal of Power Sources 192 (2009) 693-697.

[64] H. Xia, K.R. Ragavendran, J. Xie, L. Lu, Ultrafine $LiMn_2O_4$/carbon nanotube nanocomposite with excellent rate capability and cycling stability for lithium-ion batteries, Journal of Power Sources 212 (2012) 28-34.

[65] S.T.Z.B. Wen, L.L. Liu, Y.P. Wu, Chapter 13 Controlled particle size and shape of nanomaterials and their applications in supercapacitors, in, Controlled Size and Shape of Nanostructured Materials and their Applications (2012) 473-519.

[66] S. Iijima, Helical microtubules of graphitic carbon, Nature 354 (1991) 56-58.

[67] X. Jia, F. Wei, Advances in production and applications of carbon nanotubes, Topics in Current Chemistry 375 (2017) 18.

[68] X.M. Liu, Z.D. Huang , S.W. Oh , B. Zhang, P.C. Ma, M.M.F. Yuen, J.K. Kim, Carbon nanotube (CNT)-based composites as electrode material for rechargeable Li-ion batteries: A review, Composites Science and Technology 72 (2012) 121-144.

[69] W.K.M. C. Journet, P. Bernier, A. Loiseau, M. Lamy de la Chapelle, S. Lefrant, P. Deniard, R. Lee and J. E. Fischer, Large scale production of single-walled carbon nanotubes by the electric-arc technique, Nature 388 (1997) 756-758.

[70] A.G. Rinzler，J. Liu，H. Dai，P. Nikolaev，C.B. Huffman，F.J. Rodríguez-Macías，P.J. Boul，A.H. Lu，D. Heymann，D.T. Colbert，R.S. Lee，J.E. Fischer，A.M. Rao，P.C. Eklund，R.E. Smalley, Large-scale purification of single-wall carbon nanotubes: process, product, and characterization, Applied Physics A 67 (1998) 29-37.

[71] M.J.B. Pavel Nikolaev, R. Kelley Bradley, Frank Rohmund, Daniel T. Colbert, K.A. Smith, Richard E. Smalley, Gas-phase catalytic growth of single-walled carbon nanotubes from carbon monoxide, Chemical Physics Letters 313 (1999) 91-97.

[72] Z.F. Ren, Synthesis of large arrays of well-aligned carbon nanotubes on glass, Science 282 (1998) 1105-1107.

[73] Q Zhang, J.Q. Huang, W.Z. Qian, Y.Y. Zhang, F. Wei, The road for nanomaterials industry: A review of carbon nanotube production, post-treatment, and bulk applications for composites and energy storage, Small 8 (2013) 1237-1265.

[74] S.A. Morin, M.J. Bierman, J. Tong, S. Jin, Mechanism and kinetics of spontaneous nanotube growth driven by screw dislocations, Science 328 (2010) 476-480.

[75] Q. Wang, M.F. Ng, S.W. Yang, Y. Yang, Y. Chen, The mechanism of single-walled carbon nanotube growth and chirality selection induced by carbon atom and dimer addition, ACS Nano 4 (2010) 939-946.

[76] A.J. Page, Y. Ohta, S. Irle, K. Morokuma, Mechanisms of single-walled carbon nanotube nucleation, growth, and healing determined using QM/MD methods, Accounts of Chemical Research 43 (2010) 1375-1385.

[77] F. Ding, K. Bolton, A. Rosén, Nucleation and growth of single-walled carbon nanotubes: A molecular dynamics study, The Journal of Physical Chemistry B 108 (2004) 17369-17377.

[78] Y. Shibuta, S. Maruyama, Molecular dynamics simulation of formation process of single-walled carbon nanotubes by CCVD method, Chemical Physics Letters 382 (2003) 381-386.

[79] Q. Zhang, M.Q. Zhao, J.Q. Huang, J.Q. Nie, F. Wei, Mass production of aligned carbon nanotube arrays by fluidized bed catalytic chemical vapor deposition, Carbon 48 (2010) 1196-1209.

[80] Y. Yan, J. Miao, Z. Yang, F.X. Xiao, H.B. Yang, B. Liu, Y. Yang, Carbon nanotube catalysts: recent advances in synthesis, characterization and applications, Chemical Society Reviews 44 (2015) 3295-3346.

[81] S. Sinnott, R. Andrews, D. Qian, A.M. Rao, Z. Mao, E. Dickey, F. Derbyshire, Model of carbon nanotube growth through chemical vapor deposition, Chemical Physics Letters 315 (1999) 25-30.

[82] Z. Jin, H. Chu, J. Wang, J. Hong, W. Tan, Y. Li, Ultralow feeding gas flow guiding growth of large-scale horizontally aligned single-walled carbon nanotube arrays, Nano Letters 7 (2007) 2073-2079.

[83] R. Zhang, Y. Zhang, Q. Zhang, H. Xie, W. Qian, F. Wei, Growth of half-meter long carbon nanotubes based on Schulz-Flory distribution, ACS Nano 7 (2013) 6156-6161.

[84] J. Hilding, E.A. Grulke, Z. George Zhang, F. Lockwood, Dispersion of carbon nanotubes in liquids, Journal of Dispersion Science and Technology 24 (2003) 1-41.

[85] Y. Wang, J. Wu, F. Wei, A treatment method to give separated multi-walled carbon nanotubes with high purity, high crystallization and a large aspect ratio, Carbon 41 (2003) 2939-2948.

[86] L. Vaisman, H.D. Wagner, G. Marom, The role of surfactants in dispersion of carbon nanotubes, Advances in Colloid and Interface Science 128 (2006) 37-46.

[87] V. Georgakilas, A. Bourlinos, D. Gournis, T. Tsoufis, C. Trapalis, A.M. Alonso, M. Prato, Multipurpose organically modified carbon nanotubes: from functionalization to nanotube composites, Journal of the American Chemical Society 130 (2008) 8733-8740.

[88] M.O. Guler, A. Akbulut, T. Cetinkaya, H. Akbulut, The effect of MWCNT reinforcing on the electrochemical performance of $LiMn_2O_4$/MWCNT nanocomposite cathodes, International Journal of Energy Research 38 (2014) 509-517.

[89] X. Zhao, C.M. Hayner, H.H. Kung, Self-assembled lithium manganese oxide nanoparticles on carbon nanotube or graphene as high-performance cathode material for lithium-ion batteries, Journal of Materials Chemistry 21 (2011) 17297-17303.

[90] Y. Ding, J. Li, Y. Zhao, L. Guan, Direct growth of $LiMn_2O_4$ on carbon nanotubes as cathode materials for lithium ion batteries, Materials Letters 68 (2012) 197-200.

[91] M. Tang, A. Yuan, H. Zhao, J. Xu, High-performance $LiMn_2O_4$ with enwrapped segmented carbon nanotubes as cathode material for energy storage, Journal of Power Sources 235 (2013) 5-13.

[92] X. Jia, C. Yan, Z. Chen, R. Wang, Q. Zhang, L. Guo, F. Wei, Y. Lu, Direct growth of flexible $LiMn_2O_4$/CNT lithium-ion cathodes, Chemical Communications 47 (2011) 9669.

[93] S.B. Ma, K.W. Nam, W.S. Yoon, S.M. Bak, X.Q. Yang, B.W. Cho, K.B. Kim, Nano-sized lithium manganese oxide dispersed on carbon nanotubes for energy storage applications, Electrochemistry Communications 11 (2009) 1575-1578.

[94] H.P. Hong, M.S. Kim, Y.H. Lee, J.S. Yu, C.J. Lee, N.K. Min, Spray deposition of $LiMn_2O_4$ nanoparticle-decorated multiwalled carbon nanotube films as cathode material for lithium-ion batteries, Thin Solid Films 547 (2013) 68-71.

[95] X. Jia, C. Yan, Z. Chen, R. Wang, Q. Zhang, L. Guo, F. Wei, Y. Lu, Direct growth of flexible $LiMn_2O_4$/CNT lithium-ion cathodes, Chemical Communications 47 (2011) 9669-9671.

[96] S. Chen, C. Mi, L. Su, B. Gao, Q. Fu, X. Zhang, Improved performances of mechanical-activated $LiMn_2O_4$/MWNTs cathode for aqueous rechargeable lithium batteries, Journal of Applied Electrochemistry 39 (2009) 1943-1948.

[97] M. Tang, A. Yuan, H. Zhao, J. Xu, High-performance $LiMn_2O_4$ with enwrapped segmented carbon nanotubes as cathode material for energy storage, Journal of Power Sources 235 (2013) 5-13.

[98] K. Sun, D.A. Juarez, H. Huang, E. Jung, S.J. Dillon, Aqueous lithium ion batteries on paper substrates, Journal of Power Sources 248 (2014) 582-587.

[99] G. Kucinskis, G. Bajars, J. Kleperis, Graphene in lithium ion battery cathode materials: A review, Journal of Power Sources 240 (2013) 66-79.

[100] A.K. Geim, K.S. Novoselov, The rise of graphene, Nature Materials 6 (2007) 183-191.

[101] K.J. Kim, H. Lee, J. Choi, H. Lee, T. Kang, B. Kim, S. Kim, Temperature dependent structural changes of graphene layers on 6H-SiC (0001) surfaces, Journal of Physics: Condensed Matter 20 (2008) 225017.

[102] A.A. Balandin, S. Ghosh, W. Bao, I. Calizo, D. Teweldebrhan, F. Miao, C.N. Lau, Superior thermal conductivity of single-layer graphene, Nano Letters 8 (2008) 902-907.

[103] J.H. Chen, C. Jang, S. Xiao, M. Ishigami, M.S. Fuhrer, Intrinsic and extrinsic performance limits of graphene devices on SiO_2, Nature Nanotechnology 3 (2008) 206-209.

[104] C. Berger, Z. Song, X. Li, X. Wu, N. Brown, C. Naud, D. Mayou, T. Li, J. Hass, A.N. Marchenkov, Electronic confinement and coherence in patterned epitaxial graphene, Science 312 (2006) 1191-1196.

[105] K.S. Novoselov, Z. Jiang, Y. Zhang, S. Morozov, H. Stormer, U. Zeitler, J. Maan, G. Boebinger, P. Kim, A. Geim, Room-temperature quantum Hall effect in graphene, Science 315 (2007) 1379-1379.

[106] K.S. Chen, R. Xu, N.S. Luu, E.B. Secor, K. Hamamoto, Q. Li, S. Kim, V.K. Sangwan, I. Balla, L.M. Guiney, J.W.T. Seo, X. Yu, W. Liu, J. Wu, C. Wolverton, V.P. Dravid, S.A. Barnett, J. Lu, K. Amine, M.C. Hersam, Comprehensive enhancement of nanostructured lithium-Ion battery cathode materials via conformal graphene dispersion, Nano Letters 17 (2017) 2539-2546.

[107] G. Jo, M. Choe, S. Lee, W. Park, Y.H. Kahng, T. Lee, The application of graphene as electrodes in electrical and optical devices, Nanotechnology 23 (2012) 112001.

[108] K. Novoselov, D. Jiang, F. Schedin, T. Booth, V. Khotkevich, S. Morozov, A. Geim, Two-dimensional atomic crystals, Proceedings of the National Academy of Sciences of the United States of America 102 (2005) 10451.

[109] L. Li, J. Xu, G. Li, X. Jia, Y. Li, F. Yang, L. Zhang, C. Xu, J. Gao, Y. Liu, Preparation of graphene nanosheets by shear-assisted supercritical CO_2 exfoliation, Chemical Engineering Journal 284 (2016) 78-84.

[110] J.F Shen, Y.Z. Hu, M. Shi, X. Lu, C. Qin, C. Li, M.X. Ye, Fast and facile preparation of graphene oxide and reduced graphene oxide nanoplatelets, Chemistry of Materials 15 (2009) 3514-3520.

[111] Z. Fan, J. Yan, G. Ning, T. Wei, L. Zhi, F. Wei, Porous graphene networks as high performance anode materials for lithium ion batteries, Carbon 60 (2013) 558-561.

[112] G. Ning, Z. Fan, G. Wang, J. Gao, W. Qian, F. Wei, Gram-scale synthesis of nanomesh graphene with high surface area and its application in supercapacitor electrodes, Chemical Communications 47 (2011) 5976.

[113] I. Iezhokin, P. Offermans, S. Brongersma, A. Giesbers, C. Flipse, High sensitive quasi freestanding epitaxial graphene gas sensor on 6H-SiC, Applied Physics Letters 103 (2013) 053514.

[114] H. Wang, Y. Wang, Z. Hu, X. Wang, Cutting and unzipping multiwalled carbon nanotubes into curved graphene nanosheets and their enhanced supercapacitor performance, ACS Applied Materials & Interfaces 4 (2012) 6827-6834.

[115] P.T. Mohammad Choucair, John A. Stride, Gram-scale production of graphene based on solvothermal synthesis and sonication, Nature Nanotechnology 4 (2009) 30-33.

[116] K.S. Novoselov, A.K. Geim, S.V. Morozov, D. Jiang, Y. Zhang, S.V. Dubonos, I.V. Grigorieva, A.A. Firsov, Electric field effect in atomically thin carbon films, Science 306 (2004) 666-669.

[117] K. Novoselov, A. Geim, S. Morozov, D. Jiang, M.I.K.I.V. Grigorieva, S. Dubonos, A. Firsov, Two-dimensional gas of massless Dirac fermions in graphene, Nature 438 (2005) 197-200.

[118] I. Dékány, R. Krüger-Grasser, A. Weiss, Selective liquid sorption properties of hydrophobized graphite oxide nanostructures, Colloid & Polymer Science 276 (1998) 570-576.

[119] D. Li, M.B. Mueller, S. Gilje, R.B. Kaner, G.G. Wallace, Processable aqueous dispersions of graphene nanosheets, Nature Nanotechnology 3 (2008) 101-105.

[120] J.A.S. Parka, J.R. Pottsa, A. Velamakannia, S. Muralia, R.S. Ruoffa, Hydrazine-reduction of graphite- and graphene oxide, Carbon 49 (2011) 3019-3023.

[121] X. Zhu, G. Ning, Z. Fan, J. Gao, C. Xu, W. Qian, F. Wei, One-step synthesis of a graphene-carbon nanotube hybrid decorated by magnetic nanoparticles, Carbon 50 (2012) 2764-2771.

[122] Y. Sharma, N. Sharma, G. Rao, B. Chowdari, Li-storage and cyclability of urea combustion derived $ZnFe_2O_4$ as anode for Li-ion batteries, Electrochimica Acta 53 (2008) 2380-2385.

[123] Y. Fu, Y. Wan, H. Xia, X. Wang, Nickel ferrite-graphene heteroarchitectures: Toward high-performance anode materials for lithium-ion batteries, Journal of Power Sources 213 (2012) 338-342.

[124] Y. Wang, Z.S. Feng, J.J. Chen, C. Zhang, Synthesis and electrochemical performance of $LiFePO_4$/graphene composites by solid-state reaction, Materials Letters 71 (2012) 54-56.

[125] R. Jiang, C. Cui, H. Ma, Using graphene nanosheets as a conductive additive to enhance the rate performance of spinel $LiMn_2O_4$ cathode material, Physical Chemistry Chemical Physics 15 (2013) 6406-6415.

[126] H. Xu, B. Cheng, Y. Wang, L. Zheng, X. Duan, L. Wang, J. Yang, Y. Qian, Improved electrochemical performance of $LiMn_2O_4$/graphene composite as cathode material for lithium ion battery, International Journal of Eletrochemical Science 7 (2012) 10627-10632.

[127] K.Y. Jo, S.Y. Han, J.M. Lee, I.Y. Kim, S. Nahm, J.W. Choi, S.J. Hwang, Remarkable enhancement of the electrode performance of nanocrystalline $LiMn_2O_4$ via solvothermally-assisted immobilization on reduced graphene oxide nanosheets, Electrochimica Acta 92 (2013) 188-196.

[128] S.M. Bak, K.W. Nam, C.W. Lee, K.H. Kim, H.C. Jung, X.Q. Yang, K.B. Kim, Spinel $LiMn_2O_4$/reduced graphene oxide hybrid for high rate lithium ion batteries, Journal of Materials Chemistry 21 (2011) 17309-17315.

[129] G. Yu, L. Hu, M. Vosgueritchian, H. Wang, X. Xie, J.R. McDonough, X. Cui, Y. Cui, Z. Bao, Solution-processed graphene/MnO_2 nanostructured textiles for high-performance electrochemical capacitors, Nano Letters 11 (2011) 2905-2911.

[130] Z. Fan, J. Yan, T. Wei, L. Zhi, G. Ning, T. Li, F. Wei, Asymmetric supercapacitors based on graphene/MnO_2 and activated carbon nanofiber electrodes with high power and energy density, Advanced Functional Materials 21 (2011) 2366-2375.

[131] Z.S. Wu, W. Ren, D.W. Wang, F. Li, B. Liu, H.M. Cheng, High-energy MnO_2 nanowire/graphene and graphene asymmetric electrochemical capacitors, ACS Nano 4 (2010) 5835-5842.

Chapter 3

[1] J.M. Tarascon, M. Armand, Issues and challenges facing rechargeable lithium batteries, Nature 414 (2001) 359-367.

[2] R. Jiang, C. Cui, H. Ma, Using graphene nanosheets as a conductive additive to enhance the rate performance of spinel $LiMn_2O_4$ cathode material, Physical Chemistry Chemical Physics : PCCP 15 (2013) 6406-6415.

[3] X. Jia, F. Wei, Advances in production and applications of carbon nanotubes, Topics in Current Chemistry 375 (2017) 18.

[4] Q. Zhang, M. Zhao, Y. Liu, A. Cao, W. Qian, Y. Lu, F. Wei, Energy-absorbing hybrid composites based on alternate carbon-nanotube and inorganic layers, Advanced Materials 21 (2009) 2876-2880.

[5] G. Ning, Z. Fan, G. Wang, J. Gao, W. Qian, F. Wei, Gram-scale synthesis of nanomesh graphene with high surface area and its application in supercapacitor electrodes, Chemical Communications 47 (2011) 5976.

[6] X. Jia, C. Yan, Z. Chen, R. Wang, Q. Zhang, L. Guo, F. Wei, Y. Lu, Direct growth of flexible $LiMn_2O_4$/CNT lithium-ion cathodes, Chemical Communications 47 (2011) 9669.

[7] X. Jia, Q. Zhang, M.Q. Zhao, G.H. Xu, J.Q. Huang, W. Qian, Y. Lu, F. Wei, Dramatic enhancements in toughness of polyimide nanocomposite via long-CNT-induced long-range creep, Journal of Materials Chemistry 22 (2012) 7050-7056.

[8] J. Yan, J. Wang, H. Liu, Z. Bakenov, D. Gosselink, P. Chen, Rechargeable hybrid aqueous batteries, Journal of Power Sources 216 (2012) 222-226.

[9] J.X. Yuan, L. Ding , G.S. Cao , T.J. Zhu , H.M. Yu , and X.B. Zhao, Single-crystalline $LiMn_2O_4$ nanotubes synthesized via template-engaged reaction as cathodes for high-power lithium ion batteries, Advanced Functional Materials 21 (2011) 348-355.

[10] D.K. Kim, P. Muralidharan, H.W. Lee, R. Ruffo, Y. Yang, C.K. Chan, H. Peng, R.A. Huggins, Y. Cui, Spinel $LiMn_2O_4$ nanorods as lithium ion battery cathodes, Nano Letters 8 (2008) 3948-3952.

[11] W. Tang, Y. Hou, F. Wang, L. Liu, Y. Wu, K. Zhu, $LiMn_2O_4$/nanotube as cathode material of second-level charge capability for aqueous rechargeable batteries, Nano Letters 13 (2013) 2036-2040.

[12] Q. Qu, L. Fu, X. Zhan, D. Samuelis, J. Maier, L. Li, S. Tian, Z. Li, Y. Wu, Porous $LiMn_2O_4$ as cathode material with high power and excellent cycling for aqueous rechargeable lithium batteries, Energy & Environmental Science 4 (2011) 3985-3990.

[13] Y.G. Wang, Y.Y. Xia, A new concept hybrid electrochemical surpercapacitor: carbon/$LiMn_2O_4$ aqueous system, Electrochemistry Communications 7 (2005) 1138-1142.

[14] F. Ciucci, Revisiting parameter identification in electrochemical impedance spectroscopy: Weighted least squares and optimal experimental design, Electrochimica Acta 87 (2013) 532-545.

Chapter 4

[1] V.L. Pushparaj, M.M. Shaijumon, A. Kumar, S. Murugesan, L. Ci, R. Vajtai, R.J. Linhardt, O. Nalamasu, P.M. Ajayan, Flexible energy storage devices based on nanocomposite paper, Proceedings of the National Academy of Sciences 104 (2007) 13574-13577.

[2] C. Ban, Z. Wu, D.T. Gillaspie, L. Chen, Y. Yan, J.L. Blackburn, A.C. Dillon, Nanostructured Fe_3O_4/SWNT electrode: binder-free and high-rate Li-ion anode, Advanced Materials 22 (2010) E145-E149.

[3] T. Suga, H. Konishi, H. Nishide, Photocrosslinked nitroxide polymer cathode-active materials for application in an organic-based paper battery, Chemical Communications 17 (2007) 1730-1732.

[4] S.Y. Chew, S.H. Ng, J. Wang, P. Novák, F. Krumeich, S.L. Chou, J. Chen, H.K. Liu, Flexible free-standing carbon nanotube films for model lithium-ion batteries, Carbon 47 (2009) 2976-2983.

[5] G. Zhou, D.W. Wang, F. Li, L. Zhang, N. Li, Z.S. Wu, L. Wen, G.Q. Lu, H.M. Cheng, Graphene-wrapped Fe_3O_4 anode material with improved reversible capacity and cyclic stability for lithium ion batteries, Chemistry of Materials 22 (2010) 5306-5313.

[6] H. Gwon, H.S. Kim, K.U. Lee, D.H. Seo, Y.C. Park, Y.S. Lee, B.T. Ahn, K. Kang, Flexible energy storage devices based on graphene paper, Energy & Environmental Science 4 (2011) 1277-1283.

[7] X. Jia, C. Yan, Z. Chen, R. Wang, Q. Zhang, L. Guo, F. Wei, Y. Lu, Direct growth of flexible $LiMn_2O_4$/CNT lithium-ion cathodes, Chemical Communications 47 (2011) 9669-9671.

[8] J. Yan, J. Wang, H. Liu, Z. Bakenov, D. Gosselink, P. Chen, Rechargeable hybrid aqueous batteries, Journal of Power Sources 216 (2012) 222-226.

[9] X. Jia, Q. Zhang, M.Q. Zhao, G.H. Xu, J.Q. Huang, W. Qian, Y. Lu, F. Wei, Dramatic enhancements in toughness of polyimide nanocomposite via long-CNT-induced long-range creep, Journal of Materials Chemistry 22 (2012) 7050-7056.

[10] G. Yuan, J. Bai, T.N.L. Doan, P. Chen, Synthesis and electrochemical investigation of nanosized $LiMn_2O_4$ as cathode material for rechargeable hybrid aqueous batteries, Materials Letters 137 (2014) 311-314.

[11] Z. Han, D. Askhatova, T.N.L. Doan, T.K. Hoang, P. Chen, Experimental and mathematical studies on cycle life of rechargeable hybrid aqueous batteries, Journal of Power Sources 279 (2015) 238-245.

[12] W. Tang, Y. Hou, F. Wang, L. Liu, Y. Wu, K. Zhu, $LiMn_2O_4$ nanotube as cathode material of second-level charge capability for aqueous rechargeable batteries, Nano Letters 13 (2013) 2036-2040.

[13] W. Tang, Y. Zhu, Y. Hou, L. Liu, Y. Wu, K.P. Loh, H. Zhang, K. Zhu, Aqueous rechargeable lithium batteries as an energy storage system of superfast charging, Energy & Environmental Science 6 (2013) 2093-2104.

[14] Y.G. Wang, Y.Y. Xia, Hybrid aqueous energy storage cells using activated carbon and lithium-intercalated compounds I. The C/$LiMn_2O_4$ System, Journal of the Electrochemical Society 153 (2006) A450-A454.

[15] Y.G. Wang, Y.Y. Xia, A new concept hybrid electrochemical surpercapacitor: Carbon/$LiMn_2O_4$ aqueous system, Electrochemistry Communications 7 (2005) 1138-1142.

[16] M. Pasta, C.D. Wessells, R.A. Huggins, Y. Cui, A high-rate and long cycle life aqueous electrolyte battery for grid-scale energy storage, Nature Communications 3 (2012) 1149.

[17] R. Ruffo, C. Wessells, R.A. Huggins, Y. Cui, Electrochemical behavior of $LiCoO_2$ as aqueous lithium-ion battery electrodes, Electrochemistry Communications 11 (2009) 247-249.

[18] J.Y. Luo, Y.Y. Xia, Aqueous lithium-ion battery $LiTi_2(PO_4)_3/LiMn_2O_4$ with high power and energy densities as well as superior cycling stability, Advanced Functional Materials 17 (2007) 3877-3884.

[19] S. Liu, S. Ye, C. Li, G. Pan, X. Gao, Rechargeable aqueous lithium-ion battery of $TiO_2/LiMn_2O_4$ with a high voltage, Journal of The Electrochemical Society 158 (2011) A1490-A1497.

[20] B. Zhang, Y. Liu, X. Wu, Y. Yang, Z. Chang, Z. Wen, Y. Wu, An aqueous rechargeable battery based on zinc anode and $Na_{0.95}MnO_2$, Chemical Communications 50 (2014) 1209-1211.

[21] G. Wang, Q. Qu, B. Wang, Y. Shi, S. Tian, Y. Wu, An aqueous electrochemical energy storage system based on doping and intercalation: Ppy//$LiMn_2O_4$, ChemPhysChem 9 (2008) 2299-2301.

[22] G.J. Wang, H.P. Zhang, L.J. Fu, B. Wang, Y.P. Wu, Aqueous rechargeable lithium battery (ARLB) based on LiV_3O_8 and $LiMn_2O_4$ with good cycling performance, Electrochemistry Communications 9 (2007) 1873-1876.

[23] N. Alias, A.A. Mohamad, Advances of aqueous rechargeable lithium-ion battery: A review, Journal of Power Sources 274 (2015) 237-251.

[24] F.X. Wang, S.Y. Xiao, Y. Shi, L.L. Liu, Y.S. Zhu, Y.P. Wu, J.Z. Wang, R. Holze, Spinel $LiNi_xMn_{2x}O_4$ as cathode material for aqueous rechargeable lithium batteries, Electrochimica Acta 93 (2013) 301-306.

[25] X. Wu, Y. Li, C. Li, Z. He, Y. Xiang, L. Xiong, D. Chen, Y. Yu, K. Sun, Z. He, P. Chen, The electrochemical performance improvement of $LiMn_2O_4$/Zn based on zinc foil as the current collector and thiourea as an electrolyte additive, Journal of Power Sources 300 (2015) 453-459.

[26] W. Tang, L.L. Liu, S. Tian, L. Li, L.L. Li, Y.B. Yue, Y. Bai, Y.P. Wu, K. Zhu, R. Holze, $LiMn_2O_4$ nanorods as a super-fast cathode material for aqueous rechargeable lithium batteries, Electrochemistry Communications 13 (2011) 1159-1162.

[27] W. Tang, S. Tian, L.L. Liu, L. Li, H.P. Zhang, Y.B. Yue, Y. Bai, Y.P. Wu, K. Zhu, Nanochain $LiMn_2O_4$ as ultra-fast cathode material for aqueous rechargeable lithium batteries, Electrochemistry Communications 13 (2011) 205-208.

[28] Q. Qu, L. Fu, X. Zhan, D. Samuelis, J. Maier, L. Li, S. Tian, Z. Li, Y. Wu, Porous $LiMn_2O_4$ as cathode material with high power and excellent cycling for aqueous rechargeable lithium batteries, Energy & Environmental Science 4 (2011) 3985.

[29] X. Jia, Z. Chen, A. Suwarnasarn, L. Rice, X. Wang, H. Sohn, Q. Zhang, B.M. Wu, F. Wei, Y. Lu, High-performance flexible lithium-ion electrodes based on robust network architecture, Energy & Environmental Science 5 (2012) 6845-6849.

Chapter 5

[1] X. Zhu, T.N.L. Doan, Y. Yu, Y. Tian, K.E.K. Sun, H. Zhao, P. Chen, Enhancing rate performance of $LiMn_2O_4$ cathode in rechargeable hybrid aqueous battery by hierarchical carbon nanotube/acetylene black conductive pathways, Ionics 22 (2016) 71-76.

[2] H.P. Min, J.P. Yong, Graphene/$LiMn_2O_4$ nanocomposites for enhanced lithium ion batteries with high rate capability, Journal of Alloys & Compounds 643 (2015) S90-S94.

[3] R. Jiang, C. Cui, H. Ma, Using graphene nanosheets as a conductive additive to enhance the rate performance of spinel $LiMn_2O_4$ cathode material, Physical Chemistry Chemical Physics : PCCP 15 (2013) 6406-6415.

[4] G. Ning, Z. Fan, G. Wang, J. Gao, W. Qian, F. Wei, Gram-scale synthesis of nanomesh graphene with high surface area and its application in supercapacitor electrodes, Chemical Communications 47 (2011) 5976-5978.

[5] X. Zhu, G. Ning, X. Ma, Z. Fan, C. Xu, J. Gao, C. Xu, F. Wei, High density Co_3O_4 nanoparticles confined in porous graphene nanomesh network driven by an electrochemical process: Ultra-high capacity and rate performance for lithium ion batteries, Journal of Materials Chemistry A 1 (2013) 14023-14030.

[6] X. Zhu, X. Song, X. Ma, G. Ning, Enhanced electrode performance of Fe_2O_3 nanoparticle-decorated nanomesh graphene as anodes for lithium-ion batteries, ACS Applied Materials & Interfaces 6 (2014) 7189-7197.

[7] L. Li, J. Xu, G. Li, X. Jia, Y. Li, F. Yang, L. Zhang, C. Xu, J. Gao, Y. Liu, Z. Fang, Preparation of graphene nanosheets by shear-assisted supercritical CO_2 exfoliation, Chemical Engineering Journal 284 (2016) 78-84.

[8] Z. Fan, J. Yan, G. Ning, T. Wei, L. Zhi, F. Wei, Porous graphene networks as high performance anode materials for lithium ion batteries, Carbon 60 (2013) 558-561.

[9] X. Zhu, G. Ning, Z. Fan, J. Gao, C. Xu, W. Qian, F. Wei, One-step synthesis of a graphene-carbon nanotube hybrid decorated by magnetic nanoparticles, Carbon 50 (2012) 2764-2771.

[10] J. Yan, Z. Fan, T. Wei, W. Qian, M. Zhang, F. Wei, Fast and reversible surface redox reaction of graphene-MnO_2 composites as supercapacitor electrodes, Carbon 48 (2010) 3825-3833.

[11] E.P. Barrett, L.G. Joyner, P.P. Halenda, The determination of pore volume and area distributions in porous substances. I. Computations from nitrogen isotherms, Journal of the American Chemical Society 73 (1951) 373-380.

[12] J. Li, X. Zhang, R. Peng, Y. Huang, L. Guo, Y. Qi, $LiMn_2O_4$/graphene composites as cathodes with enhanced electrochemical performance for lithium-ion capacitors, RSC Advances 6 (2016) 54866-54873.

[13] Y. Wang, L. Chen, Y. Wang, Y. Xia, Cycling stability of spinel $LiMn_2O_4$ with different particle sizes in aqueous electrolyte, Electrochimica Acta 173 (2015) 178-183.

[14] Y. Chen, K. Xie, Y. Pan, C. Zheng, Nano-sized $LiMn_2O_4$ spinel cathode materials exhibiting high rate discharge capability for lithium-ion batteries, Journal of Power Sources 196 (2011) 6493-6497.

[15] W. Sun, F. Cao, Y. Liu, X. Zhao, X. Liu, J. Yuan, Nanoporous $LiMn_2O_4$ nanosheets with exposed {111} facets as cathodes for highly reversible lithium-ion batteries, Journal of Materials Chemistry 22 (2012) 20952-20957.

[16] X. Zhu, X. Wu, T.N.L. Doan, Y. Tian, H. Zhao, P. Chen, Binder-free flexible $LiMn_2O_4$/carbon nanotube network as high power cathode for rechargeable hybrid aqueous battery, Journal of Power Sources 326 (2016) 498-504.

[17] W. Tang, Y. Hou, F. Wang, L. Liu, Y. Wu, K. Zhu, $LiMn_2O_4$ nanotube as cathode material of second-level charge capability for aqueous rechargeable batteries, Nano Letters 13 (2013) 2036-2040.

[18] X. Jia, Z. Chen, A. Suwarnasarn, L. Rice, X. Wang, H. Sohn, Q. Zhang, B.M. Wu, F. Wei, Y. Lu, High-performance flexible lithium-ion electrodes based on robust network architecture, Energy & Environmental Science 5 (2012) 6845.

[19] X. Jia, C. Yan, Z. Chen, R. Wang, Q. Zhang, L. Guo, F. Wei, Y. Lu, Direct growth of flexible $LiMn_2O_4$/CNT lithium-ion cathodes, Chemical Communications 47 (2011) 9669.

Chapter 6

[1] G. Kucinskis, G. Bajars, J. Kleperis, Graphene in lithium ion battery cathode materials: A review, Journal of Power Sources 240 (2013) 66-79.

[2] X. Zhu, X. Song, X. Ma, G. Ning, Enhanced electrode performance of Fe_2O_3 nanoparticle-decorated nanomesh graphene as anodes for lithium-ion batteries, ACS Applied Materials & Interfaces 6 (2014) 7189-7197.

[3] J. Yan, J. Wang, H. Liu, Z. Bakenov, D. Gosselink, P. Chen, Rechargeable hybrid aqueous batteries, Journal of Power Sources 216 (2012) 222-226.

[4] J.X. Yuan, L. Ding, G.S. Cao, T.J. Zhu, H.M. Yu, X.B. Zhao, Single-crystalline $LiMn_2O_4$ nanotubes synthesized via template-engaged reaction as cathodes for high-power lithium ion batteries, Advanced Functional Materials 21 (2011) 348-355.

[5] D.K. Kim, P. Muralidharan, H.W. Lee, R. Ruffo, Y. Yang, C.K. Chan, H. Peng, R.A. Huggins, Y. Cui, Spinel $LiMn_2O_4$ nanorods as lithium ion battery cathodes, Nano Letters 8 (2008) 3948-3952.

[6] X. Jia, Z. Chen, A. Suwarnasarn, L. Rice, X. Wang, H. Sohn, Q. Zhang, B. Wu, F. Wei, Y. Lu, High-performance flexible lithium-ion electrodes based on robust network architecture, Energy & Environmental Science 5 (2012) 6845-6849.

[7] T.K.E. Hosono, I. Honma, H. Matsuda, H. Zhou, Synthesis of single crystalline spinel $LiMn_2O_4$ nanowires for a lithium ion battery with high power density, Nano letters 9 (2009) 1045-1051.

[8] F. Ciucci, T. Carraro, W.C. Chueh, W. Lai, Reducing error and measurement time in impedance spectroscopy using model based optimal experimental design, Electrochimica Acta 56 (2011) 5416-5434.

[9] F. Ciucci, W. Lai, Electrochemical impedance spectroscopy of phase transition materials, Electrochimica Acta 81 (2012) 205-216.

[10] F. Ciucci, Revisiting parameter identification in electrochemical impedance spectroscopy: Weighted least squares and optimal experimental design, Electrochimica Acta 87 (2013) 532-545.